ACCELERATOR PHYSICS AND INSTRUMENTATION

ESTIMATION OF RADIOACTIVE BEAM INTENSITIES

J.A. Winger, D.J. Morrissey, and B.M. Sherrill

The prospects for experiments with secondary radioactive beams of exotic nuclei through projectile fragmentation has lead to the development of several facilities worldwide including the recently completed A1200 beam analysis device at the NSCL.[1] Results from the LISE facility at GANIL[2] indicate that numerous experiments involving secondary radioactive beams are possible. However, the feasibility of many experiments depends directly upon the intensity and purity of the secondary beam. These intensities would be impossible to know in advance without direct experimental measurements unless a reasonable method for estimating these rates were developed. Therefore, in the process of bringing the A1200 on-line, we have developed the computer code INTENSITY to provide an order of magnitude estimate of beam rates and purities as well as provide information needed to operate the A1200 as a projectile fragment separator.

INTENSITY incorporates four basic physical processes: 1.) Projectile fragmentation, 2.) Beam energy loss and multiple scattering, 3.) Ion charge state distribution, and 4.) Magnetic separation. Each process has been modeled using a resonable theory or parameterization, but always using a method which will allow for fast calculation. The program INTENSITY is an interactive, menu driven program which allows easy input of information on the production beam and target used, secondary beam desired, and field and apperature settings for the A1200. It is also designed to calculate the optimal settings of the system (production target thickness, field settings, etc.).

The first process involved in the production of a secondary beam is fragmentation of the ion beam from the K1200 cyclotron in a production target at the start of the A1200. In this process, we observe the spectator particles which continue on in the forward direction at nearly the beam velocity after the fragmentation. An estimate of the production rate first requires, of course, an estimate of the production cross section. Two input methods are possible: 1.) Direct input of cross section values using an input file, or 2.) Estimation of the production cross section using the parameterization of Sümmerer, *et al.*[3] The second method, although based on high energy interactions and deep spallation products, is used as a reference given that essentially no cross sections are available. The model of Goldhaber[4] is used, with an additional width added to the transverse spread to account for nuclear reaction effects, to determine the momentum and angular phase space distribution of the projectile fragments. These phase space

distributions are assumed to be gaussian in shape, an assumption that is not necessarily correct since low momentum tails are known to exist. (A better general description of these momentum distributions will be used when available.)

In addition to the pure fragmentation process, it is also necessary to include the effects of the target on the momentum and angular phase spaces. This second class of processes is modeled in the manner described by Schmidt, *et al.*[5] using basic energy loss, energy straggling, and angular straggling formulas. These formulas give reasonable results when compared to experimental data. The effect of the different energy losses of the projectile and fragment in the target is included via a width based on the difference between the final energies of a fragment produced at the front or back of the target. For the angular straggling, a value for the angular width is determined using the average energy of the fragment in the target. These widths are then added in quadrature to the nuclear fragmentation width to obtain the final momentum and angular phase space distributions of the secondary beam. Finally, the percentage of the fragments in various charge states (the third process) is estimated with a parametric formula.[6]

Once the momentum and angular phase space distributions are known, the properties of the A1200 can be used to calculate the fraction of the initial beam that will be transported through to the final image. This final process, magnetic separation, is modeled using first order beam optics. (See Ref. 5 and 7 for details.) Basically, the effects of the beamline magnets of the A1200 are reduced to their magnification and dispersion. In this simulation, only the target(object), dispersive image, and final image points are considered. The mathematical method uses matrix algebra to describe the transfer ($X_{i+1} = RX_i$) of the six dimensional position-angle-momentum phase space (X_i) of the particles through sections of the device. Only the image points, at which many of the matrix elements are zero, are calculated. Consequently, the magnetic separation of the A1200 can be reduce to a simple set of equations describing the phase space location of beam particles at the object, and dispersive and final images. In addition, the use of a wedge degrader[5, 7] is easily implemented since it can be treated as an additional matrix describing the interaction of the beam with the degrader.

In order to determine the transmission of particles described by these equations, it is necessary to apply the physical limitations of the A1200 on the phase space. These 'cuts' determine the angular and momentum acceptance of the A1200.[1] Given the assumed phase space distributions of the beam leaving the target and the matrix equations, it would be easy to perform a Monte Carlo type calculation applying

the cuts to obtain the transmission of the A1200. However, the use of such a method would be quite slow and hence was deemed to be unacceptable. Instead, the cuts are made by integrating the phase space distributions over the limits specified at the corresponding image point. For those cuts which do not occur at one of the image points, their effects are projected to an image point where the integration can be made. (Examples are the angle cuts which do not occur at image points, but can be projected to the object or final image.) In order to do the integrations it is necessary to also transfer the widths of the distributions between the points ($\sigma_{i+1} = R\sigma_i R^T$). This is complicated since cuts at one point can affect the apparent width of the distribution at a subsequent point. In order to determine the manner in which these effects should be taken into account, numerous Monte Carlo calculations were performed. As an example, the apparent dispersion width (σ_δ) for particles in the second half of the device depends only upon the value of the dispersion cut at the dispersive image ($\pm\Delta$) and is reasonably approximated by $\sigma_\delta = 0.627\Delta$. In addition, it is also necessary to include the second order effects of energy and angular straggling in the wedge which are included by adding the first order widths in quadrature with these second order effects. We have found that it is possible to perform integration of gaussian distributions for each cut which deviate from a Monte Carlo calculation by only a few percent at most.

The complexity of the calculation is greatly increased by the inclusion of a degrader wedge. If no wedge is used, then the transmission (acceptance) of the A1200 is determined solely by the acceptance of the first half of the device. This is true because all the particles that are accepted at the dispersive image will be refocussed at the final image in an achromatic system. However, the wedge causes different particle groups to be focussed to different points at the final image as it changes their momentum dispersions from the central rigidity. This can be conceptualized by considering the reverse process of particles going from the final to the dispersive image where only those with the proper dispersion will reach the expected position. (As an example, a particle of interest could have a dispersion of 1% before and after the wedge, while an undesirable contaminant particle starting with a 1% dispersion could have a 2% dispersion after the wedge.) To perform the calculation, the momentum(position)/angular distribution of the particles accepted by the first half of the A1200 is divided into small slices which are passed through the wedge and their acceptance at the final image determined by integrating the final position distribution. In this way, the shape of the wedge can be explicitly considered since the shape of the wedge greatly effects the widths of the final distributions. To determine the proper shape to obtain either an achromatic or monochromatic

final beam, the method described by Geissel, *et al*[7] is used.

INTENSITY has been designed to to be very versatile and adaptable. By changing the parameters (contained in a file) of the device being considered, physically different facilities can be modeled. In addition, the segmented nature of the code allows the inclusion of new methods of calculating the cross sections, fragmentation distributions, energy losses, angular straggling, etc. as new information becomes available. We believe that this is important since the program needs to be adapted to perform calculations of nuclei produced through transfer reactions and not fragmentation. Comparison with experimental results from LISE[2,8] indicate that the program performs quite well. However, certain discrepancies are observed but seem to arise from the limitation of our estimations of the primary cross sections and fragmentation distributions. (For example, the shift down in position and tail on the momentum distribution which brings maximum intensity at slightly lower field settings and adds contamination in separation of proton-rich nuclei.) So far, test comparisons of the program to measurements with the A1200 have been limited. Our experience indicates that the program works exceptionally well for the fragmentation of lighter beams (A<40, within a factor of 2 - 3), but severely overestimates the rates for heavier beams. As a comparison, we present the results in Table 1 for the fragmentation of an 80 MeV/u $^{18}O^{6+}$ beam in a 790 mg/cm^2 Be target. In the future, we hope to make continuing improvements to the program as more experimental information becomes available.

Table 1: Comparison of measured and calculated production rates per particle nanoamp of 80 MeV/u $^{18}O^{6+}$ incident on a 790 mg/cm^2 Be target. The last column provides a ratio of the measured to calculated rates.

Ion	Calculated Rate (pps/pnA)	Measured Rate (pps/pnA)	Ratio
t	2120	28100	13.3
^{6}He	2400	5140	2.14
^{8}He	22.3	17.1	0.77
^{8}Li	6470	4220	0.65
^{9}Li	1140	1620	1.42
^{11}Li	3.4	5.8	1.70
^{11}Be	3860	1430	0.37
^{12}Be	415	635	1.53
^{14}Be	0.7	1.2	1.70
^{13}B	14600	6140	0.42
^{14}B	2300	460	0.20
^{15}B	200	185	0.93
^{16}C	15000	5020	0.33
^{17}C	1400	415	0.30

References

1. B.M. Sherrill, *et al.*, Nucl. Inst. and Meth. A, in press.
2. A.C. Mueller and R. Anne, Nucl. Inst. and Meth. A, in press, and references therein.
3. K. Sümmerer, *et al.*, Phys. Rev. C42 (1990),p 2546.
4. A.S. Goldhaber, Phys. Lett. 53B (1974),p 306.
5. K.-H. Schmidt, *et al.*, Nucl. Inst. and Meth. A260 (1987),p 287.
6. J.A. Winger, unpublished.
7. H. Geissel, *et al.*, Nucl. Inst. and Meth. A282 (1989),p 247.
8. D. Bazin, *et al.*, Nucl. Phys. A515 (1990),p 117.

A SOLID HYDROGEN TARGET

A. Zeller, B. Sherrill, R. Fontus and H. Laumer

As a part of the program to study the nuclear structure of exotic nuclear beams produced in heavy ion fragmentation reactions a thin hydrogen target is being constructed. A pure hydrogen target is superior to hydrogenous plastic targets because all the mass is in the element of interest. At low beam power densities solid hydrogen has the advantage over liquid targets because the thermal conductivity of the solid at 4 K is significantly higher than the liquid at 20 K. Additionally, there is about a 15% gain in density with the solid. By operating at a low differential pressure during filling and warm-up a very thin beryllium window can be used. This keeps background to a minimum since the majority of interactions occur in the hydrogen instead of the window. The target thickness is about 10 mg/cm^2, readily thickened by replacing two copper plates. To allow the greatest flexibility in target location, the target is mounted on an 8 inch Conflat flange. Additionally, the target is cooled by attachment to a small helium dewar, which in turn, is filled from a portable liquid helium dewar. Since the heat shields are cooled with the boiloff helium gas, the system does not require any liquid nitrogen. The only connection to the helium refrigerator is by a warm gas return, which is a simple copper pipe. The system is shown in Fig. 1. along the beam direction. Not shown in the figure are the intermediate heat shields which form cones around the target to reduce the solid angle for 300 K surfaces to shine on the 4 K surfaces. Also not shown are the heaters which will be used to warm up the target and to keep the hydrogen fill lines from freezing out hydrogen and becoming plugged. The expected heat load will allow a minimum of 48 hours of operation from a single 100 liter dewar. To operate, the target will first be filled, then the heater turned on to melt the hydrogen. Re-freezing will insure a uniform density. Background may be checked by vaporizing the hydrogen and pumping out the gas. For safety the volume of hydrogen is kept to a minimum. At room temperature and one atmosphere pressure the volume of gas is only one half of a liter.

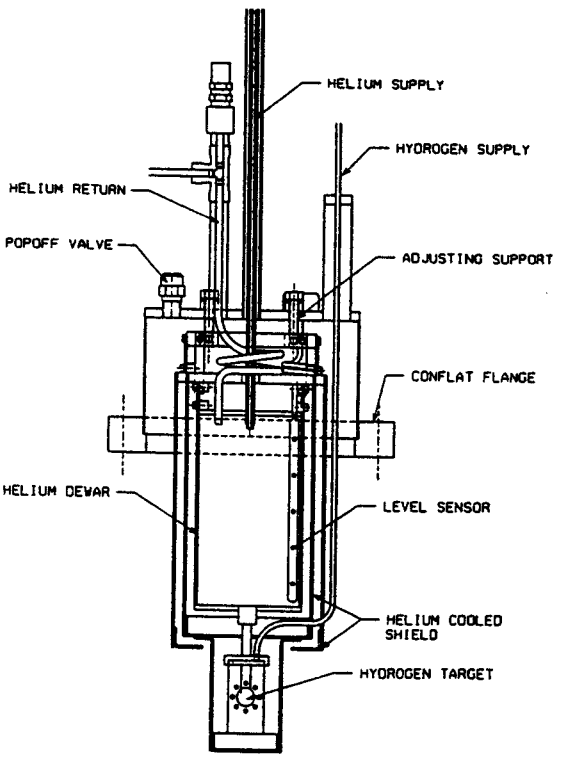

Fig. 1. The solid hydrogen target, looking along the beam direction.

ZERO-DEGREE FOCAL PLANE DETECTOR FOR THE S-320 SPECTROGRAPH

J. Kelley, Sam M. Austin, A. Nadasen,[a] N.A. Orr, D. Swan, J.S. Winfield, and J.E. Yurkon

A detector has been constructed for the S-320 spectrograph focal plane which permits position measurements close to the beam. It was designed specifically for a zero-degree inelastic scattering experiment in which the beam passed through the center of the usual focal plane into a beam dump in the far wall of the vault. The detector spans slightly less than one half the focal plane, and consists of a gas-filled drift chamber with a 8.5 μm diameter Nichrome resistive wire above the window opening. Position is measured by the charge division technique. The entrance and exit windows are 8.5 μm Kapton foils of area 11.7 cm long by 3.5 cm high. The detector is typically filled with 50 to 150 torr of iso-butane gas and the wire held at 1100 to 1500 V.

In order to bring the usable region of detector as close to the beam as possible (thus permitting the measurement of relatively low excitation energies), the detector is designed such that the wire, which is above beam height, overhangs the active window area (see Fig. 1). This feature, together with field shaping in the drift chamber region, minimizes edge effects which would otherwise lead to strong non-linearities. Bench tests of the detector revealed a need for electric field shaping in the drift chamber, to overcome a lack of position sensitivity. Accordingly, five evenly-spaced stripes of chromium were evaporated on 6 μm Mylar foils inside the gas windows, and connected to a bias chain held at 500 to 800 V. The shaping field provided a nearly uniform field of roughly 175 V/cm in the active window area. Figure 2 shows a position spectrum taken with an 8.8-MeV alpha source collimated to 0.3 mm. For this test, the detector was operated with 100 torr of isobutane gas, with a bias of 1125 V on the wire and −690 V on the drift chamber bias chain. The position resolution was found to be 0.9 mm. The position response was found to be linear up to the point where counts were lost at the edges of the window.

In the $^{24}Mg(^{6}Li,^{6}Li^{*})^{24}Mg^{*}$ experiment (described elsewhere in this report), the gas detector was backed by a trio of plastic scintillators which were used to generate ΔE, E, and veto signals. The edge of the detector was 1.0 cm from the nominal beam path. The detector position resolution was measured as 1.8 mm with slits in front of the windows to eliminate beam spot size and target effects. Without the slits, excited states in ^{24}Mg showed a resolution of 420 keV, or 1.6 mm.

a. University of Michigan, Dearborn, MI.

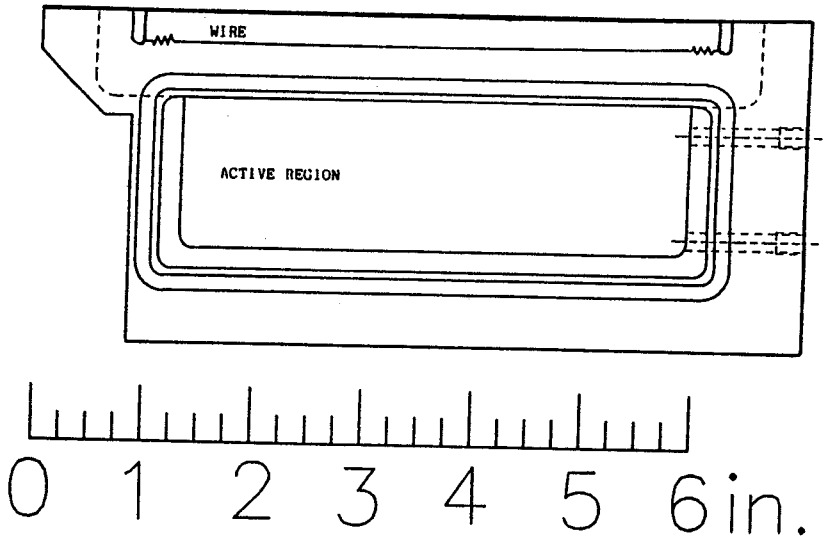

Figure 1: Side view of the focal plane detector

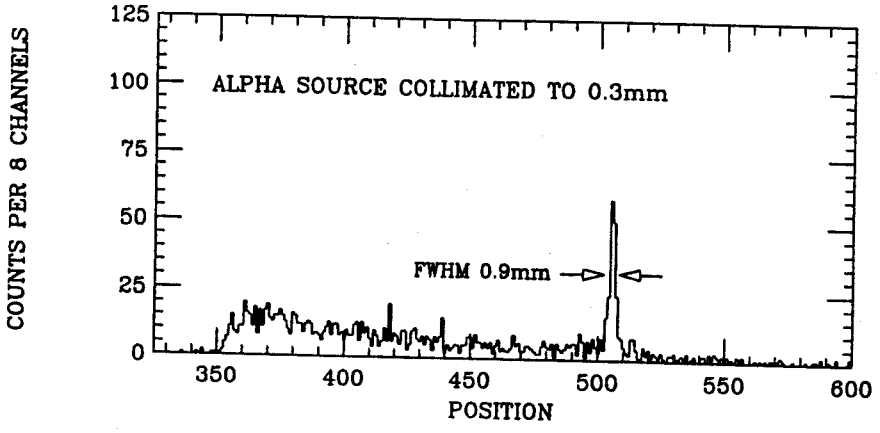

Figure 2: Histogram of counts *vs.* position for an 8.8 MeV collimated alpha source.

RESPONSE OF A BaF_2 DETECTOR TO PHOTONS FROM 75 to 200 MeV

J. Clayton, W. Benenson, J.C. Bergstrom[a], H.S. Caplan[a], E. Hallin[a], N. Levinsky, M. Mohar, R.E. Pywell[a], D.M. Skopik[a], J.D. Stevenson[b], and J.M. Vogt[a]

The goal of this work was to determine tagged photon calibration data for a large volume BaF_2 crystal and show that Monte-Carlo simulations of the electromagnetic shower can reproduce the measured response. In addition, an analytical energy dependent parameterization of the resulting line shape was found for photon energies in the range from 75-200 MeV. A method for establishing a transferable energy calibration using cosmic ray muons for high full-scale energies without the use of monoenergetic photons was also developed.

A large volume BaF_2 crystal was exposed to monochromatic photon beams in the energy range from 75 to 200 MeV at the tagged photon facility of the Saskatchewan Accelerator Laboratory at the University of Saskatchewan. The tagged photons were produced by bremsstrahlung radiation in a thin foil by an incident electron beam. In this measurement the electron beam had a kinetic energy of 264.5 MeV and was incident on an aluminum foil. The energy of the electron after scattering was measured in a magnetic spectrometer which, combined with the knowledge of the incident electron energy, defined the energy of the bremsstrahlung photon. The spectrometer detected electrons above 66 MeV in a focal plane detector consisting of 16 overlapping plastic scintillator paddles.

The BaF_2 detector consists of two right cylinders[1] with a diameter of 12.7 cm and a length of 11.45 cm. The total crystal length is 22.9 cm which is approximately 11.2 radiation lengths deep. The two crystals were coupled together with 10^5 centipoise silicon oil[2] and then wrapped with teflon tape (0.5 mm total thickness), aluminum foil (0.2 mm), and finally black electrical tape. Three 5.08 cm diameter Hamamatsu R2256 quartz window photomultiplier tubes were coupled to one end of the cylinder with an RTV silicon rubber compound which has excellent transmission of UV light. The use of quartz windowed photomultiplier tubes allows complete coverage of the emission spectrum of BaF_2.

The detector was placed in the photon beam 5.48 m from the bremsstrahlung radiator. The size of the photon beam was reduced by a 20 mm diameter collimator placed 1.92 m from the radiator. This gave rise to a spot size of 5.7 cm at the face of the crystal. An 11.4 cm deep 95% tungsten collimator with an acceptance diameter of 7.82 cm was placed in front of the crystal to ensure that the detector was centrally illuminated by the tagged photons. The tungsten collimator was used in studies of high energy

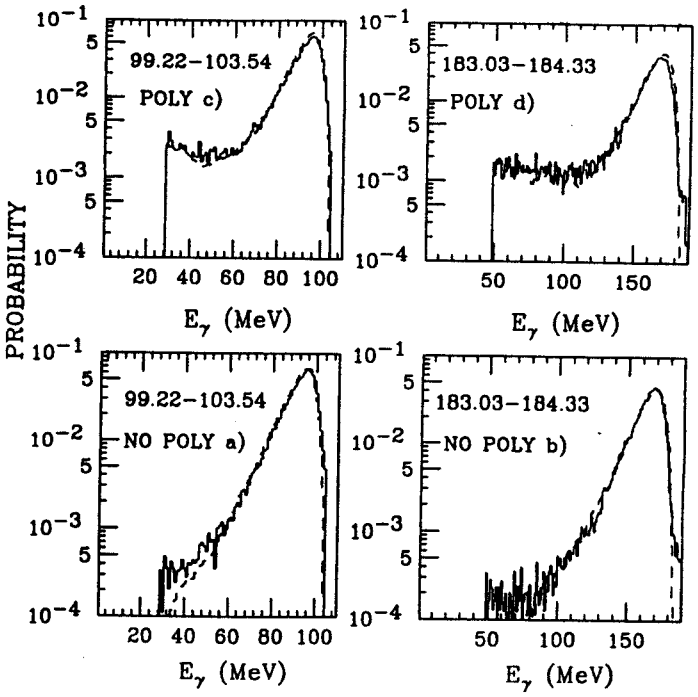

Figure 1: A comparison of the measured (solid) and calculated (dash) spectra for tagged photons in the energy range from 99.22 to 103.54 MeV and from 183.03 and 184.33 MeV respectively. The lower frames (A) and (B) are for the BaF_2 crystal alone while the upper frames (C) and (D) are the BaF_2 crystal plus a 40 cm polyethylene absorber placed in front of the crystal.

bremsstrahlung gamma rays (ie., Ref. 3), and its use in the calibration simulates experimental running conditions. A 2.54 cm thick plastic scintillator anticoincidence shield was used to reject cosmic rays as well as to check on the extent of shower leakage from the crystal. This is approximately one half of the energy deposition for a minimum ionizing particle in the plastic scintillator.

Several runs were also made in which a 40 cm polyethylene absorber bar was placed between the detector and the photon source. This was done to estimate the effect of the polyethylene absorber bar on the attenuation of gamma rays and to investigate its effect on the response function. This was necessary since the absorber bar is used to attenuate fast light particles coming from the target in heavy ion experiments. The Monte-Carlo simulations of the resulting electromagnetic shower were performed with EGS4[4] (Electron Gamma Shower Code). The photons and electrons in the electromagnetic shower were followed down to 100 keV, once reaching this low energy cutoff the particles were considered to be stopped and to have deposited all of their kinetic energy in the active volume. Figure 1 shows a comparison of the EGS4 simulation to the measured tagger data at 99.22 MeV to 103.54 MeV and 181.03 MeV to 184.33 MeV for both configurations. The EGS4 simulations are in good agreement with the measured

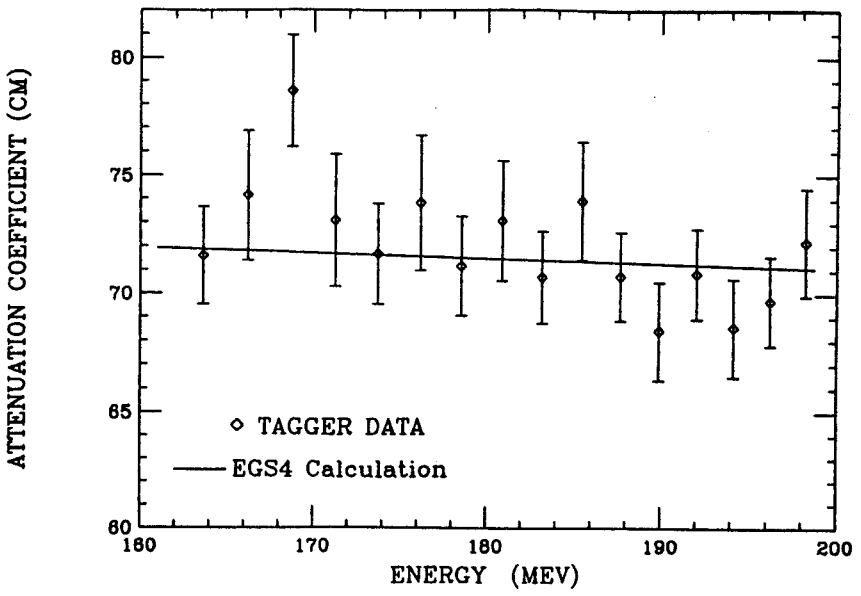

Figure 2: The attenuation coefficients for polyethylene from the measured (squares) and simulated data (solid line) in the energy range from 160 MeV to 200 MeV.

data, and the effect of the absorber is to extend the low energy tail of the distributions. The dashed curves representing the EGS4 simulations are in such good agreement that for the most part they are obscured by the solid curves representing the measured data. The ratio of detector counts in the peak divided by the number focal plane scintillator paddle counts with and without the polyethylene in place gives a measure of the attenuation coefficients for gamma rays in polyethylene at these incident energies. The attenuation coefficients are displayed in Fig. 2. and are in good agreement with the values calculated from the EGS4 simulations.

Calibration of photon detectors is a standard problem, and the usual procedure is to place a source of known γ-ray energy in front of the detector and observe the full-energy peak. This procedure is limited to detectors with sufficient volume to completely absorb the incident photon and is useful only when the region of interest is relatively close to the standard source energies. In measurements that require high full scale energies, large extrapolations from the standard source energies are necessary and this can lead to errors. For high energy photons and detectors with moderate volume a significant fraction of the incident photon energy may leak out of the detector. The resulting peak corresponds to the most probable energy deposited in the active volume, and this shift to lower energies can be significant.

The method of calibration chosen was to compare the most probable energy deposition for the measured tagged photon data and the EGS4 simulations. A least squares fit to the line shape was

made, and then the best-fit parameters were found. Using the best-fit value for the most probable energy deposition, a linear fit to a plot of channel number versus the EGS4 energy was computed. The slope of this line yielded the conversion coefficient from channel number to energy.

With the problems of energy calibration of the detector at high full scale energies in mind, a decision was made to examine the energy deposition in the BaF_2 crystal from cosmic ray muons and compare their energy deposition to that of tagged photons. This was based on the fact that a portable and reproducible energy calibration extremely useful. Calibration with cosmic ray muons avoids the following problems which are all associated with extrapolating the relatively low energy gamma ray sources. For inorganic scintillators with long decay times such as BaF_2 the necessary gates on QDC modules need to be 1.5 – 2.0 μs, and this can lead to large pedestals which hamper peak indentification. A method that employs amplification of the photomultiplier tube output of low energy gamma rays suffers from problems with pedestals in the QDC as well. Since additional amplification of the signal is required, DC offsets can be introduced which effect the measured QDC pedestals. This method also suffers from the fact that for large volume crystals the production and transmission of the scintillation light is not the same at high energies as it is at low energies. The use of cosmic ray muons as a calibration does not suffer from large extrapolations in energy since the energy of the cosmic ray muon is approximately at half the maximum full scale energy used for this detector. Since there is no need to amplify the signal, the electronics set up is not changed and the effect of the pedestal is not significant.

The procedure for the muon calibration was to look at the triple coincidence of the BaF_2 crystal and two 160 cm^2 plastic scintillators placed above and below the crystal. The paddles were placed at the end of the crystal furthest from the photomultiplier tubes to yield a more uniform light transmission to the photomultiplier tubes. A Monte-Carlo simulation of the detector response to cosmic ray muons using GEANT3 (version 3.10/3.11) [5] was carried out. The shape of the measured spectra were well reproduced by the simulation. However, the energy scales are slightly different. The centroid for the GEANT3 simulation is 85 MeV and is slightly higher than the energy calibration based on the EGS4 simulations. The energy scale based on EGS4 calculations yields an equivalent energy deposition of 81 MeV. The discrepancy may be related to the reduced light collection in the experimental measurement. The muon energy deposition will serve as a means to calibrate the full scale energy in applications such as measurements of high energy gamma ray production in heavy-ion collisions at incident energies E/A= 50–150 MeV.

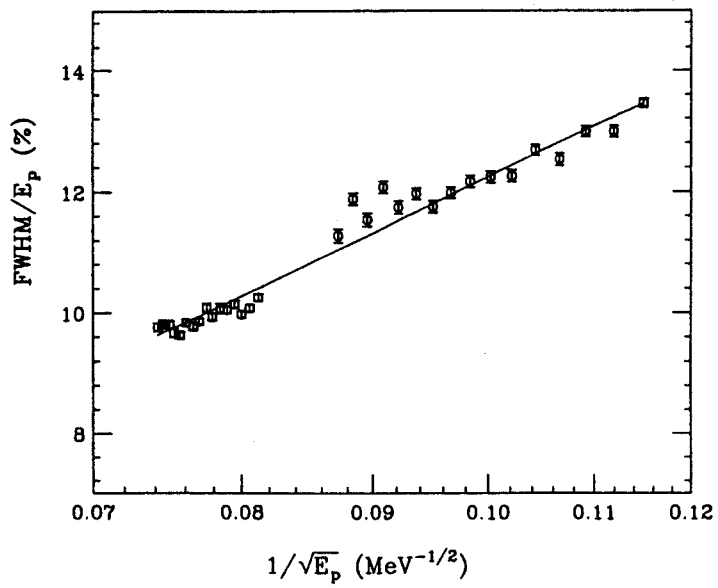

Figure 3: The ratio of the FWHM over the peak energy E_p for the BaF_2 crystal described in this work as a function of $E_p^{-1/2}$. The solid line is a least squared fit to the experimental data.

Of principle importance in describing the performance of any scintillator used in gamma ray measurement is its energy resolution over a large energy range. Since using the ratio σ/E_γ as a measure of the resolution implies a gaussian type response function, and the response of this BaF_2 detector is not gaussian, the definition for the experimental resolution used was given by:

$$R = \frac{FWHM}{E_p} \tag{11}$$

The results are displayed in Fig. 3, which is a plot of the resolution versus $1/\sqrt{E_p}$. Also displayed in Fig. 3 is a least squares fit to the resolution. The function used describes the detector resolution to leading order in powers of $1/\sqrt{E}$ as$(4.4\% \pm 0.3\%)/\sqrt{E_p}$ where E_p is in GeV. A more complete discription of these results can be found in Nuclear Instruments and Methods[6].

a. Saskatchewan Accelerator Laboratory

b. Present address Science Applications International Corp., Santa Clara, CA 95054.

References

1. Supplied by Englehard Corp., Solon, OH
2. Supplied by McGhan-Nusil Corp., CA

3. Supplied by General Electric Corp., NY
4. J. Clayton, J.D. Stevenson,W. Benenson, D. Krofcheck, D.J. Morrissey, T.K. Murakami and J.S. Winfield, Phys. Rev. C42 (1990), p 1009.
5. *The EGS4 Code System*, W.R. Nelson, H. Hirayama and D.W.O. Rogers, Stanford Linear Accelerator Center, Stanford University, Stanford CA, 94305
6. J.S. Clayton et al., N.I.M. (in press)

THE 4π DATA ACQUISITION SYSTEM

A. Vander Molen, R. Au, R. Fox, G.D. Westfall and J. Winfield

The problem of acquiring the large amounts of data from large solid angle detection systems presents a challenge to present day computer systems. The data acquisition system for the MSU 4π Array is no exception. The Array contains 215 phoswich counters, 30 Bragg Curve counters (BCCs), and 30 Parallel Plate Avalanche Counters (PPACs). For each phoswich counter, three quantities must be recorded, ΔE, E, and time, resulting in a requirement to read 645 channels. Five of the BCCs feature segmented anodes which brings the total number of BCC channels to 55. Each channel provides a Z and an E signal. Thus the total number of BCC-related channels is 110. The PPACs provide time and position signals for heavy fragments. The forward five PPACs are segmented into three separate read-outs resulting in 130 position signals and 40 timing signals. Therefore the 4π acquisition system must deal with 925 channels of information.

The 4π acquisition system is based in the ECLine readout bus of the LeCroy Fast Encoding and Readout ADCs (FERAs) charge integrating ADCs and the FERA-compatible Silena peak sensing ADCs. The data from these modules are read out over the ECLine bus in zero-suppressed mode directly into a high speed memory buffered by the FERA Faucet Maier (FFM) module to provide line-time signals and event delimiters. This system eliminates the requirement for bit registers.

The 4π acquisition system has been implemented in its original design configuration with the installation of the FFM module. This configuration takes advantage of the ECLine bus with its high speed (100 ns) data transfer rates. The system has been implemented with both the Lecroy FERAs and the SILENA ADCs. Data rates have been improved by an order of magnitude over the previous system using CAMAC reads. The system has also been configured for the Bragg curves and the PPACs.

The data rates for the system are dependent on the deadtime of the modules used and a rate of 250 nsec/word of valid data. Currently the system is configured to run with a deadtime about 50 μsec/event or a maximum or 20 kiloevents/sec. Currently ethernet restricts rates to 400 kbytes/sec. Several additional gating slots are available for users with no additional software or hardware changes necessary. All online analysis software and control software have been updated to reflect the aforementioned changes.

The system as it currently stands requires no setup by the user short of loading the code, if required, and setting the desired pedestals. All loading and settings are done via user-friendly menu driven programs that require only the knowledge of the FERA and/or Silena modes of operation. A Users Guide is available.

THE 4π GAS HANDLING SYSTEM

A. Vander Molen

The complex gas handling control system for the multiple 4π Bragg curve detectors has been implemented at its first level of control. The system is based on the FERMI control system and interfaces with MKS pressure controllers and a bank of solenoid valves. Each detector has an "in" and an "out" valve. The 30 detectors are arranged in 5 subsystems, each with three valves for venting and pumpdown. Also included is hardware and software for a similar system for the PPACs and the IOWA forward array PPAC. There are 3 remaining MKS controllers and 32 valve controllers for expansion and outside users. The valves are interfaced to the FERMI system via VME binary I/O coupled to OPTO-22 DC modules. The system currently will allow the user to configure the gas control valves of each detector and the control valves of each of the 5 subsystems. These valves can be set individually or collectively. In the latter case the FERMI system has been programmed to set the valve states in one of several configurations by the selection of the appropriate menu choice. This allows the user to configure the system for example for pumpdown or run without having to configure each of the 75 valves associated with the system. A mask is available to take advantage of the menu choices but to prevent selected valves from being used.

The system also allows the user to set each of the 5 subsystems to a given pressure. These systems can be set either individually or collectively. The MKS systems do the actual controlling of the pressure, but they are interfaced to the FERMI system. This allows for remote setting and monitoring. Additionally the system will allow control of the MKS override and monitoring of the deviation state.

The system has been used in several tests and a scheduled experiment with success. However, as it now stands, it does not have the complete user-friendly interface or safety related software. Because of this the system is being used at present only with in-house assistance. Completion of the software is expected over the up coming year.

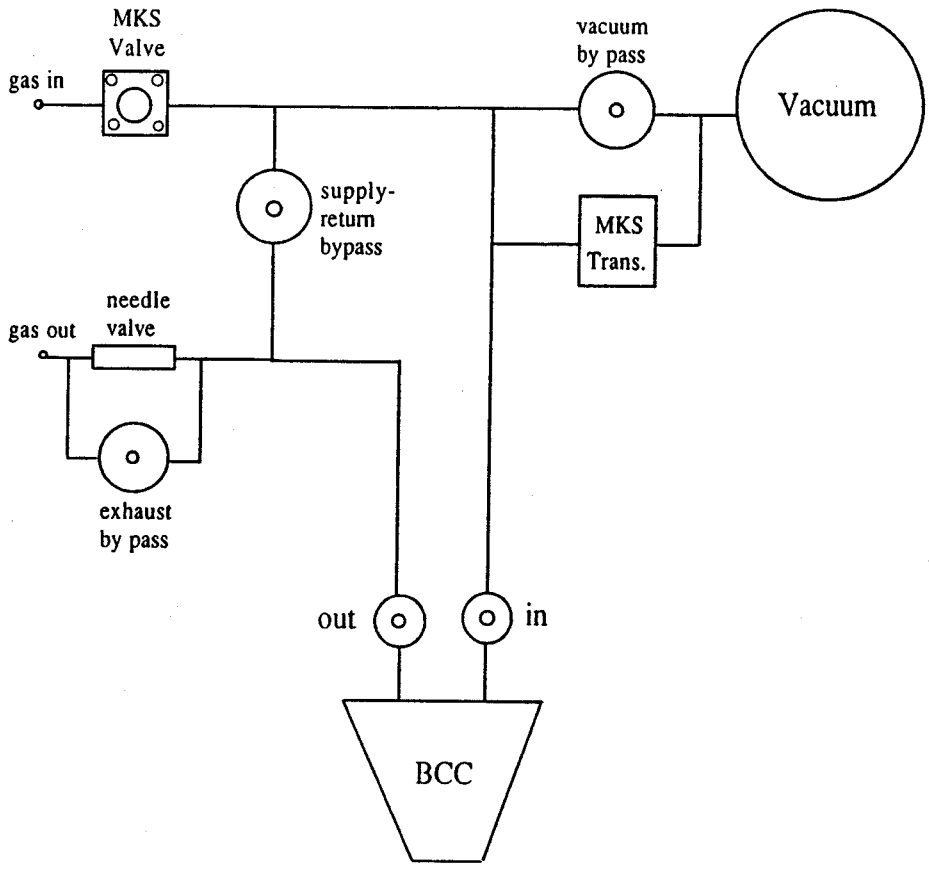
MKS
Valve
gas in
vacuum
by pass
Vacuum
supply-
return
bypass
MKS
Trans.
needle
valve
gas out
exhaust
by pass
out
in
BCC

A FAST DATA TO BUFFER INTERFACE

A. Vander Molen, M.R. Maier, M. Robertson, and G.D. Westfall

The problem of reading out data produced by medium-sized arrays of detectors (number of channels ≤ 1000) has become a problem of immediate concern over the last few years. These systems are not large enough to warrant converting to FASTBUS but still have a large number of parameters. Reading the data through CAMAC is still a viable option, but the relatively slow transfer rates of CAMAC limit the rate at which data can be acquired. We have designed a VME based data acquisition system incorporating commercial and locally designed components that takes full advantage of the LeCroy Fast Encoding and Readout ADC, FERA[1], for the MSU 4π Array.[2] This system demonstrates a performance level similar to a FASTBUS system while maintaining the simplicity and low cost of a CAMAC system.

The data acquisition system of MSU 4π Array detector at NSCL is designed around the LeCroy FERA module. There are 6 major banks of FERAs and Silena peak-sensing ADCs housed in 4 CAMAC crates. The banks are time of flight, two fast plastic signals, two slow plastic signals and Bragg curve signals. Each of these banks has a separate gate and LeCroy 4301 driver. The original design[3] called for the use of the LeCroy ECLine bus, with its high (100 ns/word) data transfer rates. The acquisition systems at NSCL are based on the VME bus[4], and because of this, it was decided to design and build a VME based module to interface the VME with the ECLine bus. Originally there were to be three such modules; one for each of the original CAMAC crates in the system. The data would be buffered in the memory and subsequently transferred to the recording device. In our case this would be magnetic tape.

Subsequent to the design of this module a commercial VME board became available, the Creative Electronics Solution (CES) 8170 memory board, that was similar in concept to what we had proposed. This board is a high speed (100 ns) memory board that interfaces to the ECLine with access to the memory from both the VME and VSB buses. The board, *in situ,* however, had no means to signal the end of transfer of data outside of software intervention. This meant that there was no means to control the deadtime and clear signal at the end of events. Also, there was no event boundary other than that coming from the event structure, which in our case was not predictable. The decision was made to design a board to interface high speed data busses and associated buffer memories with this application in mind. In addition to interfacing the CES module with the ECLine it would also add in a programmable event header word to the data stream and supply a busy signal for deadtime monitoring and a clear for the system at the end of

the event. This combination would, once enabled, run independently of the rest of the acquisition system, supplying all necessary signals. The remaining task of the acquisition system would then be to remove the data from the memory as it became available.

The FFM system (see the figure below) is designed to have a FFM module with up to 10 FERA drivers (Lecroy 4301) on the ECLine data bus and command bus. The drivers are modified so that the last one terminates the command bus. Each of these drivers can then have their own separate gates and a number of FERAs or FERA-like devices. There can be multiple FFM systems on the VME bus. The FFM in turn is gated with a master event signal. Note, however, that the FFM is also designed to have a gate input that can also be used to provide a MASTER gate to all the modules via the command bus. After being gated the FFM would then set its busy line (used for deadtime) and wait a programmable timeout period for a REQ signal (request to be read) from one of the FERAs via the command bus. This is necessary because we run the FERAs in the zero suppression mode and it is possible to have a master gate with no subsequent data. If this is the case the FFM will, after the timeout period, issue a clear on the command bus and drop the busy signal allowing for a new event.

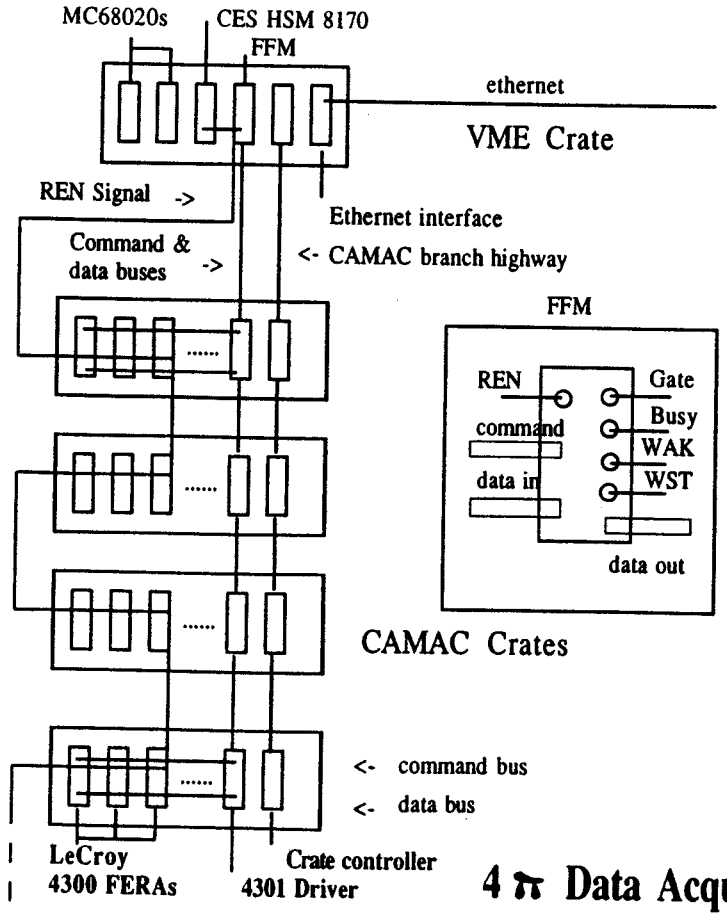

If a REQ is present the FFM will wait another programmable time period to allow for the completion of data conversion of other devices with different conversion times. For example, the FERA-compatible Silenas require about 4 μs for each occupied channel to convert. The FFM will then write a header word from the contents of a VME accessible register to the output ECL data bus and issue a REN (readout enabled) to the FERA's via the command bus. The FFM at this point will become passive and only pass the data and handshaking signals from the high speed data/control lines to the external storage device. It does, however, monitor the REQ signal to determine when the data transfer is completed and then issues a clear and drops its busy line. At this point a new event can be accepted.

With the exception of the initial write to the FFM VME header register, a clear to the VME control register and initializing the memory device, no other interaction is required until the memory device can no longer acquire data. The memory device will not respond to REQs via the handshaking lines and therefore "freezes" the system until it can again acquire the data. At this point the data acquisition system would then remove the data and/or direct the data flow to another memory board. At anytime the FFM state can be monitored via its VME control register which can also be used to issue a clear or busy on the ECL command bus.

The FFM was interfaced to a CES 8170 fast memory module in two different confiqurations for testing. The first arrangement was a simple test of the operational characteristics of the device with one FERA driver and two FERAs. In this confiquration the system transferred data at 180 ns/word and had event times on the order of 20 μs. The latter time is dependent on the aforementioned programmable delay time between a gate and the issuing of the REN signal as well as the FERA conversion/suppression which is on the order of 12 μs.

The second test was in the full 4π set up which contains 6 sets of FERAs, each set with its own driver and one set of Silena ADCs. The total number of FERA or Silena modules was 50. The bus cable length was on the order of 2 meters. The transfer rate in this case was on the order of 250 ns/word. Data reliability tests brought to light a problem with the CES module when it was concurrently being accessed from the VME while acquiring data. The result was to ping-pong two memory modules with no discernable loss in rates. Originally the design was to ping-pong between two memory banks within a single memory module. The new design does raise the cost considerably. Data rates are limited by the rate at which data can be removed from memory to permanent (tape) storage. In our case we are limited to 400 Kbytes/second

by the ethernet link.

An experimental test run of the 4π using both Silenas and FERAs had a deadtime on the order of 40 μs. Most of this is attributed to the aforementioned programmable delays. The delays were set to 32 μs and 24 μs. The former being the maximum time to wait which is the worst case of all 8 channels of a Silena firing only and the latter being the time difference between a FERA firing and a Silena worst case conversion time (32 - 12 μs.). A typical event is around 40 words which takes around 10 μs to read. The data rates to tape during the run were 5000 - 8000 events/second with deadtimes of 70 and 50 percent respectively. These rates were dictated by run time requirements and taping limitations and not the acquisition system.

The FFM module has performed as designed. Our acquisition rates have gone from 3-4 μs/word when reading data from the CAMAC to 250 ns/word. The 4π data acquisition has been implemented with the FFM module interface using 6 banks of FERAs and one bank of Silenas. Our overall data rates have been improved by a factor of 10. Several problems with the CES 8170 in addition to the one described above have resulted in our consideration of a new design for the memory module for future applications. The system has proved to be a viable alternative to FASTBUS for medium sized arrays of detectors.

References

1. ECLine and FERA registered trademarks of LeCroy Corp.
2. G.D. Westfall, J.E. Yurkon, J. van der Plicht, Z.M. Koenig, B.V Jacak, R. Fox, G.M Crawley, M.R. Maier and B.E. Hasselquist, Nucl. Inst. and Meth. A238, (1985), p 347.
3. A. Vander Molen, R. Au, R. Fox, M. Maier, M. Robertson, "Status of the 4π Data Acquisition System", IEEE Trans. on Nucl. Sci., 36, No. 5 (1989), p 1559.
4. R. Fox, R. Au, and A. Vander Molen, "A Multitasking, Multisinking, Multiprocessor Data Acquisition System," IEEE Trans. on Nucl. Sci., 36, No. 5 (1989), p 1562.

CRYOVESSEL FOR THE CURRENT LEADS TEST

J. Kim, S. Hickson, G. Stork and H. Blosser

I. Introduction

A cryogenic test vessel for Liquid Helium, LHe, has been constructed for the comparison of the heat leak through magnet current leads in vertical and horizontal directions and for general cryogenic tests. Since the convection effect of He vapor is very strong due to its small mass, we expect a measurable dependence of the heat leak on configurations of the leads. Numerical estimations are made for an empty tube rather than current leads because the lead structure is complicated and not easily analyzed. We obtain an idea of the convection effect in the real leads by this simulation, even though current leads as heat conductor and heater are neglected.

One of the features in this vessel is to utilize only the outgoing He gas as a coolant of radiation shields (without using LN_2). Assuming that thermal equibilium is established, the system is analyzed to get the temperatures of the shields as well as the LHe boil-off rate. Several platinum thermometers and two LHe level sensors are installed for measurements.

II. Mechanical features

The mechanical features of the vessel are schematically shown in Fig. 1. The sub-sections below detail those features.

1. Vapor shields

The small latent heat of LHe requires very good shielding to reduce the heat load on the liquid He. Two kinds of coolants have been widely used for the radiation shields, i.e. liquid nitrogen and evaporated helium vapor. The use of only one cryogen makes the cryovessel simple, even though the He vapor line on the shielding plates must be long to use fully the enthalphy of the vapor. The tube length needed on contact with the shields has been estimated to be longer than 1 meter under the assumption that the temperature is uniform on the shields (Fig.2)

Because the shield coolant lines are mounted only on the upper plates of the shields, the sides and bottom plates will have a temperature distribution. This is estimated to mean that the bottom plates (considering only the radiation effect) will be 3K higher.

2. Test port for the current leads

The tube which will contain current leads is installed at a 45 degree angle to the main neck tube. This shape allows the current lead to have a horizontal or a vertical orientation just by rotating the vessel 45 degrees clockwise or counterclockwise. The dimensions of the leads are taken

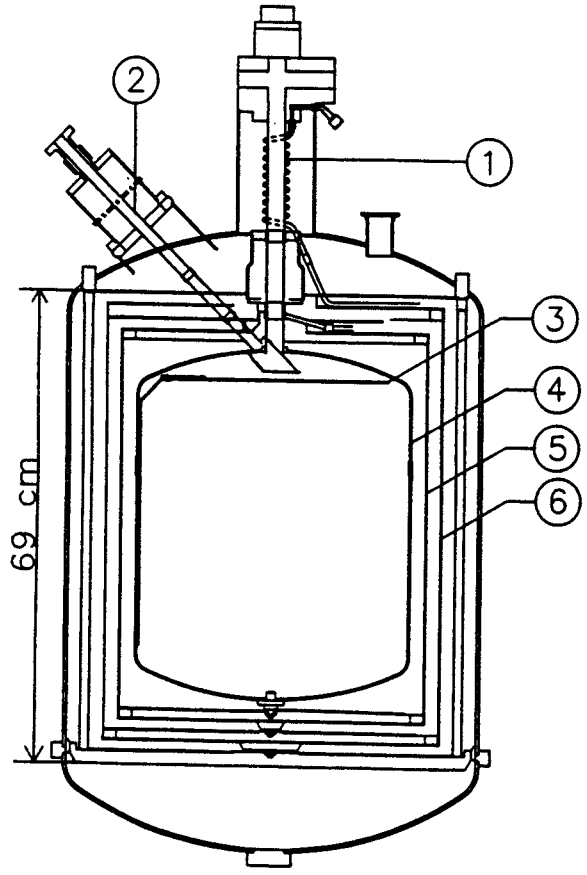

Fig. 1. Schematic view of cryogenic vessel; 1 is main neck tube, 2 is current lead tube, 3 is copper liner, 4 is LHe vessel, 5 is inner heat shield, and 6 is outer heat shield.

to be those of the Harper cyclotron for the purpose of studying the puzzles of heat leaks in the horizontal position.

3. Copper liner

The inner cryovessel has a Cu liner to keep the outgoing gas temperature constant regardless of the LHe level change. Without a copper liner, He gas in the inner vessel (above the liquid) would stratify, and the outgoing gas temperature would vary with liquid level. Considering the large heat capacity of He gas, this effect may not be negligible, and for an accurate heat load estimation the temperature of the outgoing He gas as well as the LHe level change would then need to be measured.

III. Thermal equibilium

A simplified model system involving the conduction and radiation heat transfer is employed to solve the equations of thermal equibilium. The heat leak by conduction mainly flows through the neck tube and the test port tube. The gas tube wrapping around the neck is designed to reduce the conduction heat leak; this effect is, however, ignored in the model calculation because of the relatively small contribution of conduction compared with radiation between room temperature and the outer shield. The radiation heat leak is reduced by laying superinsulation on the outer shield; in addition all radiation surfaces have been applied with 3M aluminum tape. The calculation of the heat load due to conduction is rather straightforward, but the radiation load is not easy to estimate, as it depends on temperature, surface conditions, etc. The equations and dimensions used are described below for each thermally separated region.

1) Region between outside (293K) and outer heat shield (T_1)

The heat leak through the superinsulation between room and liquid nitrogen temperature is shown in Table 1. The differences in values may result from factors such as penetrations and shape of surface and preparation of superinsulation. FNL's value is achieved by a specially prepared vessel while NSCL's result comes from beamline magnets. For our case a weight factor is applied to estimate the heat load between 293K and T_1 using the NSCL result as follows,

$$Q_1 = 2*10^{-4}(W/cm^2) * \text{Area } (cm^2) * (293^4 - T_1^4)/(293^4 - 77^4),$$

where the weight factor is $(293^4 - T_1^4) / (293^4 - 77^4)$.

Table 1. Heat load with 30 layers of superinsulation between 293K and 77K

Fermi National Lab (Ref.1)	NSCL
0.64 W/m^2	2 W/m^2

2) Region between outer(T_1) and inner heat shield(T_2) and between inner heat shield and 4.4K

3M aluminum is taped without multilayer insulation (MLI). The radiation heat load on Al taped surfaces is reported [2] to be about 15mW/m^2 between 77K and 4K. For the temperature ranges under consideration and for solving the thermal equilibrium equations, the black body radiation law with an effective emissivity of 0.03 was thought to be more reasonable. Assuming plane parallel surfaces, the formula[3] used is:

$$Q= (\varepsilon/2)* \sigma * \text{Area} * (T_1^4 - T_1^4),$$

where the factor of 1/2 is due to the taping on both surfaces.

The heat extracted by boiled off helium gas from radiation shields is estimated with a formula used for gas stream cooling by a liquid bath[3]. The heat (Q_{He2}) extracted from the inner shield (T_2), for instance, can be calculated as shown,

$$Q_{He2} = h_2 * S * \int_0^L (T_{He2} - T_2)$$
$$= (4.4K - T_2)(mC_p)[1- \exp(-Lh_2S/mC_p)],$$

where m is mass flow rate, C_p is the specific heat, h_2 is the heat transfer coefficient at T_2, S is the perimeter to which the gas stream transfers heat, and $T_{He2} = (4.4K- T_2) \exp(-Lh_2S/mC_p) + T_2$. T_{He2} is the temperature of He gas in the tube.

In the heat transfer calculation between the gas and solid phases the heat transfer coefficient (h) is unfortunately not well defined. The formulae for h are separated into flow regions frequently designated by Reynold number even though h is largely influenced by the particular fluid and duct that is used. According to the calculated Reynold number (≈300 at 40K) the flow in the tubes on the outer shield belongs to the region of laminar flow (Re < 2300). In this case h is simply represented as a function of the thermal conductivity (k) of He gas and effective diameter (D_e) of duct as follows,

$$h = 3.66\, k/D_e \quad \text{(Ref.4)}$$

For the tubulent flow we could find two different expressions of h from the published results; one of them is $h = 0.0243\, Pr^{0.4} Re^{0.8}\, k/D_e$, which is known as the Dittus-Boelter equation[4], and the other one is more complicated, $h = 0.023\, C_p G^{0.8} \mu^{0.2} / (Pr^{0.6} D_e^{0.2})$ given by McAdams (1954)[3]. The heat transfer coefficient h is computed and compared for two different flows in Table 2. Since the laminar flow has a larger heat transfer with the tube, the estimation in Fig. 2 (using the McAdams formula) gives the

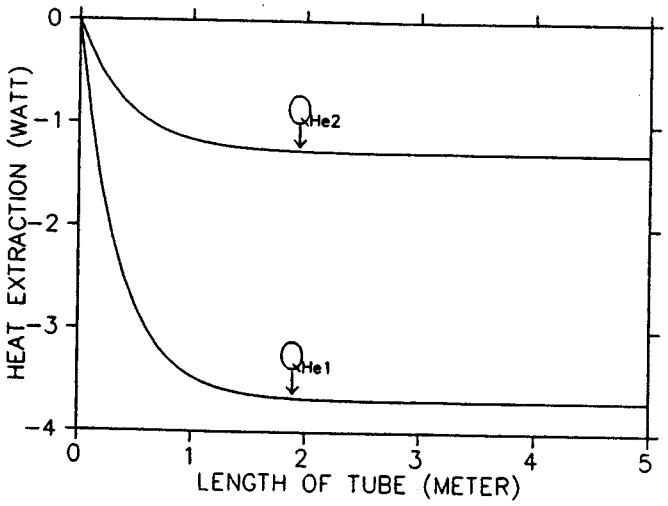

Fig. 2. Extracted heat as a function of tube length assuming 0.19(l/hr) LHe consumption, where Q_{He1} is from outer radiation shield (T_1= 151K), and Q_{He2} is from inner one (T_2=42K). About 1 meter is the required length to fully use the enthalphy of He gas. McAdams' coefficient of heat transfer is used for this calculation (Ref.2)

pessimistic length required. The thermal equibilium equations have been solved always assuming the complete heat exchange, as the actual lengths of the cooling tubes on the shields are much longer than 1 meter. All of the calculated heat loads and the cooling effect of boiled-off helium vapor are summarized in Table 3. Tables 4 and 5 tabulate temperatures on heat shields and helium consumptions, respectively. The thermal equibilium equations are shown below, and these are solved with the aid of computer using T_1 and T_2 as variable parameters.

$$Q_1 + Q_2 - Q_{He1} = Q_3 + Q_4$$

(4.48 Watt + 0.56 Watt - 3.68 Watt = 0.59 Watt + 0.79 Watt)

$$Q_3 + Q_4 - Q_{He2} = Q_5 + Q_6$$

(0.59 Watt + 0.79 Watt - 1.26 Watt = 0.003 Watt + 0.122 Watt),

where $Q_2 = Q_{21} + Q_{22}$, $Q_4 = Q_{41} + Q_{42}$, $Q_6 = Q_{61} + Q_{62}$, and the descriptions of the Q's and values in parenthesis are shown at Table 3.

Table 2. Comparison of heat transfer coefficient

h	Inner shield (42 K)	Outer shield (151 K)
Tubulent (McAdams)	15 W/m^{2}K	13 W/m^{2}K
Laminar	19 W/m^{2}K	58 W/m^{2}K

Table 3. Summary of heat loads

Temperature ranges	Two different values of radiation loads* NSCL FNL
Between 293K and T_1	Q_1 : 4.48 watt, 1.51 watt; through superinsulation
	Q_{21}: 0.48 watt, 0.61 watt; through main tube
	Q_{22}: 0.074 watt, 0.094 watt; through test tube
Between T_1 and T_2	Q_3 : 0.59 watt, 0.18 watt; through Aluminum tape
	Q_{41}: 0.50 watt, 0.29 watt; through main tube
	Q_{42}: 0.29 watt, 0.17 watt; through test tube
Between T_2 and 4.4K	Q_5 : 0.0026 watt, 0.0010 watt; through Aluminum tape
	Q_{61}: 0.087 watt, 0.051 watt; through neck tube
	Q_{62}: 0.035 watt, 0.020 watt; through lead tube
Extracted heat from shields	Q_{He1}: -3.68 watt, -1.57 watt; from outer shield
	Q_{He2}: -1.26 watt, -0.57 watt; from inner shield

* Two different values of radiation load from table 1 are employed for the comparison.

Table 4. Temperatures on shields

Heat shield	NSCL	FNL
Outer shield (T_1) :	151K	112K
Inner shield (T_2) :	42K	33K

Table 5. Total heat load and He consumption

	NSCL	FNL
Total heat load :	0.12 watt	0.08 watt
LHe load @1.2atm :	0.19 l/hr	0.11 l/hr

IV. Convection in the test port tube

Convection effects in a horizontal tube in the absence of real current leads have been studied. This subject attracts more contemporary interest as the horizontal vent tube often becomes mandatory because of the mechanical shape. In contrast to the vertical tube, which has a small convection effect due to the thermal stratification, the horizontal tube has an enormous heat transfer by convection. First, a qualitative description rather than a formula would be more helpful for an understanding of the heat transfer in a horizontal tube. The tube in the horizontal direction becomes dominated by counterflow, which is a good heat conveyor. Depending on the boundary layer theory and experimental observation[5] the flow is laminar except near the room temperature region. We attempt to divide the whole tube into three different regions in Fig. 3. In region 1, the cold He gas from the vessel flows toward the room temperature end. The large specific heat of He vapor may keep the gas cold even after heat exchange with the wall, which has heat influx by conduction and radiation. In region 2, because of tremendous heat transfer by direct contact with the room temperature wall, the gas temperature rise also follows. The boundary layer concept would not be applied any more in this region. In region 3 warm He gas returns to the vessel, carrying a large amount of heat. During counterflow some amount of heat is transfered to the outgoing helium, but the counterflowing helium still bears a lot of heat.

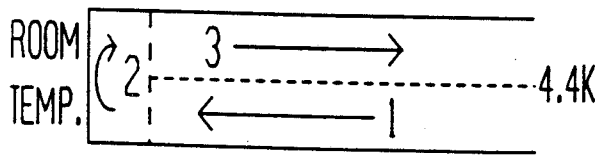

Fig.3 He gas flow in the horizontal tube is divided into three regions for a qualitative understanding.

The above illustration is a simplified heat flow model. In reality we should measure the temperature of the He gas and its flow stream velocity along the tube to completely understand the heat flow. In addition, a global heat transfer formula expressed by Nusselt number (Nu) can be used to estimate the convection effect. The Nusselt number is frequently expressed as a function of a

Rayleigh number (Ra) that is a multiplication of Prantl(Pr) and Grashof(Gr) numbers. For helium gas Pr is almost constant (0.7) in the temperature range under consideration, so the Grashof number acts as main parameter role. A problem in determining Gr, however, is that Gr is a strong function of temperature as well as of tube dimensions. Therefore, it is difficult to determine the average Gr without a complicated numeric calculation because the variation of that value is not linear inside the tube. A simplification is to evaluate Gr at the arithmetically averaged temperature, giving $Ra \approx 6*10^6$ at T=150K. The Nusselt number given by the graph in Ref.4 is within the range 200-600 for the calculated Ra number and our tube dimensions. If we take Nu as 400 for a rough estimate, the total heat load by convection is obtained as follows,

$$Q \text{ (total heat load)} = h*D_e * \text{Area}*(T_w - T_{gas})/L \approx 3 \text{ Watt},$$

where $h = Nu*k/D_e$, $D_e = 1.5$ cm, Area of tube = 1.78 cm^2, Length= 66 cm, and $k = 0.97*10^{-1}$ (W/mK) at 150K.

V. Conclusion

A cryovessel which itself utilizes the evaporated He gas as a coolant is a good object for understanding the cryogenic phenomena. With known properties of helium and the vessel, the thermal equilibrium equations were solved to obtain the boil off rate as well as temperatures on radiation shields. For the horizontal orientation, an estimate of convection effects in the test tube is made since an accurate calculation is not easy. Because of a strong dependence of convection heat transfer on the dimensions of the test tube, the heat transfer will be much larger in the case of an empty test tube (5/8" o.d.) than with the real current leads, which have lots of small empty spaces. Experiments will be carried out after completing fabrication and installation of measuring sensors.

References

1. Q.S. Shu, R.W. Fast and H.L. Hart, Adv. Cryo Eng (1986), Vol.31 p455-463.
2. E.M. Leung et al., Techniques for reducing radiation heat transfer between 77 and 4.2K, Adv. in Cryo Eng, Vol.25, p489, 1985.
3. G.K. White, **Experimental Techniques in Low Temperature Physics**, 3rd, Clarendon press (1979), p58.
4. A. Bejan, Convection Heat Transfer, John Wiley & Sons (1984), p89, 176, 265.
5. H. Ogata, Adv. Cryo Eng(1990), Vol.35, p369.

S800 DIPOLE CONSTRUCTION

A. Zeller, J. Nolen, R. Swanson, J. DeKamp, R. Burleigh, L. Morris, C. Snow and A. McGilvra

Funding from the NSF has been received to complete the construction of one of the S800 Spectrograph's superconducting dipoles. Progress in four major areas is outlined below, with work in other areas proceeding as manpower becomes available.

Support Links

Three-dimensional force calculations were done for us by CEBAF, and the results were used to design support links which are strong enough to constrain the coil but still have small liquid helium heat loads. The design of the links is discussed in another Report. Attachments for the support links to the stainless steel bobbin have been designed and are presently being fabricated, and necessary machining on, the bobbin will soon be done. After all machining has been performed the bobbin will be cold shocked and given a final leak check.

Coil Winding

Insulating spacers required to achieve turn-to-turn transitions and layer-to-layer climbs have been designed and are being procured. The coil will be wound by placing each turn in its own G10 channel, but because of the negative curvature the coil cannot be wound under tension. Therefore, we will keep the wire in place with a series of clamps, which will be loosened in turn as the winding approaches each clamp. After all the turns have been emplaced, the outer cover will be welded on. To keep the wire in place, compressed Be-Cu springs will be used.

Because no single conductor length is long enough to wind a whole coil, splices will be required. If each piece is joined by simply soldering the ends side-by-side, either one turn will be lost, or extra space will be required, resulting in a lumpy coil. Therefore, a technique has been developed which makes the splice occupy the same cross sectional area as a single turn. The conductor is machined in half for the entire one foot length of the splice and then soldered together so there is minimal separation between the superconducting filaments. One of these test splices made by J.Eicher is shown in Fig. 1. We plan on measuring the resistance of one of these splices.

Trim Coils

To extend the width of good field resistive trim coils, located outside the beam vacuum, are to be used[1]. The four coils, connected in series, each consist of two layers of four turns. The

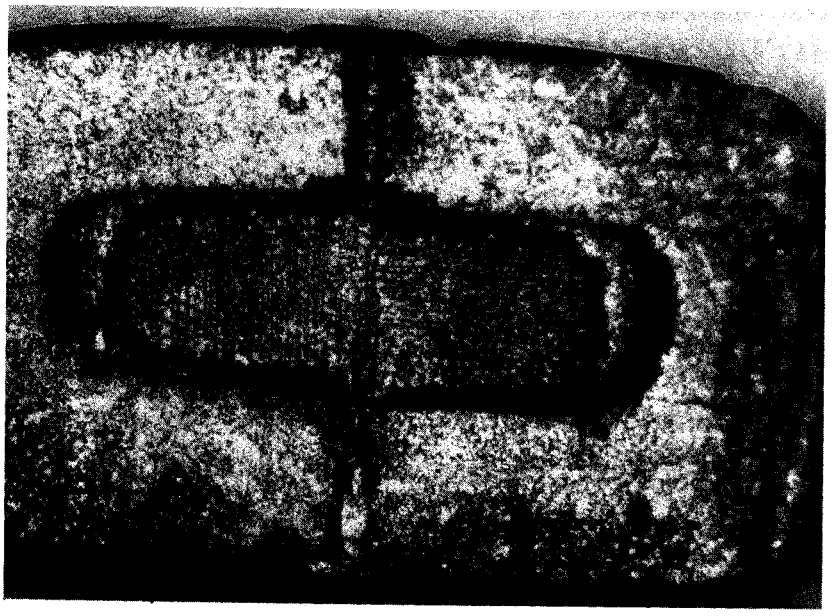

Fig. 1. Cross section of a test splice (magnified 50 times). The superconductor is in the smaller insert halves located in the middle of the conductor. The joint runs from the top of the picture to the bottom.

maximum current in the coils will be about 300 Amps. Winding forms have been designed and methods for attaching the coils to the beam vacuum wall/pole tip spacer and lead routing have been devised.

Mapping Apparatus

In order to do "Ray Reconstruction" at the focal plane a detailed magnetic field map of the dipole is necessary. To accomplish this goal a mapping fixture has been designed. It consists of a cart moving on a plate which is inserted into the dipole gap and extends several feet outside to allow mapping of the fringe fields. Provision has been made to map across the beam direction (radially) and along the beam trajectory, as well to permit measurements above the median plane. The position of the cart will be measured using a small CCD camera to read the position directly, or by sensing "tick" marks along the track. Alternatives, such as direct encoder readouts are also being considered. The field measurements can be made by using a search coil, a Hall Probe, or, in the flat field region in the interior, an NMR probe. The cart has been designed with maximum flexibility.

Coil winding should be completed by the Fall of 1991, with testing to begin a few months later.

We would like to thank S. Nanda of CEBAF for providing the force calculations.

References

1. A.F. Zeller and J.A. Nolen, MSU Ann. Report 1981-82,90.

SUPERCONDUCTING BEAMLINE MAGNET CONSTRUCTION AND OPERATION

J. DeKamp, H. Laumer, C. Magsig, J. Nolen, D. Sanderson, B. Sherrill, A. Zeller

Construction and installation of all superconducting beamline quadrupoles and dipoles as initially needed for Phase II operation were completed in February, 1991. New requirements have added 3 more quadrupole doublet cryostats to make possible the transport of secondary beams to the N4 vault. There are presently 21 doublet cryostats in operation, and there will soon be 24. In addition to the doublets mentioned above, there are 1 quadrupole singlet and 2 quadrupole triplet cryostats, 3 bipolar 16 degree dipoles and 6 bipolar 22.5 degree dipoles. All cryostats are presently cold and operable whenever required and have been transporting beams from the K500 and K1200 cyclotrons to all Phase II experimental areas. The design and construction of these magnets has been reported previously.[1-4]

Analysis Hall Magnet Construction and Installation

Construction and installation of the A1200 beam analysis device[5,6] in the analysis hall was completed in early September, 1990. This line consists of 2 quadrupole triplet and 4 quadrupole doublets as well as four 22.5 degree dipoles. A view of the A1200 line is shown in Figs. 1 and 2.

Fig. 1. Shown is the east end of the A1200 line, which begins at the left of the photo, outside the K1200 vault.

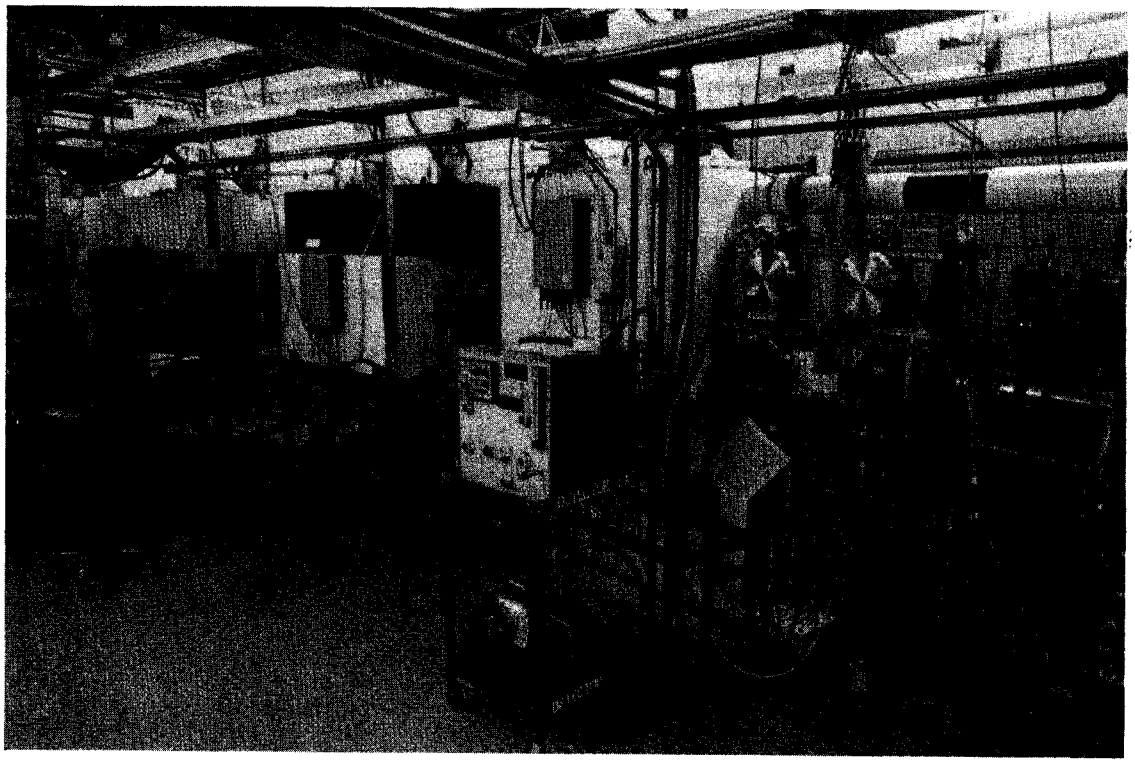

Fig. 2. West end of the A1200. The A1200 ends just inside the transfer hall (not shown) left of the photo.

Actual magnet construction occurring during the year before installation consisted of the completion of the 2 triplets and 3 of the four 22.5 degree dipoles. All of the other magnets had been completed during the previous year. The magnets were installed by working from both ends, working toward the K1200 cyclotron from the transfer hall and working from the K1200 cyclotron toward the transfer hall. The doublets at the center of the A1200 were the last magnets installed.

The complete installation took longer than expected due to the failure of 2 quadrupole coils, each being in a different doublet cryostat, and a subsequent He leak into the insulating vacuum. Both coils failed after having been cooled down and the magnets having been ramped to full field in their initial day of testing and positioning. The doublets were removed and replaced by 2 other doublets from the N4 vault beamline, that were not connected to cryogens or beamline. After installation of these 2 doublets in the A1200 a He leak was noticed in the cryostat vacuum section encompassing the triplet, 2 dipoles, and 3 doublets. Only one of the replacement doublets was installed in this section, and it had been used previously during operation of the Interim vault,[7] suggesting that the leak was in the new cryogenic connections. Efforts to find the source of the leak were not successful and rewelding all the related cryogenic manifold connections did not cure the leak. The leak is small

and is presently being pumped by a small 2" (50 l/s) diffusion pump station with no impact on operation. The additional cost to this line for the permanent pumping station is only $1700, making further efforts to find the leak unjustified. After the initial installation was completed in early September, the A1200 line was cryogenically operational without interruption until November 1. At that time problems with the first dipole after the A1200 line in the transfer hall temporarily made it necessary to exhaust the LN2 boiloff used to cool the magnet cryostat's thermal shields through the last A1200 triplet LN2 container popoff vent instead of the usual cryomanifold exhaust line. During a batch fill, LN2 exhausted from this line and ran down on the top of the triplet cryostat long enough to crack some welds on its vacuum vessel. This destroyed the insulating vacuum for the common section which also included 1 doublet and 2 dipoles. The affected components in a cryostat during a vacuum excursion are the magnet, if energized, and the LHe container, which can overpressurize. The coils were designed and proven to be self protecting during a quench and thus do not need any further protection. At the time of the incident the magnets were not energized. The overpressure protection on the LHe containers functioned as designed. A low oxygen monitor present in the vault also functioned properly, sounding an audible warning. The cracked welds were subsequently repaired and the magnets recooled in a week's time with no impact on cryostat or magnet performance. An exhaust line to an external dewar is now used whenever a temporary LN2 exhaust out of a magnet cryostat is necessary. The A1200 line has been continuously operational since then as of February 28, 1991.

Transfer Hall and N4 Vault Installation

The transfer hall magnet installation was already largely completed by early 1990[8]. Cryomanifold welding was then completed on those magnets. In March, 1990, operation of the K500 cyclotron through the transfer hall to all experimental areas except N4 was possible. This operation continued through September, 1990, during construction of the A1200 line. The only disturbance to the beamline magnets during this time was a stress crack in a weld on one of the magnet cryostat vacuum containers. This caused a vacuum excursion similar to that discussed above in the A1200 line. All magnets in that common section were recooled with no resulting effect on operation, as expected. Remaining installation included the magnets for the beamline to the N4 experimental vault and the dipole for switching beams from the A1200 to the experimental vaults at the beginning of the transfer hall.

The entrance bipolar 16 degree dipole to the transfer hall beamlines was initially installed in the transfer hall in early October, 1990. This magnet was our original prototype and was used previously in interim vault experimental operation. Testing after its first cooldown in its new

location showed ramping problems. A quench during this testing resulted in a short in the current leads. The short was caused by a high voltage between the center tap of the coils and a lead. Our vapor cooled lead design for the beamline magnets has both leads and instrumentation leads together in 1 bundle, insulated only by formvar. This was the only dipole which had a center tap included in its instrumentation leads, although there are a few quadrupole cryostats with coil voltage taps within the lead bundle. The maximum quench voltage on a quad is much lower than that of a dipole, being less than 100 V. The maximum quench voltage for a dipole may reach 700 V. With 33 devices now installed, this is the only lead failure. The prototype dipole was then removed for repair and replaced by a new dipole in early November. Shown in Fig. 3 is this dipole installation which switches beams from the A1200 beamline through the transfer hall beamlines. Experimental operation of the K1200 cyclotron with all Phase II experimental areas except N4 was then in progress.

The installation of magnets for the beamline to the N4 vault took place during Jan.-Feb., 1991. During this time experimental operations also continued after regular daytime working hours, on weekends, and part time during normal work hours. The prototype dipole and the quadrupole doublets requiring repairs were completed and then installed in this line. The previous ramping problems with the dipole were caused by the failure of cold protection diodes originally installed to protect the

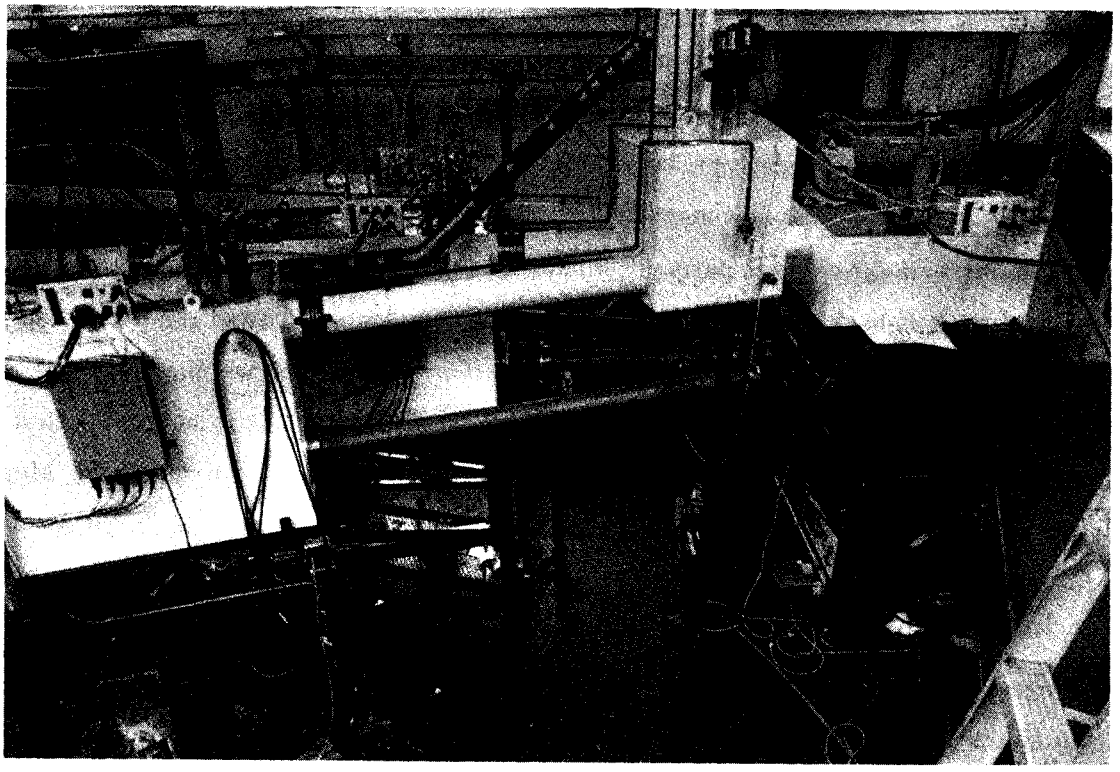

Fig. 3. The beamline from the A1200 enters the ±16° dipole at the right of the photo. This dipole then can bend the beam to any of the 3 beamlines at its exit. Superconducting quadrupole doublets on each beamline are at the left of the photo.

coils in case of a persistent-switch failure. The persistent-switch was removed during previous modifications. The diodes had been left in place because of the difficulty of removing them. The diodes were finally removed and new current leads installed during this repair. The last quadrupole doublet which is installed in the N4 vault does have a He leak to the insulating vacuum which requires pumping. A pumping station is presently installed like the one previously mentioned in the A1200 line. This makes operation possible, but the heat load on the LHe is high enough to warrant repair when the schedule permits. There are no other permanent pumping stations on any magnet cryostat vacuum sections in the entire transfer hall or other experimental vaults, with only self cryopumping maintaining the vacuum. Some of the common cryostat vacuum sections have been cryopumping continuously for over 6 months. Operation to the N4 vault was possible in early March, 1991, thereby completing the initial Phase II magnet installation.

New Construction

Four new quadrupole doublets and a new quadrupole singlet are presently under construction. Three doublets are to be installed to update the N4 beamline, and the fourth is to be used as a spare for replacement of any doublet cryostat which may require repair in the future. The spare doublet will allow us to replace a damaged one immediately and save downtime. The longest downtime that would then be necessary for a doublet replacement would be 2 weeks, the actual time would depend on cooldown of the number of magnets in that common cryostat vacuum section. The new singlet is to replace the prototype outside the K1200 cyclotron, before the A1200 line, which suffered a coil failure. Since the magnet wire and steel for the new magnets were already in-house, the only present purchasing costs for these magnets were for cryostat parts, instrumentation, and controls. Additional purchasing costs were saved on the singlet by reusing the cryostat parts of a "dummy" quad built with the original prototype quad to test reproducibility of cryogenic performance. Coil winding resumed again in November and assembly started in January, 1991. Final assembly of the singlet and the first doublet are presently underway with completion of all 5 cryostats forecast by the middle of May, 1991. Installation of the singlet is schduled in late April, with the new doublets to be installed in the N4 line by the end of June, 1991.

General Magnet Operation Experience

As of the end of February, 1991, a total of 214 superconducting coils are installed in the beamline magnets, 196 in quadrupoles and 18 in dipoles. No dipole coil failures have occurred but 4 quadrupole coil failures have occurred. Each quadrupole coil that failed was in a different magnet

assembly and cryostat. Two of the failures occurred during the initial operation and testing of the devices. The third failure occurred after the device had been through initial testing at a remote location. After it was installed in a beamline in the tranfer hall, it was tested again. The coil failed between then and the time it was called upon for its first actual use as a focussing element. During that period of time the magnet also went through another thermal cycle when it was warmed up for installation of another magnet cryostat in the same cryostat vacuum, and then recooled. The fourth coil failure occurred in the quarupole singlet, our original prototype. This magnet had been in operation since 1985 and had been through about 10 thermal cycles between room temperature and LHe temperature. All the coils that failed, did so because of at least 1 broken turn. It should be noted that 3 of the 4 coils are known to have failed after being in thermal equilibrium, that is they did not break their conductor during the cooldown. It is unknown whether the other coil failed during cooldown. All 4 coils also failed well below their previously achieved currents proving the failure was not due to a training induced quench. Since the conductor in these coils is small (0.3 mm), damage during winding and assembly may also contribute to coil failures. The actual cause of each failure is too difficult to determine. Insurance measures have already been taken to help prevent further failures by controlling the rate of cooldown and lengthening the winding forms to insure the coils do not contract around the pole tip steel creating thermal stress.

Cryogenic efficiency of the beamline magnets has been excellent overall. Total time averaged batch fill requirements for the 32 cryostats is 16 l/hr. About 4 l/hr are transfer losses which result from transfer line cooldown, transfer line heat loads, and losses from the pressure drop in the LHe containers that occurs after filling when returning to steady state operation. Of the 23 quadrupole cryostats now installed, 20 of them operate at least 7 days before needing refilling. Two quadrupole doublet cryostats each have a magnet assembly with a resistance (>10 mohm) which is large enough to generate a noticable amount of heat when the magnets are energized. The new dipoles have been much more cryogenically efficient than the prototype with 6 of the 8 capable of going at least 5.5 days between refills. The other 2 new dipoles were also this efficient when originally installed but were on the same cryostat vacuum section as a doublet cryostat which sufferred a ruptured LHe container,[8] resulting in doubled heat loads on the 2 devices. The steady state heat load of the 2 doublet cryostats with resistances plus the 2 new dipoles involved in the ruptured LHe container incident and the prototype dipole account for 3.5 l/hr LHe. The remaining 27 devices use a total of 8.5 l/hr LHe in steady state operation. These use rates are at their steady state operating pressure of 1.2 atm. The steady state heat load of the doublets average about .27 l/hr LHe, the 2 quad triplets about 0.33 l/hr, and the other 6 dipoles about 0.36 l/hr when corrected to 1 atm.

References

1. A.F. Zeller et al., Proc. of Ninth International Conference on Magnet Technology (1985), p. 160.
2. J.C. DeKamp et al., MSU Annual Report (1987), p. 157.
3. J.C. DeKamp et al., IEEE Trans. Magn. 23, No. 2, 524 (1987).
4. J.C. DeKamp et al., MSU Annual Report (1987), p. 187.
5. B.M. Sherrill et al., MSU Annual Report (1987), p. 190.
6. B.M. Sherrill et al., MSU Annual Report (1989), p. 200.
7. J.C. DeKamp et al., MSU Annual Report (1988), p. 154
8. J.C. DeKamp et al., MSU Annual Report (1989), p. 142.

BEAM DIAGNOSTICS

R. Blue, J. Kuchar, F. Marti, J. A. Nolen, B. Sherrill and J. Yurkon

Introduction

A new kind of internal beam probe has been developed for the K1200 cyclotron. It consists of a small TV camera that looks at the image produced by the beam hitting a phosphor covered plate. The small size of the camera allows it to be placed close to the screen. The image gives a detailed view of the current density in r and z with a resolution of about 0.05 mm. Total beam currents below one electrical pA are easily analyzed. This probe opens new possibilities for the study of internal beam dynamics and allows tuning very weak beams, below one pA.

TV probe

The standard beam probe for the K1200 cyclotron consists of a beam current measuring device that gives limited information on the vertical beam distribution. The probe head is made of three copper leaves separated by small insulating spacers in the vertical direction. The height of each leaf is approximately 6 mm. The probe thickness in the beam path direction is such that it stops completely most of the heavy ions in the energy range of our cyclotron, but not so for lighter ions. The only information that we obtain with this probe is the total current as a function of radius. This is probably enough to study vacuum loses and tune the beam through resonances by maximizing the transmitted beam current, but very little can be learned from a beam dynamics point of view. Several attempts have been made at other laboratories to obtain more information on the internal beam, but these techniques all have limitations [1].

After our successful experience with the use of scintillators and a frame grabber to tune and study external beams [2], we decided to look into the possibility of building a beam probe physically compatible with the present current probe that could include a TV camera to look at a phosphor covered plate. The desire of making both probes interchangeable, so as to use the same hardware for the drive presents severe restrictions on the physical dimensions. The space is limited to a tube of 1.25 inches diameter, that is inserted in the median plane between the two sections of the superconducting coil.

Two major concerns were the possibility of radiation damage to the camera and the high magnetic field (6 T) in which the camera must work. The simplification offered by inserting the camera close to the plate, compared to using an optical system with its associated loses induced us to design and build the TV

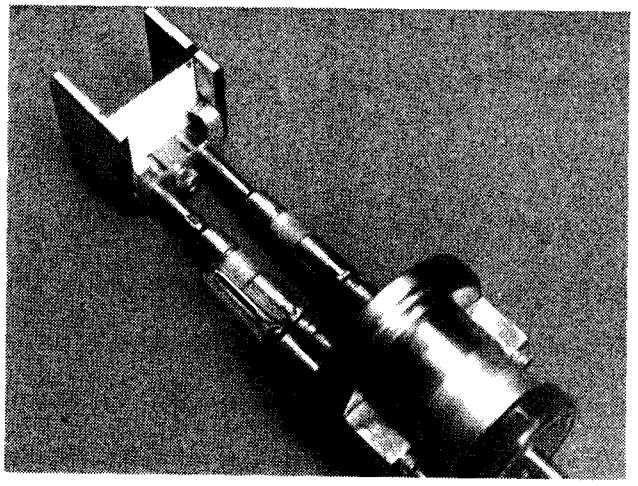

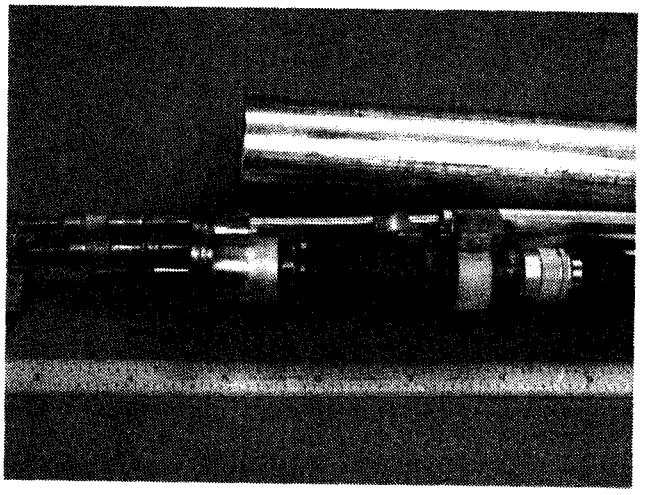

Figure 1: (left) Close up view of the probe head before welding to the vacuum tube. The support for the scintillating plate is seen on the upper left. The plate is held in a groove by springs. The two supports are the electrical connection to the beam current monitors.

Figure 2: (right) TV camera positioned behind the window as it would appear inside the stainless steel tube that is positioned above.

probe. We chose an ELMO 102BW camera after testing it in a magnetic field because of its small size and image quality.

Figure 1 shows a close up view of the probe head, while Figure 2 shows the TV camera placed behind the head next to the stainless tube that encloses the system. The ruler is marked in inches. The phosphor plate is removable, allowing an easy change of the phosphor if needed. The probe removal and reinsertion in the cyclotron can be done under vacuum in a period of 30 minutes. The screens are produced by spraying ZnS phosphor with Krylon as a binding agent.

The two insulators that support the head are hollow and a conducting rod traverses them and carries the current signal to the beam current monitors (BCMs). We have had difficulties reading beam currents below 100 pA, but a beam current below 1 pA gives an easily viewable light output for the TV camera, and produces no radiation damage to the CCD. We have noticed permanent radiation induced damage for currents above 1 nA. This threshold depends on the ion and its energy. But for the cases that we have tested this seems to happen at least 100 times above the currents that we would normally use for TV viewing. The tuning is normally performed with attenuators inserted in the injection beamline. These screens[3] are available with different transmissions, down to 10^{-7}, and sample the beam over the complete phase space, not just collimating it. In the regime of negligeable space charge, the small amount

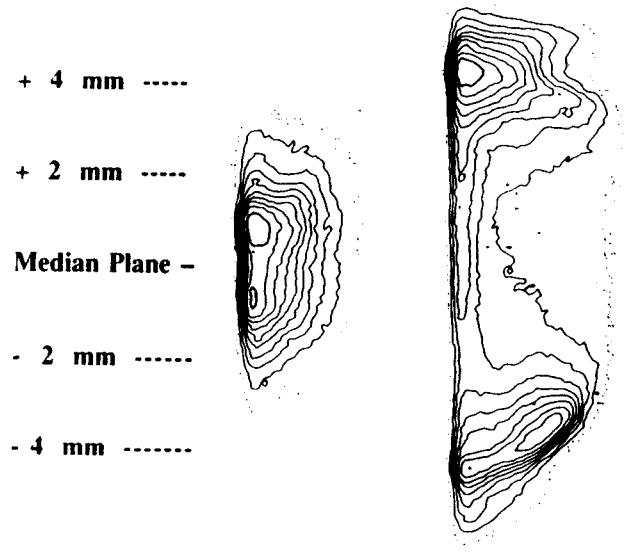

Figure 3: Contour plot of light intensity on the scintillator for a He beam of 40 MeV/u. The probe is at a fixed radius (83 cm), just outside the $\nu_r = 2\nu_z$ coupling resonance. The plot on the left corresponds to a centered beam, while the one on the right is from an off-centered beam.

of current that is injected, is then representative of the total beam; the attenuator thus provides complete control of the beam intensity hitting the probe. Once the beam is tuned, the probe is retracted and the attenuator screens adjusted to match the experiment requirements. Working with low current allows the probe to run with no water cooling, which lowers the electrical noise. The ability to tune beams with very low intensities will allow us to accelerate to higher energies ions that are produced in limited quantities in the ion source. Modern 4π detector experiments require low intensities and could make use of these weak high energy beams.

The glass dome visible at the lower left in figure 1 is used to insert an illuminating optic fiber. The purpose is to inspect the condition of the screen in case there are doubts about its integrity.

The RS170 TV signal from the camera can be sent directly to a B&W monitor, or sent to the frame grabber [2] and the intensity levels displayed in pseudocolor on a color monitor in real time. Figure 3 shows an example of the equicontours of the light intensity for two different centering coil values with the probe at a fixed radius. The beam probe was placed just beyond the region of the $\nu_r = 2\nu_z$ resonance. This coupling resonance transfers energy between the horizontal and vertical oscillation planes. Most of our beams have to cross this resonance, and severe losses can occur if the beam is not centered when crossing it. As the figure shows, the probe picture gives a dramatic visualization of the increase of the vertical

oscillation between the centered beam (left picture) and an off-centered beam (right). These pictures were digitized from a video tape recording. Digitizing from a recorded image introduces some noise that is not present when capturing frames from a live image.

The low noise and detailed information that the probe gives in the r and z planes expands enormously the work that can be done in comparing with orbit tracking simulations. A rich new field opens to us with the new diagnostic tool.

References

1. U. Schryber, "Upgrading the SIN facilities to higher intensities," Proc. of the 10th International Conference on Cyclotrons, East Lansing, 1984, and Minerbo, G., "MENT: A maximum entropy algorithm for reconstructing a source from projection data," Computer Graphics and Image Processing, 10 (1979), p 48.
2. F. Marti et al., "Beam Diagnostics developments at NSCL," Proc. of the 12th International Conference on Cyclotrons, Berlin, 1989.
3. Burton, R.F., D.J. Clark and C.M. Lyneis, "Beam attenuator for the LBL 88 inch cyclotron," Nucl. Instr. Meth. A270 (1988), p 198.

PROGRESS ON THE 8-TESLA MAGNET

J. Kim, J. Bailey, H. Blosser, L. Lee, F. Marti, J. Nolen, G. Stork and A. Zeller

I. Introduction

While the detailed design of the 8-Tesla magnet still is in progress, a few basic aspects of the superconducting magnet have been evaluated and tested. We have chosen a bobbin with a stainless steel cryogenic tank and aluminium coil form, and calculated the stresses on the coil as a function of preloads of winding and banding. A schematic view of a quarter of the magnet is shown in Fig. 1. The quench behavior has been analyzed so that an optimum conductor type can be chosen. Two types of joints for the G-10 support link (bolt and bonding combination joint, and pin joint) were tested to investigate joint strength as well as to find the pin arrangement which minimizes the stress concentration. POISSON[1] gives the off-centering force in the vertical direction so that the needed link strength can be estimated. A three dimensional code such as ANSYS[2] would need to be used to estimate accurately the radial de-centering force; in lieu of this, approximate estimates were made with a dipole model for the yoke and coil.

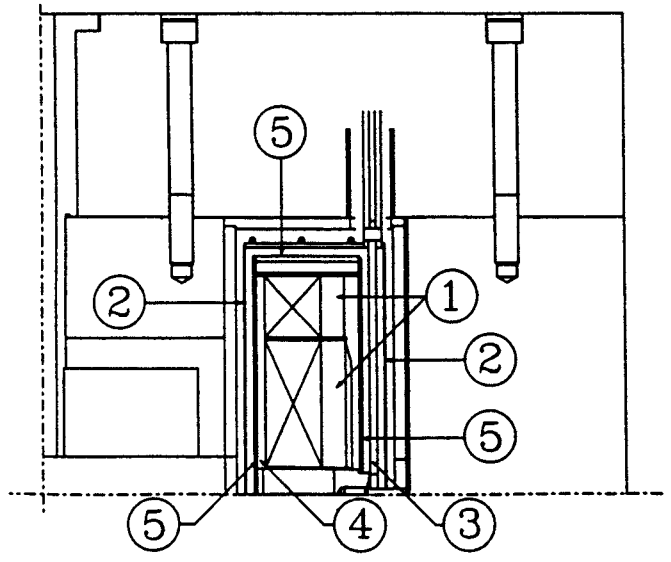

Fig. 1. Schematic view of quarter of magnet. The two section coil is shown with the usual diagonal "X"; numbered elements are 1) stainless steel banding, 2) 77K heat shield, 3) vertical support link (G-10), 4) aluminium bore tube, and 5) stainless steel helium vessel.

Stainless steel aircraft cable was tested as a banding material with the aim of reducing the shear stress on the boundary between the coil and the banding (soft axial banding). The Young's modulus of the coil measured for the transverse direction was about 3×10^5 psi, which is much softer than the coil wound with conductor. However, the structual stretch for the initial load and uncertain mechanical and thermal properties made us choose the rectangular wire.

II. Pre-tensioning of winding and banding

A free coil concept was accepted after being discussed and compared with other options.[3] The amount of preload has been varied in the process of optimization. With a free coil condition

(F_r=0 at the boundary) the limit line of preloads could be found to lift off the coil from the bobbin after cool down (see Fig. 2). The winding preload produces a tighter clamping effect than banding at the boundary for the same load amount. However, we need a proper amount of preload for easy winding. Around 14 lbs load, which produces 4000 psi winding tension, seemed adequate for our conductor and pre-tensioner.

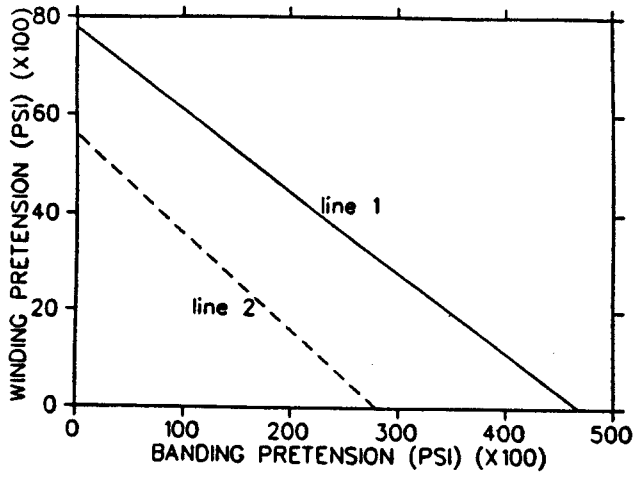

Fig. 2. Limit line of pre-tensions. Line 1 is when the gap size between the Al bobbin and S.S. cryotank (in the unstressed condition) is larger than 0.01" so that two materials do not interfere each other. Line 2 is the case when two materials are completely in contact, so the thermal contraction of the Al coil form is hindered by the stainless steel cryogenic tank.

The hoop stresses on the conductor, computed with STANSOL[4], are shown in Fig. 3 for several choices of pre-tensions. The hoop stress on the conductor must stay below the yield strength of Cu (≈15000psi) to satisfy the criterion of a safe winding. A flat distribution of stress is achieved with a relatively low winding preload (4000 psi) because with a higher one (8000psi) the accumulated winding tension on the innermost layer over-compensates the stress by the magnetic field, while the effect of a raised preload remains on the outer layers. So the overall effect with a high winding preload is a counterclockwise tilt of stress distribution (Fig. 3).

Care has been taken in deciding the coil winding method and preloads in order to avoid the quenches. Two major causes of quenches are prevented with controlled stresses inside the coil: 1) reduced hoop stress below the yield strength of the conductor 2) minimized shear stress. We have used stress analysis programs to examine the stress distributions in the coil with various pre-tensions, and summarize our observations in the following two subsections for the two coil winding methods (tightly banded coil and free coil).

1) Tightly banded coil

Tightly banded means that the coil is firmly clamped on the bobbin by the preloads of winding and banding, which should produce a radial force strong enough to overcome the expanding pressure from the magnetic force. Because the axial force of the coil at the interface is countered by frictional force, the plane shear stress is at a maximum, especially in corners where the axial force is

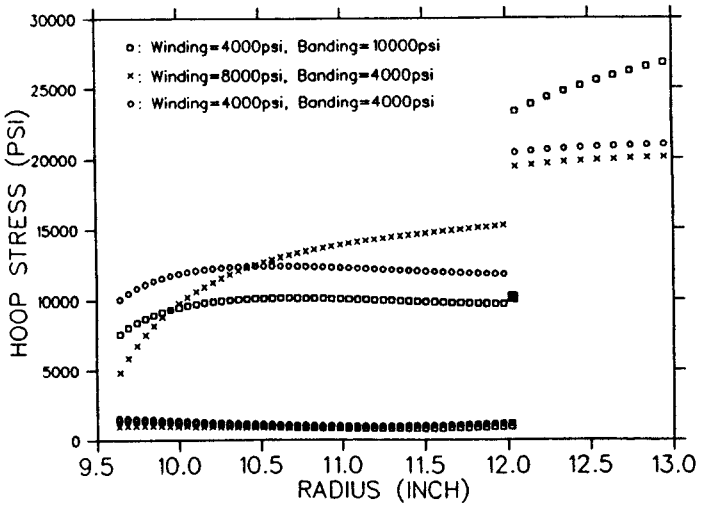

Fig. 3. Hoop stress distributions in the coil for three different combinations of pre-tension at 8-Tesla field when the coil is freed from the bobbin. The discrepancy at r= 12" is due to the coil banding. A group of low stresses (≈ 2000 psi) are on the epoxy and Formvar. The stresses on the conductor are around 10000 psi depending on preloads. The present choice is 4000 psi of winding pre-tension and 10000 psi of banding preloads. A stronger winding preload (8000 psi) only reduces hoop stress on the inner layers.

strongest. In this region, a small movement of the coil produces enough heat to cause magnet quenching because of the small heat capacity near 4K.[5] If we use a large pre-tension, we can, in principle, prevent the coil motion by a producing frictional force stronger than the axial one. However, the shear stress inevitably has a maximum value in corners because the coil is in tension axially and compression radially. As the opposite stresses are associated, the maximum shear stress is enhanced as the following equation shows,

$$\text{Maximum shear stress} = \left(\left[(\sigma_x - \sigma_y)/2 \right]^2 + \tau_{xy} \right)^{0.5},$$

where σ_x and σ_y are two normal stresses, and τ_{xy} is plane shear stress.

The coil is generally strong for compressive stress, but very weak for shear stress due to the structure of the winding. In addition, differential thermal contraction contributes to the stress along the circumferential direction [6] since Formvar insulation has a higher thermal contraction than the conductor. (The Stycast epxoy is filled and matched to the thermal contraction of the conductor) Estimated tensile stress on Formvar due to the differential thermal contraction amounts to 4000psi, the effect of which can be concentrated when combined with the shear stress mentioned above.[7] The equation and material properties are shown below,

$$\text{Thermal stress} : \sigma = \varepsilon_{\text{difference}} * Y_{\text{formvar}} \text{ (Ref.6)},$$

where

$$\varepsilon_{\text{difference}} = \alpha_{\text{formvar}} - \alpha_{\text{conductor}}, \quad \alpha = \text{thermal contraction coefficient, and}$$
$$Y_{\text{formvar}} \approx 5 \times 10^5 \text{ psi}, \quad \alpha_{\text{formvar}} \approx 1.0 \times 10^{-2} \text{(in/in)}, \quad \alpha_{\text{conductor}} = 3.0 \times 10^{-3} \text{(in/in)}$$

2) Free coil

In this case the hoop stress can be a problem because a relatively weak pre-tension is used to make the coil come free from bobbin. The enormous magnetic pressure is supported only by the circumferential strength of the conductor. To avoid this we use a stiff stainless steel banding (1" thick), resulting in a hoop stress under 15000 psi. But this banding adds another stress to the coil. As the coil is energized, radial and axial stresses on the coil boundary increase, giving a large shear stress as in tightly banded case. However, because the banding is composed of wires, the coil can move together with the banding axially, although more study of this effect is needed.

III. Quench protection

Because of the large stored energy density ($\approx$70 MJ/m^3 at 8 tesla) a quench could potentially damage a potted coil. The "hot spot" temperature at the quench-initiating point and voltage drop across the layers are estimated using QUENCH.[8] Three possible quench scenarios are assumed and evaluated respectively, namely: 1) both coils quench at the same time 2) one coil quenches, followed by the other coil due to mutual inductance, and 3) one coil quenches and the other one quenches when the current reaches the critical point. Scenario 3 is the worst case; however, it is unlikely because, when one coil quenches, the other follows immediately as the induced current in the unquenched coil rises higher than the operating current. Figure 4 shows an assumed 3 second delay in quenching (second scenario). The most likely cause of potted coil damage is known to be arcing due to the high voltage difference between layers. With 46 layers in an ordered winding the voltage between

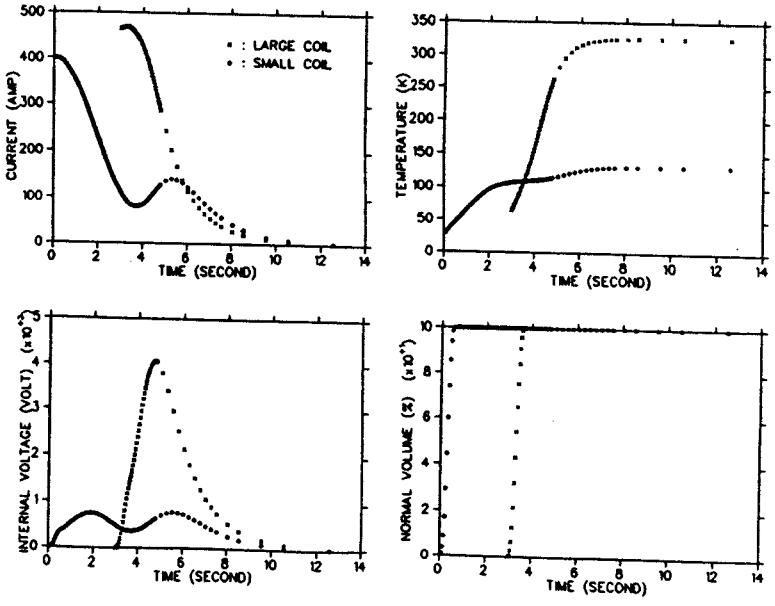

Fig. 4. Quench calculation in the case when the large coil quenches 3 seconds after the small coils.

adjacent layers is a maximum of 90 volts. Our coil has insulating paper between layers sufficient to support this voltage. A safe estimation must not depend strongly on the quench propagation velocity perpendicular to the wire because this is a largely unknown parameter. A velocity ratio of 7.5% is used for the results shown in Fig. 4. Larger and smaller ratios (5% and 10%) of velocities did not significantly change the results (less than 10%). Inductances for inputs to QUENCH are calculated from the stored energy computed from POISSON. As the actual inductance is a function of iron saturation, the value obtained by this method is only an averaged one. The difference between averaged and actual inductance is, however, thought to be insignificant at an 8-Tesla field.

IV. Support links

The electromagnetic force, which is self-cancelled in the case in which the coil is perfectly centered, can generate a large force on the coil support links when off-centered. Poisson is used to calculate the spring constant of the magnetic force for vertical off-centering, and a dipole moment method which considers the yokes and coils as dipoles is used to estimate the horizontal off-centering force.

G-10 has been tested for use as links. The high tensile strengh and low thermal conductivity make this material useful cryogenically. Ease of fabrication and better fitting to the available space leads us to test the joint strength of G-10 rather than S-glass wound links which has an intrinsically greater strength for the same cross sectional area. The major problem of the composite materials is that the breaking strength of joints is much lower than material itself, due to stress concentrations. Experiments to study this question are described below:

1) Experimental apparatus.

Devices used for the previous link test[9] could be used with some modifications of the sample holders. A hydraulic pump rather than the pneumatic pump allowed easier control of the sample tension. A 5/8" strain stud which has a maximum load of 9000 lbs was used in our tests. The strain stud used was tested to confirm the company supplied calibration, using the lab's big scale and crane.

2) Observations

The general characteristics are given in Table 1 for repeated testing of seven samples (Fig. 5).

Table 1. Observations of G-10 joint test

Applied load.	Observations
3100 lbs :	All samples are undamaged. Linear and reversible to this point
3400 lbs :	Gap between link pin and G-10 is enlarged. Stress concentration line is seen.
3700 lbs :	Stress concentration becomes clear. All samples are damaged.
3900 lbs :	Some of the fiber glass filamnets are broken (pinging sound) Several samples are broken at this load level.
4000 lbs :	All samples are broken.

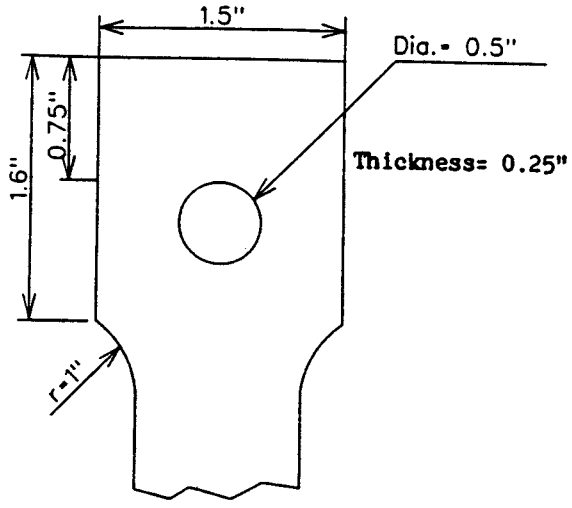

Fig. 5. Form and dimensions of support links.

3) Results of test

The ratio of rupture stress to the tensile stress of material gives the stress concentration factor of link. Since stress concentration factors for the composite material are not well known, we just used that of ordinary metal.[10] After a series of tests it was observed that composite materials also follow the same trend in stress concentrations seen in homogeneous materials, but the stress is more concentrated and the distance between link and the edge of G-10 more strongly affects the joint strength. Pin size could be optimized from the stress concentration curve. For example, the 1" wide material has an optimized pin size of 0.4" for the material following the stress concentration curve of Ref 10.

Another aim of this test was to compare the strength of two kinds of joints: 1) bolts and bonding (combination) joint, and 2) pin joint. The rupture strength of the combination joint was almost same as the bolt only. But a direct comparision with a pin joint was difficult because bolt size and their arrangement in a combination joint was not studied thoroughly so that the arrangement we used actually reduced the strength of the joint by concentrated stresses. The combination joint is generally assumed to have the greatest strength.[11] As the combination joint itself is a subject requiring study, we did not try any more. We are planning to test joint strength again after having the G-10CR which will be actually used for our link.

The test shows that we can safely apply a maximum load of 6000 lbs at the temperature (<77K) for our standard sample size. The spring constant for off-centering is about 71000 lbs/inch, and since three vertical links share the load, links can withstand off-centering of 0.25".

V. Winding test with aircraft cable

A mechanical property study and winding test of stainless steel cable was carried out as a preloaded banding material. One of the main reasons for testing the cable instead of rectangular wire for a coil banding is that the shear stress on the boundary between coil and banding can be reduced by keeping the banding soft axially.

Cable was wound using the same apparatus used for the Harper cyclotron coil and with the tensioner used for the K1200 coil winding. A simplified pusher arm to set a tight winding worked well in the dry winding, but in the wet winding, the cable sometimes slipped over the previous turn. We need to improve the design of the pusher for the later winding of the chosen banding material.

1) Young's modulus of cable

The stretch of a wire under load has two components, the structural stretch and the elastic stretch. Because the structural stretch initially dominates, the effective Young's modulus is low at the beginning. As the load is increased, the structural stretch ends, and the elastic modulus remains constant until the yield point (Fig. 6). A long gauge length (≈40 ft) amplified the overall displacement, which makes the measurement easier.

2) Young's modulus of the coil in the axial direction

The elastic modulus measurement in the coil's axial direction could be done with the help of the Forestry department. The load limit of the machine was 30000 lbs, which was enough for our soft coil. The test-coil dimensions were

$$\text{Cross-section} : \pi*(3.43^2 - 2.97^2) = 9.26 \ (\text{inch}^2)$$

Gauge length (axial dimension of coil) : 5.00"

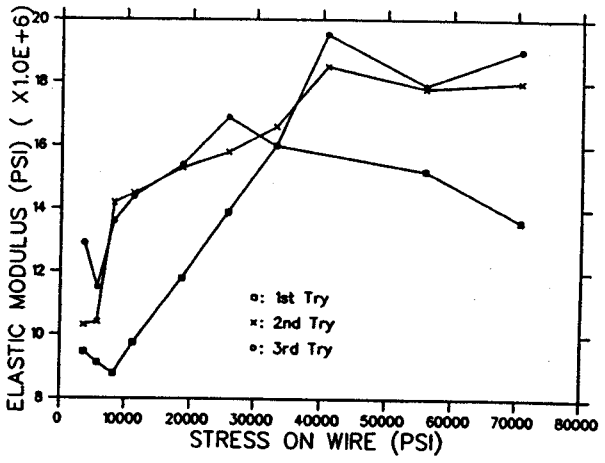

Fig. 6. Young's modulus for 1/16" aircraft wire as a function of applied stress. The wire is stretched as the test is repeated.

Table 2 shows the Young's modulus as well as the stress and strain. Young's modulus remains constant for the load change.

Table 2. Transverse Young's modulus for a coil wound with aircraft cable, as a function of applied load

Applied Load (lbs)	Increased Stress (psi)	Increased Strain	Young's modulus(psi)
6800 lbs	630	0.002	3.1E+5
12900 lbs	680	0.002	3.4E+5
19200 lbs	680	0.002	3.4E+5
25300 lbs	650	0.002	3.2E+5

3) Results of test

The softness in the coil's axial direction meets our requirement. However, the structural stretch makes the banding wound with cable inelastic for the initial loads. In other words, the banding in a real magnet is expected to stretch inelastically for the radial magnetic load because our pre-tension (10000 psi) is not sufficient to complete the initial structural stretch. For the "tightly banded coil" cable may be used after fully pre-stretching with high preloads. The cable is, however, excluded from our choices of banding material because of uncertain mechanical and thermal properties.

VI. Conclusion

The main effort has been given to the coil because that part is the core of magnet. Cryogen supply and return system, current leads, and other details are also being designed. We are now ready to construct the bobbin for the coil; in addition, test winding is planned to develop procedual details of the winding process.

References

1. M.T. Menzel, H.K. Stokes Poisson/Superfish Group of Codes, Los Alamos Nat'l Lab (1987)
2. ANSYS is a registered trademark of Swanson Analysis,Inc
3. J. Kim, et al, 8-tesla magnet for test stand, MSU Annual Report (1989), p192
4. W.H. Gray, DL. Levine, Oak Ridge National Lab (1976)
5. Y. Iwasa, Experimental and theoretical investigation of mechanical disturbances in epoxy-impregnated superconducting coils, Cryogenics (1985) V.25 June, p304
6. H Brechna, Superconducting Magnet Systems, Springer-Verlag, New York (1973)
7. E. Bobrov, J.E.C. Williams, Y. Iwasa, Experimental and theoretical investigation of mechanical disturbances in epoxy-impregnated superconducting coil. 2. Shear-stress-induced epoxy fracture as the principal source of premature quenches and training-theoretical analysis, Cryogenics V.25, June(1985)
8. M.N. Wilson, Computer simulation of the quenching of a superconducting magnet, RHEL/m 151
9. J. DeKamp, private communication
10. M. Frocht, H. Hill, Stress-concentration factors around a central circular hole in a plate loaded through pin in the hole, Jou. of Applied Mechanics, V.17, No.1, PA-5, March (1940)
11. R.P. Reed, A.F. Clark, Materials at low temperatures, ASM (1983), p445

FOUNDATIONS OF BEAM PHYSICS

Martin Berz

The effect of a particle optical device like an accelerator on the particles moving in it can be conveniently expressed by a map that relates the final values of all the coordinates $\vec{z}$ describing a particle to its final coordinates. These coordinates usually include two or three phase space pairs; in the case of beams consisting of several kinds of particles, charge and mass may also be included, and often the spin of the particle is also relevant.

Often one is also interested in the dependence of the final coordinates on a few parameters $\vec{\delta}$ describing certain aspects of the machine. Altogether, this can be summarized as

$$\vec{z}_f = \mathcal{M}(\vec{z}_i, \vec{\delta}) \tag{1}$$

Beam Physics systems can be characterized by the map being "weakly nonlinear"; the linear approximation is not good enough, yet the nonlinearities are weak enough to be treatable by various perturbative techniques. In that respect, Beam Physics lies between the textbook-like study of linear systems and the rather nonlinear effects that appear for example in plasma physics. An important aspect of any study of beam physics systems is that the accuracy to which the map has to be known and analyzed is usually rather high: in many cases, errors of less than 10^{-6} or even 10^{-10} are required. A significant step forward in meeting these very stringent criteria are the differential algebraic techniques, which allows the description of the map as a high order Taylor series of aberrations for even the most complicated realistic systems [1].

The map $\mathcal{M}$ has to be adjusted to satisfy certain needs dictated by the desired properties of the system. For example, in a mass spectrograph, the final position should depend strongly on the mass of the particle, but not on its initial velocities or energies, and the dependence on the initial position has to be minimized. In a storage ring, a repetitive application of the map of sometimes 10^9 times should still keep the particles contained. While these criteria are usually easily formulated, they are often hard to achieve in practice.

From now on, we want to concentrate on the study and design of repetitive structures like storage rings. In these systems, the linear case boils down to a straightforward study of the eigenvalue spectrum and is rather completely described by the Courant-Snyder theory [3]. A helpful side effect is that the

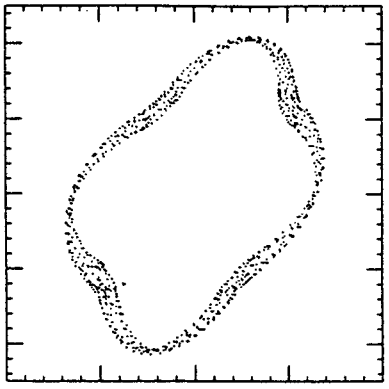

Figure 1: A Phase Space Plot of the Motion of a Particle in the SSC

Hamiltonian structure of the motion, which entails that the map $\mathcal{M}$ is symplectic, not only allows a simple decision about the stability, but it also assures stability under limited perturbations.

The higher order case, on the other hand, leads into the arena of nonlinear dynamics and the study of fixed points, invariants, ergodicity, chaos, and the quest for long term stability. Here we want to illustrate a new technique that allows a very accurate study and analysis of certain aspects of the long term behaviour of the motion. To begin our discussion, we look at a typical picture illustrating the motion in the contemplated Superconducting Supercollider. Figure 1 shows a Poincare section of the motion, i.e. a plot of position and momentum as the particle passes through a plane perpendicular to the beam axis repeatedly.

While being esthetically appealing, it is rather hard to draw sound conclusions from this picture. For example, it is hard to make predictions about the long term behaviour of the particle. Is the particle gently drifting outwards or inwards? Is its amplitude oscillating back and forth? If so, what is the frequency of this oscillation, and more importantly, is the amplitude of the oscillation growing in size?

Besides these qualitative questions, important quantities of the motion can only be extracted approximately. For example, it is only numerically possible to compute the tune of the particle (defined as the limit of total angular advance divided by turn number as turn number goes to infinity).

Normal Form Theory

It turns out that the complexity of the repetitive motion can be substantially reduced by expressing the motion in other canonical coordinates that are determined by the map:

$$\mathcal{M} = \mathcal{A} \circ \mathcal{N} \circ \mathcal{A}^{-1} \tag{2}$$

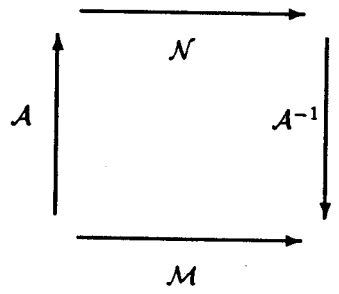

Figure 2: The Map $\mathcal{M}$ and the Adjoined Normal Form Map $\mathcal{N}$

The repetitive study may then be performed in the new coordinates because we obviously have

$$\mathcal{M}^n = \mathcal{A} \circ \mathcal{N}^n \circ \mathcal{A}^{-1} \tag{3}$$

In the linear case, suitable new coordinates are the real and imaginary parts of the eigenvectors, and the motion is reduced to circles with constant angular advance. This is a byproduct of the Courant - Snyder theory [3].

A simple argument reveals that the tune is just the frequency on the circles in the new coordinates; the total angular advance in the old coordinates can be expressed by one angular advance occurring while going to the new coordinates, the advance due to the repeated action of the map, and the advance that describes the transformation back to the old coordinates. In the limit of turns going to infinity, the angle advances due to the transformations become insignificant, and hence the tune is just the revolution frequency in the new coordinates.

Besides allowing a simple algebraic computation of the tune, the new coordinates readily provide an invariant of the motion; since the radius is preserved in the new coordinates, this radius expressed in the old coordinates is an invariant, the so-called Courant - Snyder invariant.

This very intuitive study characterizes the repetitive linear motion. In the nonlinear case, the situation becomes much more difficult and cannot be described as an eigenvalue problem anymore. In order to achieve a similar circular motion, nonlinear coordinate transformations are required.

Some fundamental ideas about this problem of the so-called normal form of nonlinear motion go back to the beginning of this century and the work of Birkhoff [4,5]. In recent years, major theoretical advances led to two applications of these techniques in accelerator physics. Dragt and Finn [6] provided the first steps for a Lie algebraic formulation of the theory. A first practical implementation of the techniques to low order Taylor maps was achieved by Neri [7]. Parallel to the work of Dragt and coworkers, similar results were achieved by Bazzani et al.[8]

With the appearance of the differential algebraic techniques [1,9,10], which for the first time allowed a computation of maps of to very high orders including parameter dependences, it was soon realized that it is possible to perform normal form transformations to arbitrary order. The resulting algorithm is based on the Lie algebraic techniques, and all the shortcomings of the Lie approach are remedied by differential algebraic methods [11].

Recently we could show [12,13] that it is possible to phrase the whole normal form algorithm in purely differential algebraic form without any Lie algebraic tools. The method again works to arbitrary order including parameter dependences, and for the first time it also allows the study of non-canonical systems.

The DA Normal Form Algorithm

The differential algebraic normal form algorithm consists of sequence of coordinate changes. The first of them transforms to the Courant - Snyder eigenvector coordinates and thus normalizes the linear motion. The subsequent transformation are nonlinear, each removing terms of higher order. This is not the place to dwell on the details of the algorithm; for this purpose we refer to Ref. 12, 13. We want to restrict our discussion to pointing out that for the removal of terms in the j th phase space pair of the map, the values of characteristic expressions of the following form are relevant:

$$(\prod_{l=1}^{n}(r_l)^{k_l^+ + k_l^-}) \cdot e^{i\vec{\mu}\cdot(\vec{k}^+ - \vec{k}^-)} - r_j \cdot e^{\pm i\mu_j} \tag{4}$$

where $\vec{r}$ are the moduli of the linear eigenvalues and $\vec{\mu}$ are their phases, which coincide with the linear tunes, and k_l^+, k_l^- are integers that lie between 1 and the current order. It turns out that a term of the map can be removed if the corresponding characteristic expression does not vanish. Clearly, in the j th coordinate pair, the terms corresponding to $k_j^+ = 1$, all others zero, and $k_l^- = 1$, all others zero, can not be

removed; these terms describe the linear circular Courant Snyder motion.

However, other combinations of $k_l^{\pm}$ can also lead to vanishing characteristic expressions; in particular, this happens if there are nontrivial choices of $\vec{n}$ that simultaneously satisfy

$$\begin{aligned} \vec{\mu} \cdot \vec{n} &= 0 \bmod 2\pi \\ \log(\vec{r}) \cdot \vec{n} &= 0. \end{aligned} \tag{5}$$

So the linear tunes of the system as well as the logarithms of the moduli of the linear eigenvalues should never lie on the same resonance.

Stable Symplectic Systems

All maps generated from Hamiltonian motions are symplectic. One consequence is that the maps are area preserving in phase space, i.e. they satisfy Liouville's theorem. That entails, however, that the product of all the moduli of the linear eigenvalues has to be unity. Since stable symplectic systems never have moduli larger than unity, all the moduli have to equal unity, and hence stable symplectic systems always lie on a modulus resonance. Thus terms cannot be removed if

$$k_+ = k_- \pm 1, \tag{6}$$

which is unavoidable, as well as if there are nontrivial solutions of

$$\vec{n} \cdot \vec{\mu} = 0 \bmod 2\pi \tag{7}$$

which characterizes tune resonances. The first condition leads to terms that entail a circular motion in the new coordinates, however with a frequency that depends on the amplitude. Like in the linear case, these frequencies are nothing but the tune, and hence the method allows the direct calculation of the important so-called amplitude dependent tune shifts.

In case the characteristic expression vanishes because of a tune resonance, the resulting motion will not be confined to a circle any longer; in this case, the motion will be deformed in a regular manner with a rotational symmetry corresponding to the order of the resonance.

In practice there are problems even in the non-resonant case because it is necessary to divide by the characteristic quantities. This entails large terms near resonances. However, since the resonance lines

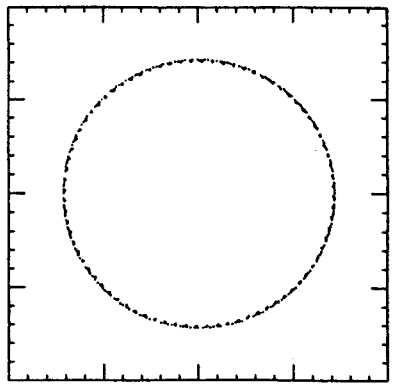

Figure 3: The Motion of Figure 1 displayed in Normal Form Coordinates

characterized by $\vec{n} \cdot \vec{\mu} = 0 \bmod 2\pi$ lie dense in tune space, for higher orders a small denominator problem is eventually unavoidable. This entails that the normal form algorithm does not necessarily converge as the order is increased. In practice, an optimum is often found around orders of 10; below the optimum, the transformation is not accurate enough, and above the optimum, the small denominator problem leads to divergencies.

The possible lack of asymptotic convergence has a rather interesting physical interpretation. In the case of convergence, the normal form motion is confined to perfect circles; hence the radius of the motion represents an invariant. For 2n dimensional systems, this produces n invariants, and hence the resulting system is integrable. However, it is well known and important that Hamiltonian systems do not have to be integrable.

Figure 3 shows the motion of Figure 1 displayed in symplectic nonresonant normal form coordinates. The motion is approximately confined to a circle; the small nonzero width of the circle is due to the lack of asymptotic convergence of the transformation.

Totally Damped Systems

Totally damped systems are characterized by the fact that all moduli of the eigenvalues of the linear map are less than unity. This entails that there are never any resonances, and the smallness of the terms in Eq. (4) is controlled by the strength of damping. Hence the small denominator problem limiting convergence is less severe and decreases with damping. The motion in the new coordinates follows regular exponential spirals collapsing into the fixed point.

Since all realistic beam physics systems experience some residual damping, the arguments developed in this section are valid asymptotically for any machine. In particular, the residual damping

limits the sensitivity to resonances of very high order.

References

1. M. Berz, "Differential algebraic description of beam dynamics to very high orders," Particle Accelerators 24, (1989), p 109.
2. M. Berz, "The Description of Particle Accelerators using High Order Perturbation Theory on Maps," in: M. Month (Ed), Physics of Particle Accelerators 1 (American Institute of Physics, 1989), p 961.
3. E.D. Courant and H.S. Snyder, "Theory of the alternating gradient synchrotron," Annals of Physics 3, (1958), p 1.
4. G. D. Birkhoff, Transactions American Mathematical Society 18, (1917), p 199.
5. G. D. Birkhoff, Acta Mathematica 43, (1927), p 1.
6. A. J. Dragt and J. M. Finn, "Normal form for mirror machine Hamiltonians," Journal of Mathematical Physics 20(12), (1979), p 2649.
7. Filippo Neri, Private communication.
8. A. Bazzani, P. Mazzanti, G. Servizi, and G. Turchetti, "Normal forms for Hamiltonian maps and nonlinear effects in a particle accelerator," Il Nuovo Cimento 102 B, N.1, (1988), p 51.
9. M. Berz, "Differential algebraic description and analysis of trajectories in vacuum electronic devices including spacecharge effects," IEEE Transactions on Electron Devices, 35-11, (1988), p 2002.
10. M. Berz, "Arbitrary order description of arbitrary particle optical systems," Nuclear Instruments and Methods A298, (1990), p 426.
11. E. Forest, M. Berz, and J. Irwin, " Normal form methods for complicated periodic systems: A complete solution using Differential algebra and Lie operators," Particle Accelerators 24, (1989), p 91.
12. M. Berz, " High-Order Computation and Normal Form Analysis of Repetitive Systems," in: M. Month (Ed), Physics of Particle Accelerators, American Institute of Physics, (1991).
13. M. Berz, "Differential algebraic formulation of normal form theory," submitted to Physical Review A15, (1991).

FIFTH- AND SEVENTH-ORDER MATRIX OPTICS CALCULATIONS USING THE CODE COSY-INFINITY

Kihun Joh, Martin Berz, Jerry Nolen

The differential algebraic method in the beam optic code COSY INFINITY [1] made it possible not only to calculate higher order maps to any order but also to introduce new optical elements easily. In this study our goal is to test and learn to use COSY INFINITY for higher order optics calculations of practical systems. A longer range goal is to use this code for high resolution magnetic spectrograph design. Here two nuclear microprobe beam systems with octupole and sextupole spherical aberration correctors, respectively, are studied to compare 5th and 7th order effects after eliminating 3rd and 4th order spherical aberrations.

Theory and system descriptions

It has been reported that two sextupoles, arranged so that their 2nd order effects cancel, can be used to correct cylindrically symmetric 3rd order spherical aberrations[2, 3]. With certain positions of the sextupoles it is also possible to avoid inducing 4th order spherical aberrations according to Vernon D. Beck[2] , H. Rose[3], and Alex J. Dragt[4]. Here one model solenoid was introduced into the code COSY INFINITY to be used to test the spherical aberration correctors. The soft-edge bump function model[4] was used for its simplicity and fast calculation of the field on the optic axis:

$$B(0,0,S) = \frac{B}{2}\left[\tanh(S/D) - \tanh(\frac{S-L}{D})\right]$$

Here L is the body length of the solenoid and D is a characteristic length describing fringe field. Figure 1 shows the behavior of the model field for three widths of fringe field tails along the optic axis. Note that B is not the maximum field inside the solenoid, and also this function falls off more rapidly than the well known bell-shaped Glaser field of the form:

$$B(0,0,S) = \frac{B_0}{1+(S/D)^2}$$

The system in Figure 2 which was proposed by H. Rose[3] to eliminate both 3rd and 4th order spherical aberrations simultaneously, consists of one objective solenoid(S3) and a sextupole spherical

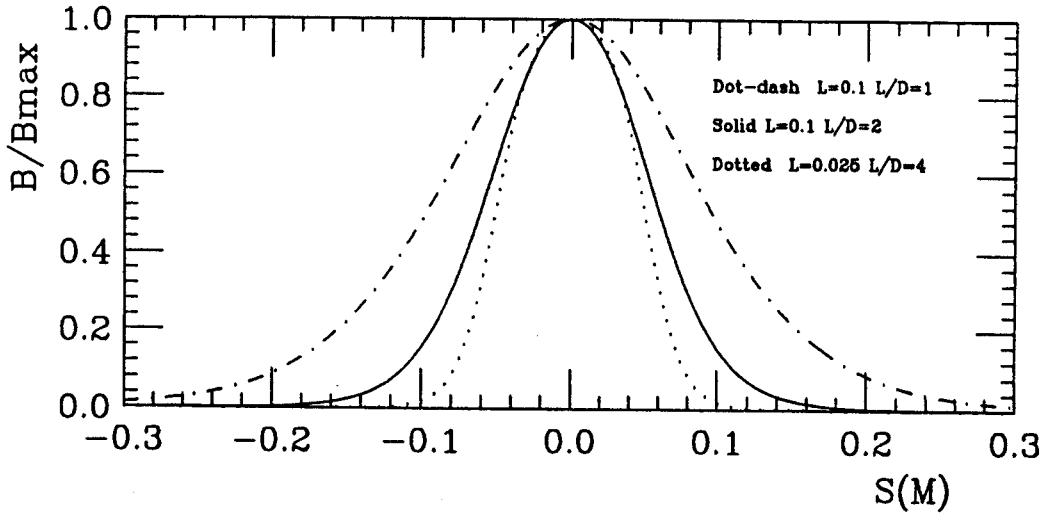

Figure 1: The B-field of the model solenoid along the optic axis S. Here the B_{max} is the maximum magnetic field strength inside the solenoid, corresponding to approximately 4.6 Tesla in this calculation.

aberration corrector. The objective solenoid gives final beam spots with needed demagnifications by the proper choice of drift lengths. The corrector part consists of two sextupoles and two identical solenoids which have magnetic fields of the same magnitude but opposite sign. The centers of the two sextupoles are at the focal points of the solenoids. The system in Figure 3 consists of one demagnifying solenoid plus an octupole spherical aberration corrector. The octupole corrector consists of an antisymmetric quadrupole quartet to give a negative unity matrix transform, and a pure octupole(O1) in the middle of the corrector. Also the second(M1) and the third quadrupole(M2) include equal octupole components. The two octupole parameters (the strength of O1 and the coupled strength of M1 and M2) are adjusted to correct (x, a^3) and (x, ab^2). By symmetry (y, b^3) and (y, a^2b) are also corrected.

COSY INFINITY calculation

The nuclear microprobe beam system has been chosen for this study because it needs a very accurate calculation in itself, and the higher order aberrations which are induced by the 3rd order corrections can be very large and usually are evaluated only via ray tracing calculations. This is especially true for aberrations beyond 5th order. For the calculation, a proton beam of 5 MeV kinetic energy was used with the initial phase space variables of $a_0 = b_0 = 0.001$. These values correspond to approximately 1 mr beam divergences for horizontal and vertical directions, respectively, in the code TRANSPORT notation. Also

a point source with no energy spread was used to study only spherical aberration effects. The solenoid parameters were B=10 Tesla, D=0.1 m and L=0.1 m to give about 4.6 Tesla peak field inside the solenoid in the Figure 1. This kind of magnet is similar to the microprobe at Los Almos [5]. The object to image ratios in the demagnification part were 10.827 for 10 to 1, and 21.35 for 20 to 1. Here object, image distances were defined from the center of the solenoid. The computational fittings for sextupole and octupole strengths were made to eliminate 3rd order spherical aberrations. The fitted magnetic multipole field strengths were relatively small values (less than 0.05 Tesla) for both sextupole and octupole correctors. The result of calculations in Table I shows that the 3rd order spherical aberrations in these microprobe forming systems must be removed if 1μm beam spots are needed. But the remaining 5th order aberrations are still not negligible in some cases(e.g. 50 to 1) even after removing the dominant 3rd order aberrations. The same thing might occur for the lower demagnification(e.g. 10 to 1) if larger beam divergences are accepted. For example in case of 50 to 1 the minimum spot size is already limited to μm due to the 5th order aberrations regardless of initial beam spot size. The situation becomes worse in the system containing the sextupole corrector due to a big 5th order aberrations. The smaller demagnification cases of 10 to 1, or 20 to 1 show the possibility of using aberration correctors to make microprobe beams with spot sizes of 1 μm or so. The system containing the octupole corrector has a resolution of less than 10 Å. The system containing the sextupole corrector seems to have relatively large 5th order aberrations. Figure 4 shows the effect of spherical aberrations up to 5th order for three different cases and actual beam spots with an initial finite beam spot radius of 10 μm. It is clear that the dominant geometrical aberrations are mainly spherical ones in this case. Table II and Table III show the effect of fringe fields in the solenoidal demagnifying systems. The slower fringe fields tails give the smaller spherical aberrations. This behavior is the opposite to the existing quadrupole microprobe systems[6].

Discussions and conclusions

The octupole spherical aberration corrector seems to be more effective than the sextupole corrector if it could be built without errors. The sextupole corrected system seems to produce large 5th order aberrations even after correcting the 3rd and the 4th order aberrations. In our system the 7th order effects were negligible for the 20 to 1 demagnification.

One interesting thing in this solenoid model is that the wider fields in Figure 1 have smaller

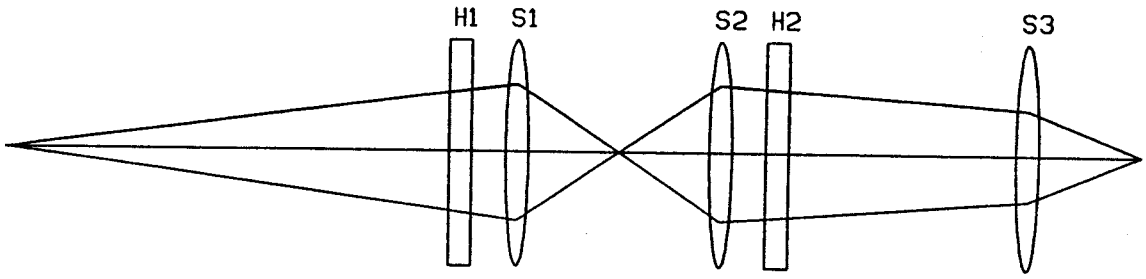

Figure 2: The microprobe forming system with a sextupole spherical aberration corrector. This figure is not to scale.

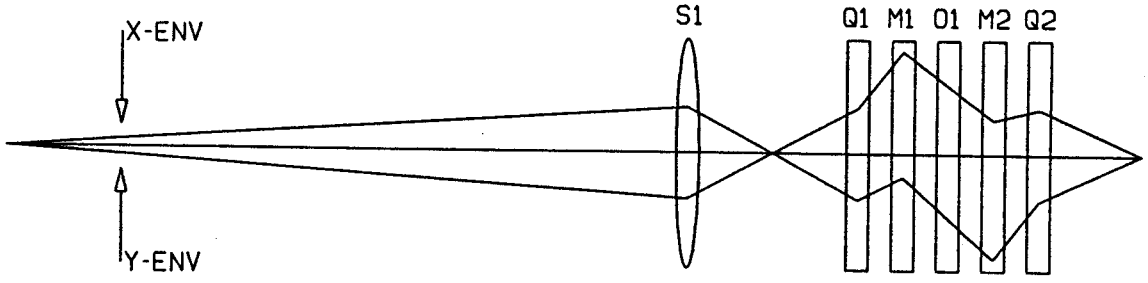

Figure 3: The microprobe forming system with an octupole spherical aberration corrector. This figure is not to scale.

higher order aberrations than the narrower fields; Table I and Table II imply the possibility of using an uncorrected solenoid for a microprobe beam spot, if the fringe field tail be made sufficiently long and the demagnification ratio be relatively small, i.e. 20 or less. This behavior is the opposite of quadrupole demagnifying systems, where fringe fields increase the higher order aberrations. The ability of COSY INFINITY to extend calculation order and its flexibility in using transfer maps repeatedly has been found powerful and useful in investigating systems requiring accurate and higher order calculations. Also the simple way of introducing new optical elements seems to be effective both for computer simulation at the design stage and for the academic study of optical systems containing new elements.

References

1. M. Berz, COSY INFINITY.3, a reference manual, NSCL Cyclotron Lab., Michigan State University, 1990.
2. Vernon D. Beck, Optik 53, (1979), p 241.
3. H. Rose, Nucl. Instr. and Meth.187, (1981) p 187.
4. Alex J. Dragt, Nucl. Instr. and Meth.A298, (1990).
5. C.J. Maggiore, Nucl. Instr. and Meth., 191, (1981).
6. G.W. Grime, F. Watt, Beam Optics of Quadrupole Probe-forming Systems (Adam Hilger Ltd, Bristol) 1984, p 83.

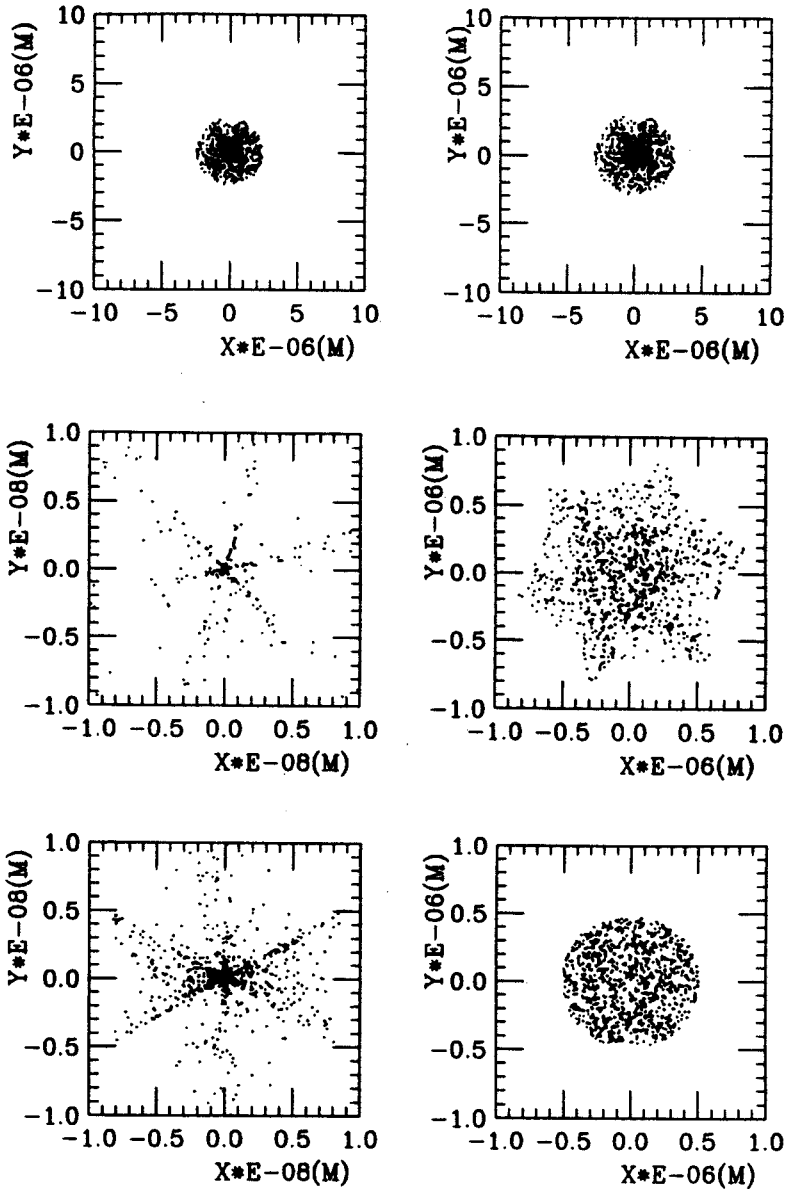

Figure 4: The beam spots for "uncorrected (top)," "sextupole corrected (middle)," and "octupole corrected (bottom)" systems up to 5th order calculations. The left side is for the point source, i.e. $x_0 = y_0 = 0$, $a_0^2 + b_0^2 = 0.001$, and the right side is for $x_0 = y_0 = 10\mu m$, $a_0^2 + b_0^2 = 0.001$ in the demagnification ratio of 20 to 1.

TABLE I. Spherical aberrations for three different cases. The number listed are the matrix elements multiplied by the initial phase space variables, $x_0 = y_0 = 0$ and $a_0 = b_0 = 0.001$.
(a) Demagnification ratio of 10 to 1.

Aberrations(m)	Uncorrected	Sextupole corrected	Octupole corrected
$(x,a^3)a_0^3$	-0.3540E-06	-0.1197E-12	-0.3540E-10
$(x,a^2b)a_0^2b_0$	-0.1042E-15	0.0000E+00	-0.3357E-16
$(x,ab^2)a_0b_0^2$	-0.3540E-06	-0.1197E-12	-0.3550E-10
$(x,b^3)b_0^3$	-0.1042E-15	0.0000E+00	-0.3330E-16
$(x,a^4)a_0^4$	0.0000E+00	-0.6977E-10	0.0000E+00
$(x,a^3b)a_0^3b_0$	0.0000E+00	0.1070E-15	0.0000E+00
$(x,a^2b^2)a_0^2b_0^2$	0.0000E+00	0.8372E-10	0.0000E+00
$(x,ab^3)a_0b_0^3$	0.0000E+00	0.0000E+00	0.0000E+00
$(x,b^4)b_0^4$	0.0000E+00	0.4186E-10	0.0000E+00
$(x,a^5)a_0^5$	-0.7931E-10	0.1081E-07	0.2939E-09
$(x,a^4b)a_0^4b_0$	-0.3240E-10	0.1625E-07	-0.3222E-14
$(x,a^3b^2)a_0^3b_0^2$	-0.1586E-09	0.9210E-08	0.1042E-08
$(x,a^2b^3)a_0^2b_0^3$	-0.6480E-10	-0.3251E-07	-0.6471E-14
$(x,ab^4)a_0b_0^4$	-0.7931E-10	0.1494E-07	0.2235E-09
$(x,b^5)b_0^5$	-0.3240E-10	0.3251E-08	-0.3249E-14

(b) Demagnification ratio of 20 to 1.

Aberrations(m)	Uncorrected	Sextupole corrected	Octupole corrected
$(x,a^3)a_0^3$	-0.2450E-05	0.3596E-14	-0.2900E-10
$(x,a^2b)a_0^2b_0$	-0.7181E-15	-0.2034E-15	-0.2528E-15
$(x,ab^2)a_0b_0^2$	-0.2450E-05	0.3598E-14	0.2567E-10
$(x,b^3)b_0^3$	-0.7181E-15	-0.2033E-15	-0.2499E-15
$(x,a^4)a_0^4$	0.0000E+00	-0.6285E-09	0.0000E+00
$(x,a^3b)a_0^3b_0$	0.0000E+00	0.2179E-14	0.0000E+00
$(x,a^2b^2)a_0^2b_0^2$	0.0000E+00	0.7542E-09	0.0000E+00
$(x,ab^3)a_0b_0^3$	0.0000E+00	0.0000E+00	0.0000E+00
$(x,b^4)b_0^4$	0.0000E+00	0.3771E-09	0.0000E+00
$(x,a^5)a_0^5$	-0.2061E-08	0.2970E-06	0.7455E-08
$(x,a^4b)a_0^4b_0$	-0.8409E-09	0.4566E-06	-0.4749E-13
$(x,a^3b^2)a_0^3b_0^2$	-0.4122E-08	0.3300E-06	0.3048E-07
$(x,a^2b^3)a_0^2b_0^3$	-0.1682E-08	-0.9131E-06	-0.3865E-13
$(x,ab^4)a_0b_0^4$	-0.2061E-08	0.3850E-06	0.7523E-08
$(x,b^5)b_0^5$	-0.8409E-09	0.9131E-07	0.8812E-14

(c) Demagnification ratio of 50 to 1.

Aberrations(m)	Uncorrected	Sextupole corrected	Octupole corrected
$(x,a^3)a_0^3$	-0.3506E-04	-0.1847E-12	-0.1583E-09
$(x,a^2b)a_0^2b_0$	-0.1035E-13	-0.3774E-14	-0.3705E-14
$(x,ab^2)a_0b_0^2$	-0.3506E-04	-0.1847E-12	0.7364E-10
$(x,b^3)b_0^3$	-0.1035E-13	-0.3772E-14	-0.3656E-14
$(x,a^4)a_0^4$	0.0000E+00	-0.1058E-07	0.0000E+00
$(x,a^3b)a_0^3b_0$	0.0000E+00	0.3399E-14	0.0000E+00
$(x,a^2b^2)a_0^2b_0^2$	0.0000E+00	0.1270E-07	0.0000E+00
$(x,ab^3)a_0b_0^3$	0.0000E+00	-0.6538E-15	0.0000E+00
$(x,b^4)b_0^4$	0.0000E+00	0.6349E-08	0.0000E+00
$(x,a^5)a_0^5$	-0.1776E-06	0.2666E-04	0.6321E-06
$(x,a^4b)a_0^4b_0$	-0.7239E-07	0.4144E-04	-0.1285E-11
$(x,a^3b^2)a_0^3b_0^2$	-0.3551E-06	0.3419E-04	0.2828E-05
$(x,a^2b^3)a_0^2b_0^3$	-0.1448E-06	-0.8289E-04	-0.1131E-11
$(x,ab^4)a_0b_0^4$	-0.1776E-06	0.3305E-04	0.7482E-06
$(x,b^5)b_0^5$	-0.7239E-07	0.8289E-05	0.1523E-12

TABLE II. The effect of the fringe fields on the spherical aberrations in the solenoid system with the demagnification ratio of 20 to 1. The aberrations were multiplied by initial phase space variables, a=b=0.001 and x=y=0.

Aberrations	L/D = 1	L/D = 2	L/D = 4
$(x,a^3)a_0^3$	-0.2450E-05	-0.1294E-04	-0.2115E-04
$(x,a^2b)a_0^2b_0$	-0.7181E-15	-0.2149E-15	-0.4237E-15
$(x,ab^2)a_0b_0^2$	-0.2450E-05	-0.1294E-04	-0.2115E-04
$(x,b^3)b_0^3$	-0.7181E-15	-0.2149E-15	-0.4237E-15
$(x,a^5)a_0^5$	-0.2061E-08	-0.3424E-07	-0.8765E-07
$(x,a^4b)a_0^4b_0$	-0.8409E-09	-0.5874E-08	-0.1056E-07
$(x,a^3b^2)a_0^3b_2$	-0.4122E-08	-0.6847E-07	-0.1753E-06
$(x,a^2b^3)a_0^2b_0^3$	-0.1682E-08	-0.1175E-07	-0.2113E-07
$(x,ab^4)a_0b_0^4$	-0.2061E-08	-0.3424E-07	-0.8765E-07
$(x,b^5)b_0^5$	-0.8409E-09	-0.5874E-08	-0.1056E-07

TABLE III. The higher order fringe field effect in the "sextupole corrected" system with the demagnification ratio of 20 to 1. Aberrations were multiplied by initial phase space variables, a=b=0.001 and x=y=0. The aberrations up to 3rd order have been eliminated.

Aberrations	L/D = 1	L/D = 2	L/D = 4
$(x,a^4)a_0^4$	-0.6285E-09	-0.3922E-08	-0.1101E-07
$(x,a^3b)a_0^3b_0$	0.2174E-14	0.9971E-15	-0.7733E-15
$(x,a^2b^2)a_0^2b_0^2$	0.7542E-09	0.4706E-08	0.1321E-07
$(x,ab^3)a_0b_0^3$	-0.7840E-16	-0.2758E-16	-0.1114E-14
$(x,b^4)b_0^4$	0.3771E-09	0.2353E-08	0.6606E-08
$(x,a^5)a_0^5$	0.2970E-06	0.1032E-04	0.5618E-04
$(x,a^4b)a_0^4b_0$	0.4566E-06	0.5501E-05	0.1707E-04
$(x,a^3b^2)a_0^3b_0^2$	0.3300E-06	-0.1426E-04	-0.9349E-04
$(x,a^2b^3)a_0^2b_0^3$	-0.9131E-06	-0.1100E-04	-0.3414E-04
$(x,ab^4)a_0b_0^4$	0.3850E-06	0.2196E-04	0.1248E-03
$(x,b^5)b_0^5$	0.9131E-07	0.1100E-05	0.3414E-05
$(x,a^6)a_0^6$	0.1684E-08	0.9610E-07	0.7127E-06
$(x,a^5b)a_0^5b_0$	0.1432E-08	0.2773E-07	0.1167E-06
$(x,a^4b^2)a_0^4b_0^2$	-0.1099E-08	-0.6857E-07	-0.5120E-06
$(x,a^3b^3)a_0^3b_0^3$	0.1479E-08	0.2910E-07	0.1231E-06
$(x,a^2b^4)a_0^2b_0^4$	-0.3539E-08	-0.2059E-06	-0.1529E-05
$(x,ab^5)a_0b_0^5$	0.4741E-10	0.1364E-08	0.6406E-08
$(x,b^6)b_0^6$	-0.7561E-09	-0.4121E-07	-0.3045E-06
$(x,a^7)a_0^7$	0.8788E-09	0.8510E-07	0.9778E-06
$(x,a^6b)a_0^6b_0$	-0.2293E-09	-0.4314E-07	-0.3366E-06
$(x,a^5b^2)a_0^5b_0^2$	0.1395E-08	0.4889E-06	0.6329E-05
$(x,a^4b^3)a_0^4b_0^3$	0.1399E-08	0.1368E-06	0.9873E-06
$(x,a^3b^4)a_0^3b_0^4$	0.2898E-08	0.1781E-06	0.1952E-05
$(x,a^2b^5)a_0^2b_0^5$	-0.1916E-09	-0.7545E-08	-0.1055E-07
$(x,ab^6)a_0b_0^6$	0.9296E-09	0.8490E-07	0.9274E-06
$(x,b^7)b_0^7$	0.9242E-10	0.6928E-09	-0.3694E-08

RELEASE OF "COSY INFINITY"

Martin Berz

In the last years there has been a considerable advance in the ability to compute high order maps of accelerators and optical systems, providing new insight and accuracy that could not be reached previously [1,2,3]. COSY INFINITY [4,5,6] is a new generation design and simulation code for particle accelerators, guidance systems and spectrometers utilizing the new techniques. The first full release of the code was made available in October 1990 in connection with the East Lansing Workshop on High Order Effects in Accelerators and Particle Optics [4]. In the meantime, another extended version has been released [5].

COSY allows the computation and manipulation of maps of arbitrary systems including fringe fields and other varying fields to arbitrary order, including the dependence on system parameters. Maps can be analyzed and manipulated in a variety of ways, including the new normal form techniques [7,8,9]. COSY's object oriented language concept allows to phrase very complicated layouts, boundary conditions, optimizations strategies and control requirements in a very natural way and also provides a very powerful environment to treat general problems with differential algebraic methods. Besides its analytical power, the code allows a highly interactive, graphics based study and design of systems.

The Code COSY INFINITY

Differential algebraic methods [1,3] allow a very efficient and direct computation of very high order properties even for very complicated systems. In practice, this requires efficient implementations of DA methods, which represents several challenges. The most important of these is probably an efficient addressing scheme for the differential algebraic multiplication, as well as the techniques to handle sparse vectors; details about these problems can be found in Refs. 1, 10, 11.

An efficient differential algebra package represents the first step towards the computation and analysis of maps. The second step is a driver code utilizing the package and providing a user interface. COSY INFINITY [5,6,12] is such a driver code written in standard FORTRAN 77. Its command language is unique in that it actually represents a complete programming language. It has object oriented features which allow direct use of the differential algebraic data type and makes DA very manageable. The language is so general and powerful that even most parts of the physics code of COSY INFINITY are

written in it.

A full language environment provides the user with utmost power to express nontrivial tasks. Yet at the same time, because of the conciseness of modern languages, it is easy to learn, usually easier than that of other code command languages.

This is not the place to provide a more comprehensive description of the abilities of the code. For this purpose we refer to the manual [5] some examples of the use of the code can be found in Ref. 13; a description of some aspects of the physics of the code is contained in Ref. 6.

Distribution of the Code

The code COSY INFINITY is distributed through Michigan State University. The licensing is handled through the Academic Computing and Technology group in the MSU Computer Center. Currently, Universities and non-profit research institutions can obtain COSY INFINITY free of charge, whereas profit-making institutions can obtain yearly or indefinite licenses for the code at a charge payable to MSU. At present, there are about 60 registered users of COSY INFINITY. Implementations of COSY INFINITY exist at the following outside institutions:

Argonne National Laboratory

Atomic Energy of Canada Ltd., Chalk River

BESSY, Berlin

Brookhaven National Laboratory

CEBAF, Newport News

CERN, Geneva

California State University, Los Angeles

DESY, Hamburg

Fritz Haber Institut, Berlin

GANIL, Caen

GSI, Darmstadt

KFA, Juelich

Krasnojarsk Polytechnical Institute

Lawrence Berkeley Laboratory

Los Alamos National Laboratory

MIT Bates Laboratory, Boston

MPI Heidelberg

POSTECH, Korea

Paul Scherrer Institute, Villingen

Soviet Academy of Sciences, Leningrad

Soviet Academy of Sciences, Novosibirsk

Stanford Linear Accelerator Center

TRIUMF

Texas A+M, College Station

Texas Tech

Universite Laval

University of Beijing

University of Berlin

University of Bochum

University of Bonn

University of Frankfurt

University of Giessen

University of Groningen

University of Saskatchewan

University of Wisconsin

Wilson Laboratory, Cornell University

We are currently processing about 20 more license registrations. The new institutions involved are

Boeing, Seattle

CEA, Saclay

Grumman Aerospace, Princeton

Indiana University Cyclotron Facility

Interatom, Bergisch Gladbach

SSC Laboratory, Dallas

University of California Los Angeles

Varian Associates, Palo Alto

References

1. M. Berz, "Differential algebraic description of beam dynamics to very high orders," Particle Accelerators 24, (1989), p 109.
2. M. Berz, "Differential algebraic description and analysis of trajectories in vacuum electronic devices including spacecharge effects," IEEE Transactions on Electron Devices 35-11, (1988), p 2002.
3. M. Berz, "Arbitrary order description of arbitrary particle optical systems," Nuclear Instruments and Methods A298, (1990), p 426.
4. M. Berz, COSY INFINITY Version 3 reference manual, Technical Report MSUCL-751, National Superconducting Cyclotron Laboratory, Michigan State University, East Lansing, MI 48824, (1990).
5. M. Berz, COSY INFINITY Version 4 reference manual, Technical Report MSUCL-771, National Superconducting Cyclotron Laboratory, Michigan State University, East Lansing, MI 48824, (1991).
6. M. Berz, "Computational aspects of design and simulation: COSY INFINITY," Nuclear Instruments and Methods A298, (1990), p 473.
7. A. J. Dragt and J. M. Finn, "Normal form for mirror machine Hamiltonians," Journal of Mathematical Physics 20(12), (1979), p 2649.
8. E. Forest, M. Berz, and J. Irwin, "Normal form methods for complicated periodic systems: A complete solution using Differential algebra and Lie operators.," Particle Accelerators 24, (1989), p 91.
9. M. Berz, "High-Order Computation and Normal Form Analysis of Repetitive Systems," in: M. Month (Ed), Physics of Particle Accelerators, American Institute of Physics, (1991).
10. M. Berz, "Forward algorithms for high orders and many variables," Automatic Differentiation of Algorithms: Theory, Implementation and Application, SIAM Conference Proceedings, (1991).
11. M. Berz, "Differential algebra precompiler version 3 reference manual," Technical Report MSUCL-755, Michigan State University, East Lansing, MI 48824, (1990).
12. M. Berz, "COSY INFINITY, an arbitrary order general purpose optics code," Computer Codes and the Linear Accelerator Community, Los Alamos LA-11857-C, (1990), p 137.
13. M. Berz, COSY INFINITY, in Proceedings 1991 Particle Accelerator Conference, San Francisco, CA, 1991.

RETROACTIVE CORRECTION OF SPECTROGRAPHS

M. Berz, K. Joh, J. Nolen, B. Sherrill, A. Zeller

A new method is presented that allows the reconstruction of trajectories and the on-line correction of residual aberrations that limit the resolution of particle spectrographs. Using a computed or fitted high order transfer map that describes the uncorrected aberrations of the spectrograph under consideration, it is possible to determine a pseudo transfer map that allows the computation of the corrected data of interest as well as the reconstructed trajectories in terms of position measurements in two planes near the focal plane. The technique is only limited by the accuracy of the position measurements and the accuracy of the transfer map. In practice the method can be expressed as an inversion of a pseudo transfer map and implemented in the differential algebraic framework. The method will be used to correct residual high order aberrations in the S800 spectrograph [1,2] which is under construction at NSCL.

Introduction

Efficient modern high-resolution mass spectrographs like the S800 often offer rather large phase space acceptances. Such large acceptance high resolution spectrographs usually require a careful consideration and correction of aberrations. But because of the large phase space acceptance, effects of rather high orders contribute. This makes the correction process often considerably more difficult and complex, and often even prevents a complete correction of aberrations in the conventional sense.

It is often possible to circumvent or at least alleviate these problems by using additional information about the particles. In particular, one often measures not only their final position but also their final angle by means of a second detector. With this additional information, it is to some degree possible to retroactively construct the whole trajectory of the particle. This information can be used both for the numerical correction of the quantities of interest, but it also reveals additional properties like the initial angle, which is of course crucial for the study of many nuclear processes.

In the past such trajectory reconstruction techniques were quite involved, often requiring extensive ray tracing and the storage of large arrays of ray data and extensive interpolation. Here we present a rather direct and efficient method based on differential algebraic (DA) techniques.

In recent years we have shown that maps of particle optical systems can be computed to much

higher orders than previously possible using DA methods [3,4,5,6]. Furthermore, the techniques also allow the accurate treatment of very complicated fields that can be treated only approximately otherwise. In our particular case, these include the fringe fields of the large aperture magnets required for such particle spectrographs. So for the first time there is now the possibility to really compute all the aberrations that comprise a modern high resolution spectrograph without having to rely on tedious ray tracing.

On the practical side this requires high order codes for the computation of highly accurate maps for realistic fields. The new code COSY INFINITY [7,8,9,10] allows such computations in a very powerful language environment. It also has extensive and general optimization capabilities, supports interactive graphics and provides ample power for customized problems, and it provides all the necessary tools for efficient trajectory reconstruction.

Inversion of Transfer Maps

At the core of the contemplated trajectory reconstruction technique is the need to invert transfer maps in their DA representation. To this end, we begin by splitting the map A_n into its linear and nonlinear parts:

$$A_n = A_{1n} + A_{2n}. \tag{1}$$

Furthermore, we write the sought for inverse as M_n. Composing the functions, we obtain

$$\begin{aligned} (A_1 + A_{2n}) \circ M_n &= E_n \Rightarrow \\ A_1 \circ M_n &= E_n - A_{2n} \circ M_n \Rightarrow \\ M_n &= A_1^{-1} \circ (E_n - A_{2n} \circ M_{n-1}). \end{aligned} \tag{2}$$

Here "$\circ$" stands for the composition of maps. In the last step use has been made of the fact that to order n, $A_{2n} \circ M_n = A_{2n} \circ M_{n-1}$. This allows an iterative computation of the inverse order by order. Obviously the existence of the inverse of the linear part A_1^{-1} is necessary and sufficient for the existence of the total inverse of the map.

Trajectory Reconstruction

The result of the computation of the transfer map of the system allows us to relate final quantities

to initial quantities and parameters. In our case, the relevant quantities are the positions in x and y directions as well as the normalized momenta p_x/p_0, p_y/p_0 and the energy of the particles under consideration. Usually the initial x, which is determined by the target thickness or a subsequent slit, is kept small to provide a minimal entrance width. So the final positions and slopes are primarily determined by the energy, and to higher orders also by the initial y position and the initial slopes.

In the full transfer map we now set x_i to zero and consider the following submap:

$$\begin{pmatrix} x_f \\ a_f \\ y_f \\ b_f \end{pmatrix} = \mathcal{S} \begin{pmatrix} a_i \\ y_i \\ b_i \\ d \end{pmatrix} \tag{3}$$

This map relates the quantities which can be measured in the two planes to the quantities of interest. The map $\mathcal{S}$ is not a regular transfer map, and in particular its linear part does not have to be a priori invertible. In a well designed particle spectrograph, the linear part has the following form:

$$\begin{pmatrix} x_f \\ a_f \\ y_f \\ b_f \end{pmatrix} = \begin{pmatrix} 0 & 0 & 0 & * \\ * & 0 & 0 & * \\ 0 & * & * & 0 \\ 0 & * & * & 0 \end{pmatrix} \cdot \begin{pmatrix} a_i \\ y_i \\ b_i \\ d_i \end{pmatrix} \tag{4}$$

where a star denotes an entry that is not zero. Since the system is imaging, clearly (x,a) vanishes, and all the other zero terms vanish because of midplane symmetry. (x,d) is maximized in spectrograph design, and (a,a) cannot vanish in an imaging system because of symplecticity. In fact, to reduce the effect of the finite size entrance slit, (x,x) is minimized within the constraints, and so (a,a) = 1/(x,x) is also maximized.

Because of symplecticity, (y,y)(b,b)-(y,b)(b,y) = 1, and so we obtain for the total determinant of S:

$$|\mathrm{S}| = (x, d) \cdot (a, a) \neq 0, \tag{5}$$

besides being nonzero, the size of the determinant is also a good measure of the quality of the spectrograph: the larger the better.

So certainly the linear matrix is invertible, and according to the last section, this entails that the whole nonlinear map $\mathcal{S}$ is invertible to arbitrary order, and thus it is possible to compute the initial quantities of interest to arbitrary order.

Table 1: The S800 Spectrograph

Drift	l = 60 cm		
Quad	l = 40 cm,	G_{max} = 21 T/m ,	d = .1 m
Drift	l = 20 cm		
Quad	l = 40 cm,	G_{max} = 6.8 T/m,	d = .2 m
Drift	l = 50 cm		
Dipole	r = 2.6667 m,	$B_{max} = 1.5T$,	ϕ = 75 deg,
	ϵ_1 = 0 deg,	ϵ_2 = 30 deg	
Drift	l = 140 cm		
Dipole	r = 2.6667 m,	$B_{max} = 1.5T$,	ϕ = 75 deg,
	ϵ_1 = 30 deg,	ϵ_2 = 0 deg	
Drift	l = 257.5 cm		

A closer inspection of the algorithm shows that in each iteration, the result is multiplied by the inverse of the linear matrix S. Since the determinant of this inverse is the inverse of the original determinant and is thus small in a well designed spectrograph, this entails that the originally large terms in the nonlinear part of the original map are more and more suppressed. So clearly even with trajectory construction, the original investment in the quality of the spectrograph, which is determined by its dispersion and its x demagnification, directly influences the quality of the trajectory reconstruction.

Correction of Aberrations in Spectrographs

The proposed superconducting magnetic spectrograph, the S800[1,2] shown in fig. 1, will allow the study of heavy ion reactions with magnetic rigidities of up to 1.2 GeV/c. It will have an energy resolution of one part in 10000 with a large solid angle of about 20 msr and an energy acceptance of about 10 percent. The spectrograph will be used in connection with the K1200 to analyze beams of protons up to uranium with energies of 2 to 200 MeV/u. It will provide unique opportunities for research in various areas, including the study of giant resonances, charge exchange, direct reaction studies and fundamental investigations of nuclear structure [1,2].

The S800 consists of two superconducting quadrupoles and two 75 degree dipoles with y-focusing edge angles. Table 1 lists the parameters of the system. Standard particle optics notation is used.

After a careful measurement of the crucial fringe fields of the dipoles, we will be using COSY INFINITY to determine the high order properties of the map of the spectrograph. The computation of the map S from the resulting transfer map can be performed directly within the COSY environment, and

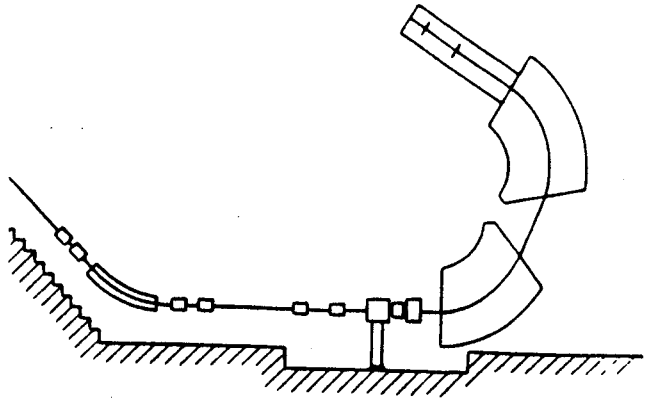

Figure 1: The vertical layout of the S800 spectrograph

so can the inversion of the map $\mathcal{S}$. Altogether, a correction map $\mathcal{S}$ is found, the nonlinearity of which is determined by the nonlinearity of the original map and the quality in the spectrograph measured by (x,d)/(x,x). It is anticipated that the correction map can be used for an on line determination of the relevant data without having to store the raw two plane position measurements.

In closing we would like to note that the method can also be employed for spectrographs for which no sufficient field measurements are known. To this end, one has to perform experimental ray tracing and fit the resulting data with a polynomial type transfer map. In this case, the inversion can still be done in the map picture resulting in a rather compact representation of the data necessary for correction.

References

1. J. Nolen, A.F. Zeller, B. Sherrill, J. C. DeKamp, and J. Yurkon, A proposal for construction of the S800 spectrograph. Technical Report MSUCL-694, National Superconducting Cyclotron Laboratory, (1989).
2. L. H. Harwood A. F. Zeller, J. A. Nolen and E. Kashy, "The MSU 1.2 GeV/c spectrograph," Workshop on High Resolution, Large Acceptance Spectrometers, ANL/PHY-81-2, Argonne National Laboratory, (1982).
3. M. Berz, "Arbitrary order description of arbitrary particle optical systems," Nuclear Instruments and Methods A298, (1990), p 426.
4. M. Berz, "Differential algebraic description of beam dynamics to very high orders," Particle Accelerators 24, (1989), p 109.
5. M. Berz, "Differential algebraic treatment of beam dynamics to very high orders including applications to spacecharge," AIP Conference Proceedings 177, (1988), p 275.
6. M. Berz, "Differential algebraic description and analysis of trajectories in vacuum electronic devices including spacecharge effects," IEEE Transactions on Electron Devices 35-11, (1988), p 2002.
7. M. Berz, COSY INFINITY Version 3 reference manual, Technical Report MSUCL-751, National Superconducting Cyclotron Laboratory, Michigan State University, East Lansing, MI 48824, (1990).

8. M. Berz, "Computational aspects of design and simulation: COSY INFINITY," Nuclear Instruments and Methods A298, (1990), p 473.
9. M. Berz, "COSY INFINITY, an arbitrary order general purpose optics code," Computer Codes and the Linear Accelerator Community, Los Alamos LA-11857-C, (1990), p 137.
10. M. Berz, "COSY INFINITY," in Proceedings 1991 Particle Accelerator Conference, San Francisco, CA, (1991).
11. N. Anantaraman and B. Sherrill, Editors, Proceedings of the international conference on heavy ion research with magnetic spectrographs, Technical Report MSUCL-685, National Superconducting Cyclotron Laboratory, (1989).

WORKSHOP ON HIGH ORDER EFFECTS

Martin Berz and Jean McIntyre

From October 29 through 31, NSCL and the Department of Physics and Astronomy hosted the workshop "High Order Effects in Accelerators and Beam Optics". Recent years have seen a growing interest in the description and analysis of nonlinearities of high orders. In particle accelerators, this allows a more detailed description of the maps describing the motion; in spectrographs it allows the analysis of residual high order aberrations, in particular for devices with large phase space acceptances. Especially the new differential algebraic methods have proven very successful for the description and analysis of systems to high order.

The workshop consisted of a total of 21 invited 30 minute talks, a sequence of demonstrations of the new differential algebraic code COSY INFINITY, and some time for discussions. There was a conference dinner at Wharton Center, followed by a performance of the Japan Philharmonic. The proceedings of the workshop, edited by M. Berz and J. McIntyre, appeared in April 91 as MSUCL-767. They cover the following talks:

1. Codes of The Future

   (a) Karl Brown, What I Think New Optics Codes Should Do

   (b) R. Servranckx, Future Plans for Tracking Studies of the TRIUMF Kaon Rings

   (c) D. Carey, The Science Fiction of Beam Optics Computer Programs

   (d) M. Berz, The Philosophy of COSY INFINITY

2. High Order Map Techniques

   (a) S. Douglas, Another Viewpoint on DA

   (b) L. Michelotti, C++ Objects for Exploratory Orbit Analysis

   (c) Y. Yan, ZLIB - A Numerical Library for Differential Algebra and Lie Algebra

3. Single Pass Systems

   (a) R. Degenhardt, A Compact Aberration-free Imaging Filter with Inside Energy Selection

(b) J. Nolen, Sextupoles Versus Octupoles for Third Order Corrections

(c) B. Sherrill, Heavy Ion Fragment Separation

(d) F. Neri, Higher Order Achromats and Normal Forms

(e) A. Zeller, Applications of COSY INFINITY to Spectrometer Design

4. Multi Pass Systems

(a) S. Martin, Nonlinearities in the Lattice of the COSY Cooler Synchrotron

(b) H. Mais, Polarization Kinetics in Storage Rings

(c) F. Schmidt, Sixtrack - a Tracking Program to Study Non-Linear Problems of Single Particle Motion in Accelerators

(d) F. Zimmermann, Dynamic Aperture of Storage Rings

5. Other High Order Map Techniques

(a) G. Pusch, Differential Algebraic Computation of High-Order Generating Functions via the Hamilton-Jacobi Equation

(b) J. van Zeijts, TLie, Transport of charged particles using Lie Algebraic techniques

(c) I. Gjaja, Lie Algebraic Computation of Error Effects in Nonlinear Hamiltonian Systems

(d) L. Sagalovsky, RFQ Beam Dynamics and Map Computation

(e) W. Davies, S. R. Douglas, G. D. Pusch, G. Lee-Whiting, DACYC, a Differential Algebra-Lie Algebra Orbit Dynamics Code for the Chalk River Superconducting Cyclotron

MEDICAL CYCLOTRON RF CONTROL UPGRADE DESIGN

G. Zheng, J. Vincent, F. Pigeaud, H. Blosser

Introduction

The K100 Medical Cyclotron, now named Harpertron I, was installed in the Gershenson Radiation Oncology Center in Harper-Grace Hospitals in July 1990. Since then it has been running successfully, giving full energy beam for the purpose of cyclotron adjustment and beam testing, as well as for the neutron survey for future treatment. During this period of time, as one of the many efforts spent in improving the cycloton overall operation performance, several important modifications and upgrade designs have been made on the rf amplifier and its control system. Two major changes and associated upgrade design will be discussed: The use of a linear rf source to drive the modified Transmitter Exciter and the operation of the rf in pulse mode.

RF Exciter Modification

In the early stages of operating the K100 cylotron it was generally difficult to turn on the rf. Later the turn on process became easier with enhanced beam chamber vacuum pumping and was further improved after changing the rf turn-on pulse from a 0.6s/6s slow pulse mode to a 3.3ms, 60Hz pulse mode. At the same time, the wave forms for the drive pulse and the rf were carefully analysed. It was found that the output response of the Continental 802A Exciter, which is used as the rf pre-amplifier, was slow (rise time t_r = 400μs). It was the slow response that reduced the Dee voltage build up rate ($+dV_{dee}/dt$) and made it more difficult to break through multipactoring.

The slow response can be explained with the simplified Transmitter Exciter block diagram. See the drawing on the right hand side of Fig. 1. In the drawing, transistors Q1, Q2, Q3 create a three stage rf amplifier with total gain of 34dBm, while U1 and Q4 constitute a voltage regulator which sets the Q2, Q3 collector voltages that in turn control the Exciter output power. The rf control signal, 3.3ms, 60Hz drive pulse from the Dee Voltage Controller was routed to the input of the voltage

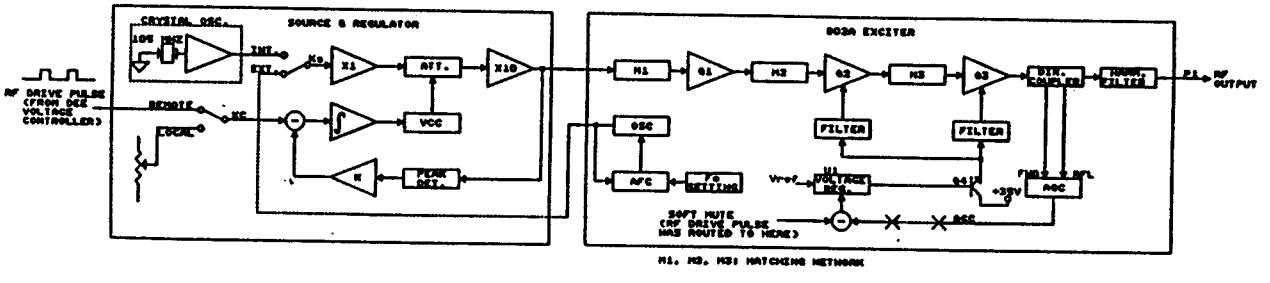

Fig. 1. 802A Exciter & Its New Control Scheme

regulator U1. When the pulse is off, the series pass transistor Q4 will be cut off. That will turn off the collector voltage for Q2, Q3. This results in no rf power output, even if the rf signal is still applied to the Q2 input. When the pulse is on, Q4 will conduct, resulting in rf power output because the Q2, Q3 collector voltages will be rising. As one can see, due to the large time constant introduced by the collector power supply filter circuit, when the drive pulse rises, the Q2, Q3 collector voltage increase will be slow. This will result in an integration of the rising edge of the rf power output and limits $+dV_{dee}/dt$. In addition to the delay problem, controlling the rf power via regulator U1, Q4 also presented a non-linear characteristic, especially in the low power range.

The problems described above can be solved by modifying the Exciter internal connection and changing the control scheme. As shown in Fig. 1, instead of controlling the collector voltage, the new method fixes the collector voltage at the desired value, and controls the Exciter output power by varying the amplitude of the rf input signal. This will substantially improve the system response because the filtering delay is completely eliminated, and will also allow more linear control. To implement this change, it was necessary to build a linear controlled rf signal source, as will be discussed later.

With the new set-up, the rf power will be controlled by a signal source, using a newly designed module called the RF Source & Regulator. The input to Q1 is disconnected from the Exciter internal signal generator. To eliminate interference with the power control, the Exciter AGC loop is disabled. The rf drive pulse from the Dee Voltage Controller that connected to the U1 Soft Mute input is now routed to the rf source control module. The Soft Mute terminal can be either left open or used as an external mute control if needed. The U1 reference voltage V_{ref} still sets the Q2, Q3 collector voltage, and will be used to set the maximum output power for the Exciter.

RF Source & Regulator

The RF Source & Regulator module was built to generate a linear controlled rf signal as the drive source for the Exciter. The module consists of three functional blocks: The rf source, the electronic attenuator and the amplitude feedback control. (See the block drawing in the left hand side of Fig. 1.)

The self contained signal source is a 105MHz crystal oscillator (VECTRON CO233T-3R). A front panel switch allows selection of the internal source, or an external signal generator, such as the 802A Exciter internal signal generator. (Since the Exciter signal generator has an adjustable frequency range, it will be useful for doing Dee system low power tuning.)

The power level of the source signal is at about +10dBm. It is buffered and then attenuated by two mixers which will work as current controlled attenuators. The two mixers are connected in series, and each one is able to give an attenuation of 0 to -45dBm, depending on the control current setting. The final output amplitude from the module is required to be from -30dBm to +10dBm. This signal then will be routed to the input of the pre-amplifier (Q1) as the drive source for the Exciter.

The attenuation control circuit includes Control Reference Setting, Feedback Regulation and Voltage Controlled Current Source (VCC). The Control Reference Setting will set the attenuation level. It can be given from a front panel setting (Local), or by the drive pulse from the Dee Voltage Controller (Remote). In either case, the setting is first compared with a feedback signal, which is the DC output of a RF Peak Detector used to sense the rf output. The error signal will then be integrated and sent out to control the VCC source. The current output of the VCC will control the attenuation and the rf output amplitude.

The use of two cascaded attenuators is intended to provide better source isolation and wider amplitude control range. Feedback control will make the system operation more stable and will also improve the control linearity.

Running RF In Pulse Mode

The K100 Cyclotron was designed to produce a 10μA, 50MeV deutron beam to meet the medical treatment requirements. However, when the cyclotron is well aligned the actual beam can reach 50μA and above, with the rf running at its continuous maximum power of 25kW. In order to reduce the neutron flux, the operating mode was changed from continuous to pulse modulated mode. Experiments have shown that with a 60Hz, 20% duty factor rf waveform, the time averaged beam on the main target can easily reach up to 10μA. This pulsed beam produces the same time averaged neutron yield as the continuous beam, and reduces the rf power to about 20% of what was required for continuous mode. This will improve operating conditions for the Dee system by lowering the amount of rf heating and will allow the rf transmitter to operate at lower power.

Switching to pulse modulated rf does not require changes in the Dee system or transmitter. The major modifications involved are with the rf control system, including the Dee voltage amplitude control and the phase trimmer control, as will be described below.

Dee Voltage Control

When running in continuous mode, the initial pulsed signal that drives the rf pre-amplifier (Exciter) will be disabled as soon as Dee voltage breaks through the Dee Low level. After this the

pulse circuit will pass control to the Dee voltage amplitude control loop. If the rf stays on, pulsing will stop and the amplitude control loop will start to regulate the Dee voltage. The pulse timing will resume each time the rf is removed for some reason (eg. dv/dt).

When running in pulse mode, the pulse generator should be independent of the rf, and maintaining its own timing (3.3ms on and 13.4ms off). During the pulse on cycle, if the Dee voltage breaks through the Dee Low level and stays on, the amplitude loop will take over the control and start to regulate Dee voltage, just as it does in the continuous mode. Because the amplitude loop response is less than 10μs, that is rather a short time compared with the 3.3μs pulse on time.

For either case, the Dee voltage will be controlled by the pulse height setting when the rf is being pulsed on, and by the Dee voltage amplitude setting when the rf remains on.

Phase Trimmer Control

The purpose of the phase trimmer control is to automatically tune the rf resonator to the correct resonant freqency. Figure 2 is a simplified block diagram of the trimmer control system designed for the K100 cyclotron. The phase control is normally disabled when the rf is off or unstable. It will function only when the rf is on and the phase error between Dee voltage and the rf forward power is significant, which is set by a window comparator. A TTL high to low transition signal from the Dee Voltage Controller will be used to trigger a gating control circuit. The output HIGH of the circuit, called RF OK, will gate the window comparator output to solid state relay Kp or Km, depending on the polarity of the phase error. When the phase error is positive, Kp will be on and

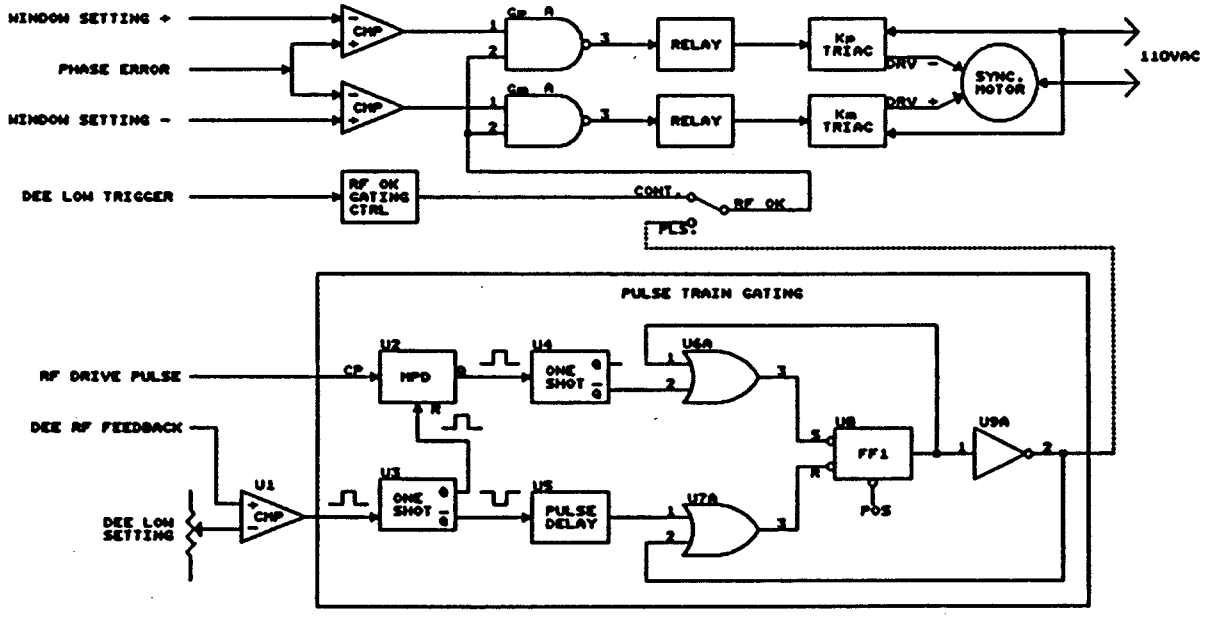

Fig. 2. Phase Trimmer Control

the trimmer will be driven in the negative direction to reduce the phase error until it is zero. For negative phase error, Km will be on, causing the trimmer to move towards the positive direction until the rf phase is matched.

The phase control loop is slow because the mechanical servo and the drive relays both have a very limited bandwidth. However, since phase changes are primarily introduced by the Dee system thermal effects, the rf phase drift is usually slow. As a result, the trimmer control system has been working well in tracking the phase change even though it has limited bandwith.

When switched to 60Hz, 3.3ms pulsed rf, the trimmer did not work well. This was due not only to the slow servo loop response, but also because, with 60Hz pulse gating, the solid state relays (Triac Kp and Km) used as the line switches were not be able to generate proper AC output to drive the synchro motor for the trimmer.

A simple way to solve this problem is to keep the trimmer working in continuous mode and change the RF OK gating signal. That is, instead of enabling and disabling the trimmer control each time the rf pulses on (3.3ms) or off (13.4ms), it will be gated on for as long as the rf pulse train exsists, and turned off as soon as the pulse train is gone. The so called Missing Pulse Train Detecting (MPD) technique will be used for this application, see the Pulse Train Gating circuit block diagram at the bottom of Fig. 2.

As shown in the diagram, the RF OK signal, which now is from the output of inverter U9 and controlled by the Flip Flop FF1, will be set to LOW by the Power On Set (POS) circuit when the dc power is first turned on. It will stay LOW as long as there is no reset pulse from the OR gate U7 to reset the FF1. Both NAND gates Gp and Gm will be closed resulting in no drive command sent to either Kp or Km.

When the 60Hz pulse signal starts to drive the rf, and when the rf is on with the Dee voltage above Dee Low, the Dee voltage feedback signal will turn the output of the Dee Low comparator U1 from LOW to HIGH. When the pulse is off, the U1 output will change from HIGH to LOW. There will therefore be a pulse train from U1 output if the rf is pulsing on. With the front edge differentiated by U3, this pulse train will be routed to the input of the Pulse Delay Counter U5. After an N pulse delay, the (N+1)th pulse will be output by U5 and reset FF1. This will make the RF OK signal go HIGH, opening NAND gate Gp and Gm to enabe the phase trimmer control. The trimmer will continue to function as long as the rf pulse train remains.

At the same time, the rf feedback pulse train will be sent to MPD U2 to compare with the rf drive pulse. Normally the U2 output will remain LOW if two pulse train are well matched. If the Dee voltage goes off for any reason, a pulse may be missing from the U1 output or the whole pulse train

will go off. The MPD will detect those events and trigger U4 if they occur, which then sets the U8 output HIGH. The RF OK signal will then go LOW, disabling the trimmer control.

Phase Detector

The Phase Detector that detects the phase error between the Dee voltage and rf forward power also needed to be modified to work in pulse mode. When the rf is off, the phase signal may be uncertain and is meaningless. This was not a problem when running in continuous mode because the trimmer is normally off and will work only when the rf is on and stable. But in pulse mode, the rf will be turned off during the off cycle even when it is regularly pulsing on. The trimmer may also still remain functioning during that off time. It is therefore important to filter out the uncertain signal when the rf is off. For this reason, a rf pulse synchronised gating control circuit was designed, which will turn off the detector output during the rf off cycle.

Conclusion

The rf control system was first designed to run in continuous mode and has been working well in the past. A modification was made to the system to enable it to also work in pulse mode so the cyclotron can run pulse modulated beam. To switch easily between the two modes, a Mode Control module was designed. Shown in Fig. 3 is the simplified new rf control system configuration for the K100 medical cyclotron. All upgrade designs have been completed recently and are working with the rf now running in a more stable manner because these successful changes. Another advantage of this new configuration is that Dee system low power tuning can be done with the same set up, and requires no external signal source and amplifier (by switching Kc to Local, Ks to Ext. and connecting P1 to T). The next required step is to perform more testing and careful tuning which may help to further improve the rf amplitude control performance and increase the trimmer dynamic range.

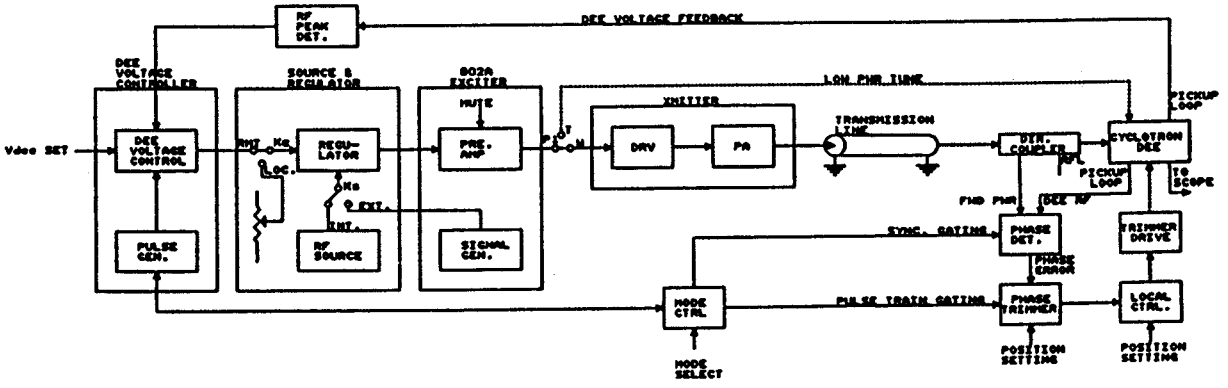

Fig. 3. Modified RF Control System

SEARCH FOR MATERIAL DAMAGE OF ION IMPLANTED SILICON NITRIDE AND STAINLESS STEEL

T.L. Rachel[a], Y. Chung[a], T. Stuecken[a], H.J. Schock[a], R. Shalek[b], D. Grummon[b], T. Hsieh, J. Kuchar, Wm.C. McHarris, R.M. Ronningen, and M.L. Mallory[c]

During the last several years we have been developing an implantation technique potentially useful for the study of mechanical wear. The method involves the implantation of radioactive ions, such as ^{7}Be or ^{22}Na, into the surface of a mechanical part. The wear of the part can be monitored *in situ* by a measurement of the radioactivity, if the dose-depth distribution of ions is known.

The implantation technique will complement a wear measurement method called Surface Layer Activation, in which the ion beam transmutes nuclei in the surface of the part, producing radioactivity. However, with both techniques there is a problem deserving study. This problem is the degree to which the implanted, or the activating beam damages and alters the wear characteristics of the material. Ion implantation research suggests that, for high doses ($>10^{16}$ ions/cm^2) of ions with low bombarding energies (typically several MeV or lower), a variety of material properties can be changed. These changes include amorphization, defect clusters, destruction of crystallinity or the production of a new phase, and surface hardness alterations. Such ion doses are comparable to those used in surface layer activation, and are at least several orders of magnitude larger than that needed to produce a useful (~1 Ci) activity.

This year we have constructed a new vacuum chamber for wear studies and installed it in the NSCL Transfer Hall. The chamber is shown in Fig. 1. We then performed an experiment to test for material property alteration by implanted ions. The materials selected for implantation were silicon nitride (Si_3N_4)[1], and stainless steel (17-4PH), initially mostly austenite but was further prepared to be 98% martensite. Silicon nitride was chosen because it is considered one of the standards for advanced ceramic materials research. Stainless steel was chosen because its martensite phase is metastable, reverting to the austenite phase under kinetic energy transfer from the ion beam. The samples were manufactured as shown in Fig. 2. The radiused edge was made so that the samples could be used in a piston ring wear testing apparatus at Battell Memorial Institute, Columbus, Ohio. The Department of Mechanical Engineering's Buehler polisher/grinder was used to prepare the samples for nanoindentation studies. Its platens can be chosen from several materials having differing finish grades, and can be used with abrasive liquids that include diamond suspensions.

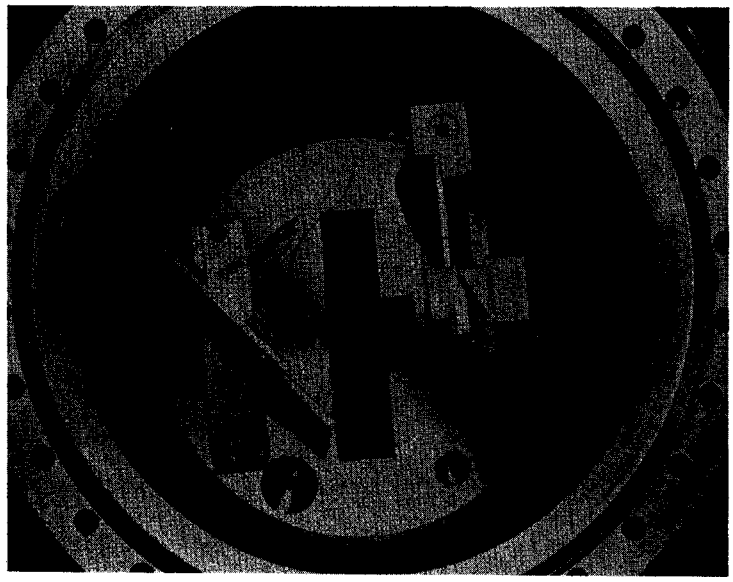

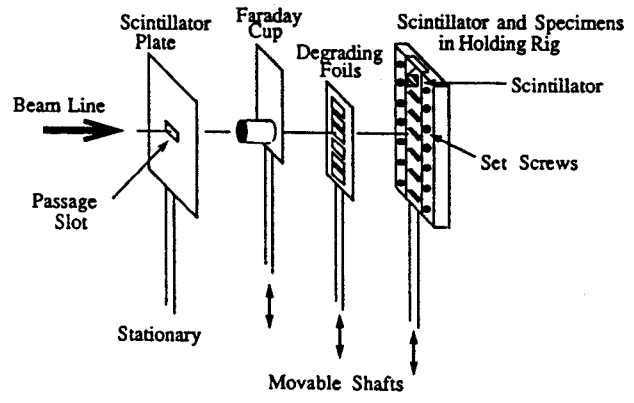

Fig. 1. In the top panel, the vacuum chamber for wear studies is shown with its top cover removed. The chamber was manufactured by MDC Vacuum Corporation. There are four drives; from left to right these are: an 45 degree aperatured viewing plate, a Faraday cup, a variable position ladder for degrader foils, and a variable position ladder for samples. In the bottom panel is a line drawing of these features.

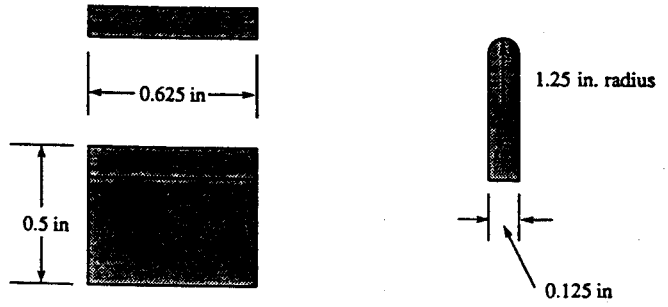

Fig. 2. Dimensions for ceramic and steel samples.

The samples were irradiated by a 2.5 Mev/u ^{20}Ne beam from the K500 cyclotron. The beam ion was chosen to mimic damage that might be caused by implanted ^{22}Na, and probably overestimates the damage which would be caused by ^{7}Be, for the same range. The beam energy was chosen so that, while a useful implantation depth would be achieved (15-20 microns), the sample would not become significantly radioactive. Irradiation times were adjusted to produce doses of 10^{12} to 10^{14} ions/cm^2. Such doses will produce amounts of radioactivity useful for wear studies. For example, a 1 Ci source of ^{7}Be (^{22}Na) contains $2.5\text{x}10^{11}$ ($4.4\text{x}10^{12}$) nuclei.

The samples for the hardness tests were stacked in pairs so that the beam illuminated both members. The damage could then be accessed by measuring hardness and elasticity across the common interface surface. Samples for the Battelle wear testing apparatus were irradiated at six depths each, to a maximumm of 4.5 microns. Six gold foils of known thicknesses (made using the Metallurgy, Mechanics, and

Materials Science Department's sputtering chamber) were used as energy degraders to obtain the desired ranges.

Hardness and elasticity measurements were made at the High Temperature Materials Laboratory, at Oak Ridge National Laboratory, using a mechanical properties microprobe (nanoindenter) of the Berkovitch type. The position resolution was 0.2 nm over a range of 100 m, and load ranges were 0-120 mN and 0-20 mN, with a 0.2 μN resolution for the latter range. Typically, several runs were made on each sample, with 6 to 43 indents per run and depths of 50, 100, 150, and 200 nm per indent. Control data were taken from samples that were either not irradiated, or from nonirradiated portions of sample surfaces. The analysis is at a preliminary stage, but Fig. 3 shows data on stainless steel samples, for 10^{12} and 10^{14} ions/cm^2. Data for silicon nitride look similar but are somewhat poorer statistically, because of the difficulty in surface preparation. We find that no damage, at least manifested by changes in hardness and elastic modulus, is detected at 10^{12} ions/cm^2, but softness is detected at 10^{14} ions/cm^2. While not shown, there appears to be no strong evidence for damage at 10^{13} ions/cm^2. For the ongoing Battelle wear tests, at 10^{14} ions/cm^2 no significant differences were found in the wear rates between the control and the implanted samples. A summary of the preliminary data is shown in Fig. 4. Thus, if the threshold for damage is close to 10^{14} ions/cm^2, one may use radioactivities to 10 Ci of ^{7}Be or ^{22}Na, if desirable and economically feasible.

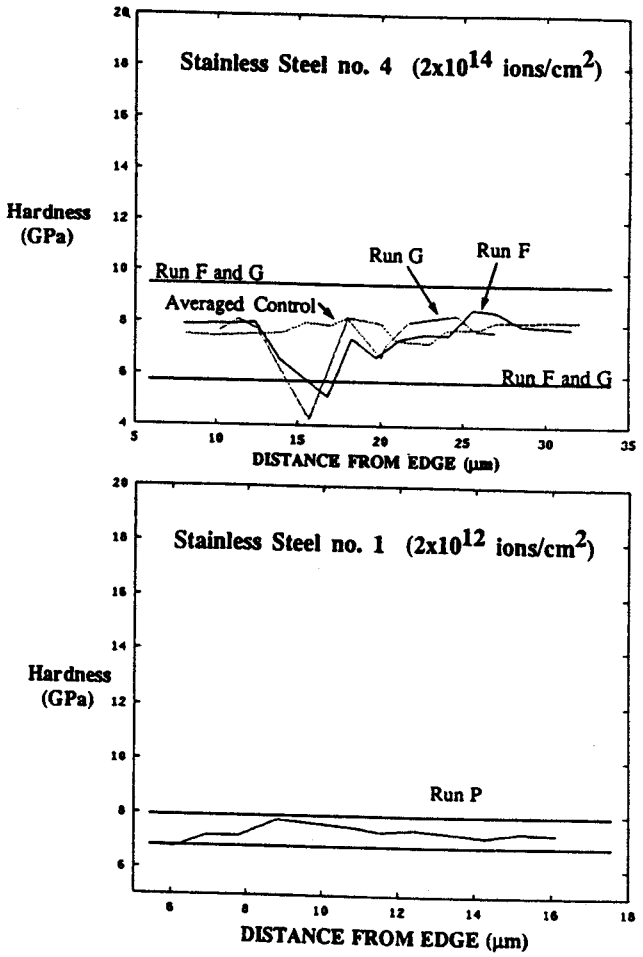

Fig. 3. Nanoindentation results for stainless steel samples (98% martinsite). The upper panel shows hardness data for an implantation dose of 10^{14} ions/cm^2, and for a nonirradiated control. The lower panel shows hardness data for an implantation dose of 10^{12} ions/cm^2.

Finally, we used the code TRIM (TRansport of Ions in Matter)[2] to predict damage for protons (used for surface layer activation), and ^{7}Be

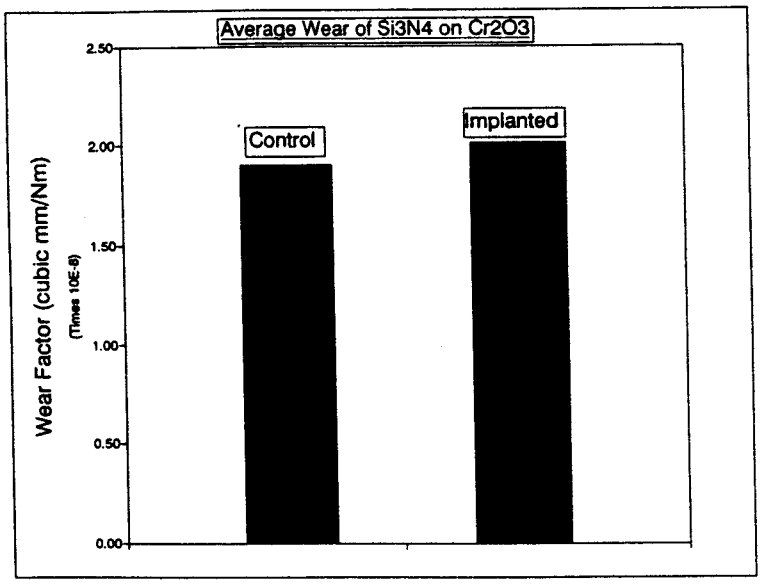

Fig. 4. Preliminary results from the Battelle Memorial Institute piston ring wear testing apparatus. The silicon nitride sample contacted a chromium oxide surface. The samples were implanted as described in the text.

and ^{22}Na ions. We chose the number of vacancies per ion as a figure of merit for damage. Protons of 7 Mev were used, with the energies of the other ions selected to match the proton range. We find, on the average, protons produce at least one order of magnitude more vacancies than the other ions for a given activity. Thus, we expect, and our preliminary data shows, that the technique of implanting radioisotopes into materials at the 1 to 10 Ci level is fairly innocuous to the material's wear characteristics.

a. Mechanical Engineering Department, MSU.
b. Metallurgy, Mechanics, and Materials Science Department, MSU.
c. Present address: M.D. Anderson Hospital, University of Texas, 1515 Holcomb Blvd., Houston, TX 77030.

References

1. NC-132, supplied by the Norton Corporation
2. TRIM-90, TRIM-91, J.F. Ziegler and J.P. Biersack, IBM Research, Yorktown, NY, June 11, 1990, and January 3, 1991.

RADIATION DAMAGE MECHANISMS IN NdFeB

A.F. Zeller

The results of several studies[1-5] indicate that NdFeB is much more sensitive to radiation damage that either $SmCo_5$ or Sm_2Co_{17}. It has long been felt that the radiation damage is similar to thermal demagnetization effects, ie., related to the coercivity, H_c. Thus it is not too surprising that the radiation sensitivity is different since the coercive mechanisms are different.

The dominant coercive mechanism for NdFeB is nucleation hardening. If one assumes that the radiation induced loss of magnetization is caused by the nucleation of reversed domains[5], then the rate of flux loss should be given by the simple first order rate equation:

$$dM/d(\text{time or dose}) = C\, e^{-E'/kT} \qquad (1)$$

where C is an empirical constant, E' is the activation energy, k is Boltzmann's constant and T is the temperature. However, when the loss of magnetization is plotted against the dose, the resulting curve shown in Fig. 1, has more than one component, ie., the initial loss rate is greater than the loss rate at larger doses. This would indicate that E' is not a constant or that the mechanism is changing. If we imagine a small dipole, with negligible volume, in the middle of the sample, the demagnetization field as a function of radius is given by:

$$H_{demag} = \frac{\mu_0 \mu}{4\pi\, r^3} \qquad (2)$$

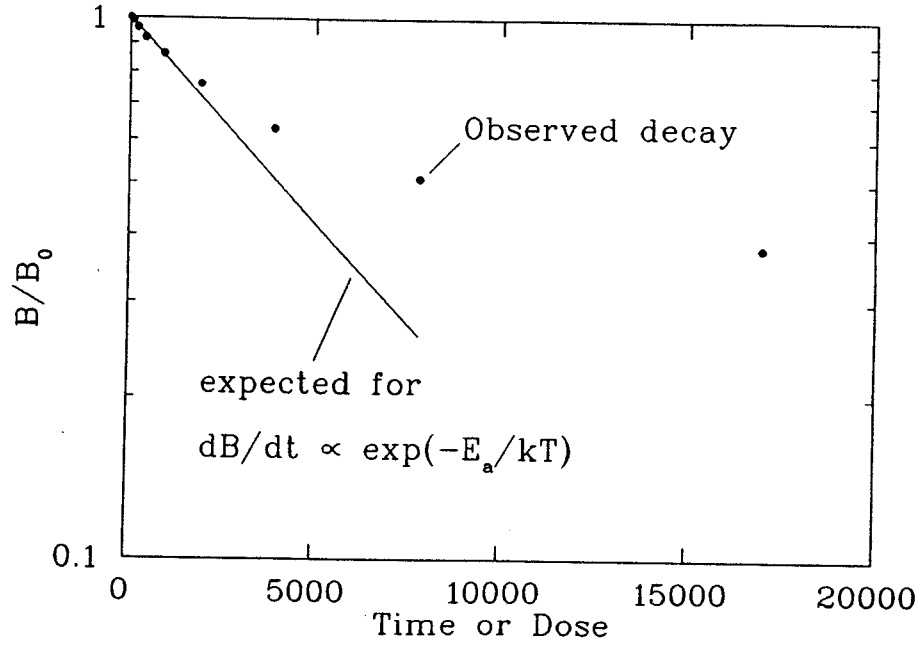

Fig. 1: Rate of loss of magnetization for NdFeB. The data is for neutron irradiation from Ref. 5.

where μ is the dipole moment. Thus the material near the edges of a cylindrical sample is not as strongly demagnetized as the center. This also shows up in the well known dependence of irreversible loss upon the permeance coefficient ($P_c = B/H$).

If the loss mechanism for radiation damage is similar to that seen in heat treatment, then the material should show similar loss patterns. A sample of NdFeB was irradiated with gamma rays from ^{60}Co, as described in ref. 2, for varying lengths of time. The resulting maps and those observed in thermal demagnetization studies show similar loss patterns. At first glance we would expect that the charged particle and gamma ray results should be identical for identical doses since the Rad is a unit of energy deposition per unit mass. This is not the case since less than 3 MRad of charged particles produced more than 50 times the flux loss induced by 50 MRad of gamma irradiation[2]. It is also seen that neutrons[4,5] and electrons[3] are more damaging than gamma irradiation. A similar "Relative Biological Effectiveness" is seen in living organisms.

One aspect of radiation damage that has been observed[1,2,4,5] is that the higher the coercivity of the material, the lower the loss of flux. Similar behavior is seen in temperature induced loss of flux in NdFeB and both types of SmCo, even though the coercive mechanism is very different. NdFeB material having Dy or other heavy lanthanides added to increase the coercivity show less sensitivity to gamma and neutron damage that the standard materials. When the sample is irradiated the center part quickly loses it's coercivity, while the outer, larger area is less affected. PANDIRA calculations were made for a cylindrical, thin sample where successive portions of the middle were partially or completely demagnetized. The four cases shown in Fig. 2 are the flux lines in one quarter of a thin sample with cylindrical symmetry. In each successive part the coercivity of the innermost region has been reduced. We see that when the coercivity has been reduced to a very small value that the sample now has a hole in the middle where the polarity has actually reversed. This is on a macroscopic scale what must happen in a multi-domained grain when reversed domains have been induced. A plot of the magnetic field component which is parallel to the magnetization axis (B_z) as a function of radius is shown in Fig. 3 for the cases shown in Fig. 2. The region which is demagnetized has a radius which is only about 10% of the full radius, ie., 1% of the total volume. In the real heat treatment or irradiation, the whole sample is subjected to demagnetization, not just the center region. Because of the limited number of regions which can be used in PANDIRA four were used to simulate a more uniform demagnetization process. Several cases are shown in Fig. 4. Extrapolation to the case of many regions we see the following features: The center is the quickest to be demagnetized and as the center is demagnetized the outer radii are subjected to less demagnetization forces. Taken to the extreme of reducing the coercivity in the inner three regions

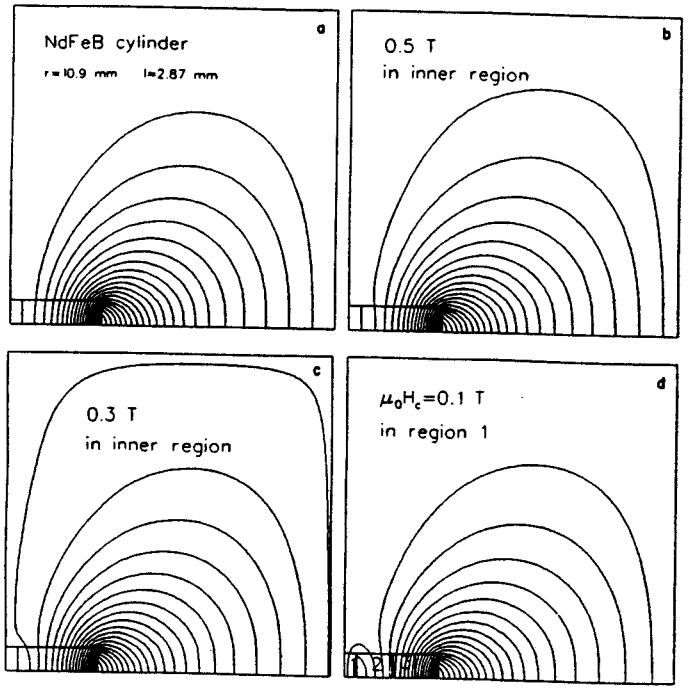

Fig. 2. PANDIRA calculations for a sample of NdFeB in cylindrical coordinates. a) is the original material, b) is for the coercivity reduced to 0.5 T in region 1, c) shows a further reduction to 0.3 T, and d) is reduced to 0.1 T. Note that the product of radius times vector potential has been plotted.

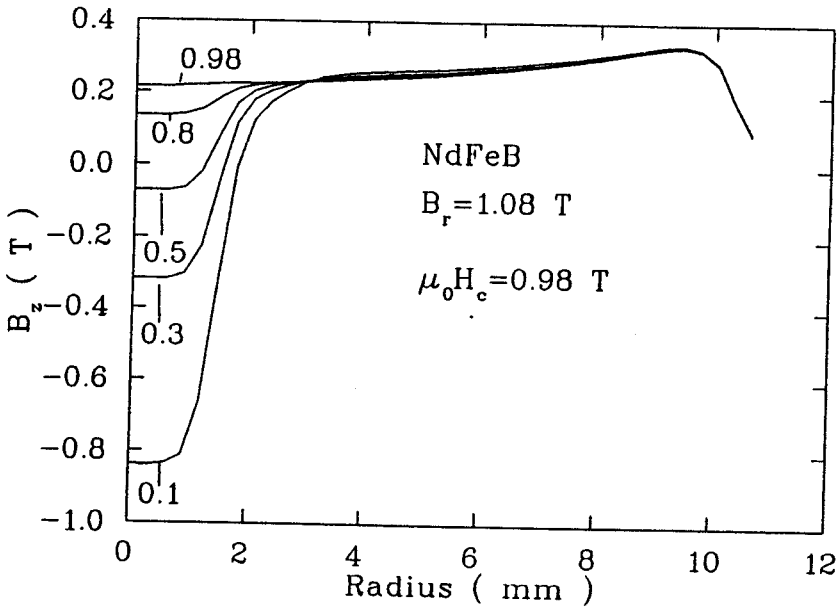

Fig. 3. Field components as a function or radius for the cases illustrated in Fig. 2.

the outer segment actually increases its field strength, as seen in Fig. 4. This results in a demagnetization curve which quickly demagnetizes the center regions and then the process slows down because the activation energy required to demagnetize the outer, less stressed regions is greater. This leads to curves like those seen in all of experimental data. Additionally, of course, the rate is further reduced because of the greater volume of PM material in the outer segments compared to the inner regions.

There is a second way that the PM material can lose its field strength, ie by the loss of B_r. To test the sensitivity to this process further PANDIRA calculations were made. In this case the inner region of Fig. 2 was given a reduced remanent field of 0.5 T, while keeping the coercivity the same. This is shown in Fig. 5. The results should

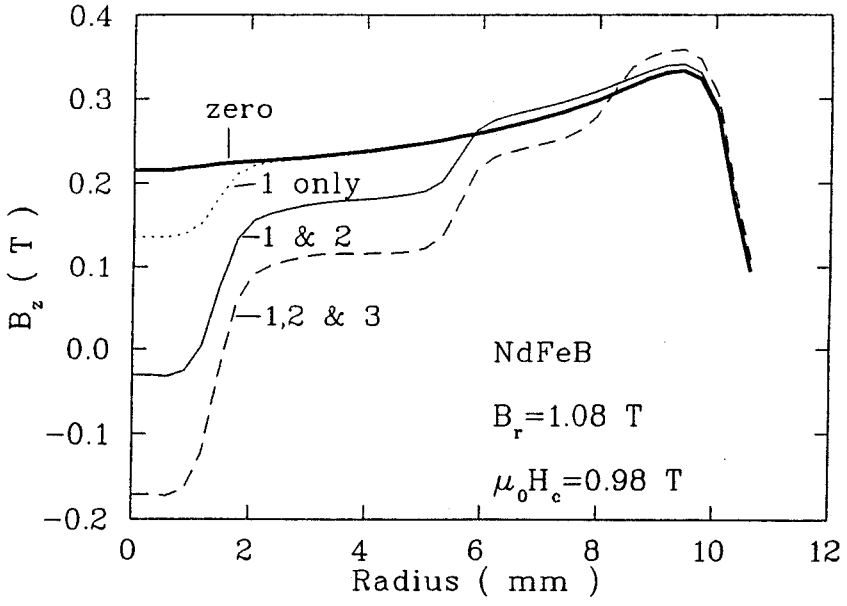

Fig. 4. Successive reduction of the coercivity in the three inner regions shown in Fig. 2. The curve marked "zero" is for the material with properties listed in the figure.

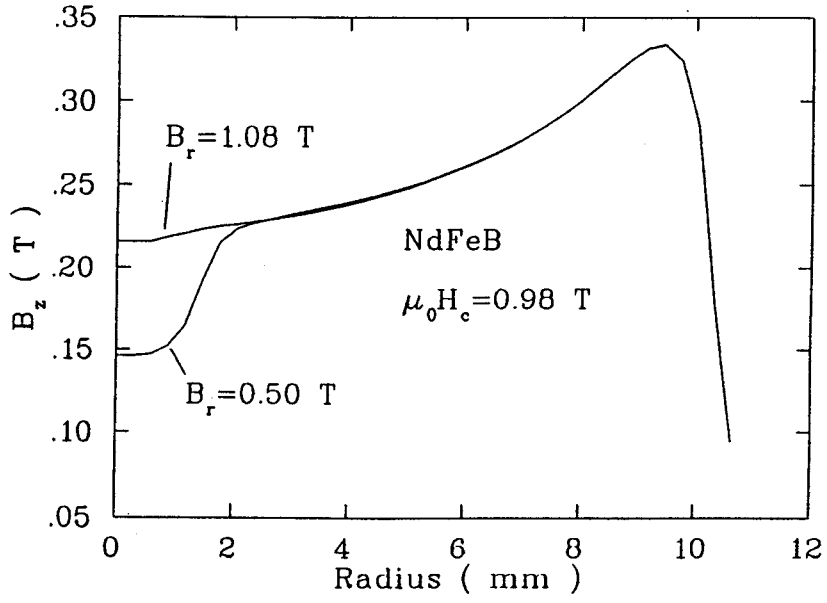

Fig. 5. The remanent field in region (from Fig. 2) has been reduced to 0.5 T. The resulting B_z components are shown here.

be compared with Fig. 4, where the coercivity for the same region has been reduced. We see that the reduction in coercivity is much more effective than a reduction in remanent field. When PM materials are heated, both the coercivity and the remanent field are reduced, so the demagnetization will proceed with contributions from both sources. In an irradiation experiment this shows up as a decrease in the rate of flux loss. Because the pre-exponential factor in eq. 1 is very difficult to calculate the activation energy required to precipitate a reversed domain can be determined by examining the temperature factor. Therefore, by irradiating a sample at two different temperatures, the initial loss rate gives E' from:

$$E' = \frac{kT_1T_2}{T_2 - T_1} \ln (\text{rate2/rate1}) \qquad (3)$$

For the neutron irradiations in Ref 5, E' is determined to be 0.14 eV. The specific value of E', of course, depends on P_c. Recent results for 20 MeV proton irradiation of NdFeB at room temperature and at 20 K for very thin samples[6] yielded an activation energy of 0.01 eV. The strong dependence on demagnetization factors enters into the activation energy as B^2, so this result is not too surprising.

Although both NdFeB and $SmCo_5$ are nucleation hardened materials, NdFeB is more readily demagnetized from radiation effects. A 10 MeV proton will deposit about 300 eV in a typical knock-on reaction[7] from the recoiling atom. The diameter of a sphere of NdFeB material in this hot "spike" which is heated to a 1000 K is about 3 nm, which is close to the measured[8] domain wall thickness of 5.2 nm. Although there is a ideal wall thickness where the system is in equilibrium, it is an unstable equilibrium, which tends to move the Bloch walls quickly[9] when disturbed. Thus one expects that irradiation of NdFeB is more damaging than irradiation of $SmCo_5$. Additionally, the presence of light elements such as B and O renders it more susceptible for large energy transfers because the recoil energies of these light elements are higher. Sankar et al[10] have postulated that a valence change on the B atoms could be responsible for the susceptibility of NdFeB to radiation damage. This can only be the case if the radiation damage mechanism differs from the loss of flux that occurs when the material is heated. If the basic mechanisms are the same then change in the B valence state could only be part of the explanation.

The general shape of all radiation induced flux loss curves is shown to be the result of a gradual demagnetization of the stressed center regions of a NdFeB sample. This proceeds quickly, but also reduces the demagnetization forces on the outer regions, resulting in a decreased rate of demagnetization.

References

1. E.W. Blackmore, IEEE Trans on Nucl Sci NS-32 (1985),p 3669.
2. A.F. Zeller and J.A. Nolen, 9th Int Workshop on Rare-Earth Magnets Bad Soden, FRG, 1987,p 159.
3. H.B. Luna, et al, Nucl Inst Meth A285 (1989),p 349.
4. J.R. Cost, et al, J. Appl Phys 64 (1988),p 5305.
5. J.R. Cost, et al, Mater Res Soc Symp Proc 96 (1987),p 321.
6. O-P. Kahkonen, et al, submitted to Europhysics Letters (1990).
7. F. Seitz and J.S. Koehler, Solid State Phys 2 (1956),p 305.
8. M. Sagawa, et al, J. Appl. Phys. 55 (1984),p 2083.
9. J.S. Broz, et al, Phys. Rev. Lett. 65 (1990),p 787.
10. S.G. Sankar, et al, 5th Int. Symp. on Mag. Anisotropy and Coercivitivy in Rare-Earth-Transition Metal Alloys, Bad Soden, FRG 1987,p 109.